Dipl.-Ing. Peter Pichler, BSc.

Thermophysical property measurement: On earth and in microgravity on-board of parabolic flights and the International Space Station

DOCTORAL THESIS

to achieve the university degree of

Doktor der technischen Wissenschaften

submitted to

Graz University of Technology

Supervisor

Ao.Univ.-Prof. Dipl.-Ing. Dr.techn. Gernot Pottlacher

Institute of Experimental Physics

Graz, March 2021

This document is set in Palatino, compiled with pdfLaTeX2e and `Biber`.

The LaTeX template from Karl Voit is based on KOMA script and can be found online: https://github.com/novoid/LaTeX-KOMA-template

Affidavit

I declare that I have authored this thesis independently, that I have not used other than the declared sources/resources, and that I have explicitly indicated all material which has been quoted either literally or by content from the sources used. The text document uploaded to TUGRAZonline is identical to the present doctoral thesis.

04.03.2021	Peter Pichler
Date	Signature

Acknowledgment

Writing a thesis is a stressful yet rewarding process full of fears, melt-downs, anxiety but also joy, anticipation and happiness. While it is true that a lot of work is done alone and the success ultimately depends on your own capabilities, the creation of such a project is impossible without the support of many people. During the process of understanding the experimental tools and evaluation techniques, performing measurements, writing up results, publishing said results and finally writing up what I have done the past four years, I worked with, depended on and exchanged thoughts with a multitude of great people. It is now time to thank those wonderful people. I sincerely apologise to anyone, I might have left out.

First and foremost I would like to express my deepest gratitude to my supervisor Ao.Univ.-Prof. Dipl.-Ing. Dr.techn. Gernot Pottlacher. His ability to find solutions for any problems and difficulties we faced was truly inspiring. Not only did he provide help and knowledge to any experimental, physical or fish-related question, but he also understood how to motivate his working group, keep morale high and set an example for great leadership. Thank you, I will always enjoy looking back at my time at the Thermo- and Metalphysics Group.

During my time at the working group I had the pleasure to work with many brilliant minds and kind people. I am grateful to all of them, but as I do not want this section to surpass the rest of this thesis in length I will mention the two guys who walked with me on this path the longest. Dipl.-Ing. Thomas Leitner and Dipl.-Ing. Dr.techn. Matthias Leitner. Thomas, thank you for being the helpful, positive and cheerful person you are. You investing your time in trying to help solving other peoples problems, without ever getting sour about it, is humbling. Thank you for your help and thank you for many entertaining moments and coffee breaks.

Matthias, you showed me all the secrets of ohmic pulse-heating and helped me with many physical problems. I thank you for that. But what I am mostly grateful for is the long friendship we share, all the memories, the night-walks when we were 15 year old boys and the certainty that I can always count on you. Thank you.

I want to thank all the people I met at conferences and had discussions with. All the physicists, I collaborated with during my work. And of course all the members of the Hi-TRACE project. Our meetings have always been fruitful and interesting and I am very happy to have been a part of such a great project with so many brilliant people. Thank you to all the people at NIST who I collaborated with. I appreciate the opportunity of working with you. Special thanks to Dipl.-Ing. Dr.techn. Konstantinos Boboridis, Dipl.-Ing. Dr.techn. Boris Wilthan and Dipl.-Ing. Dr.techn. Claus Cagran who showed me the ways of ellipsometry and always answered my questions with patience.

Thank you to all the people involved with the microgravity experiments, especially voestalpine BÖHLER Edelstahl GmbH & Co KG, DLR and JAXA. Being part of a team that is involved with experiments on the International Space Station was a once in a lifetime possibility.

Finally I want to thank my parents and my sisters. My parents, Eva and Horst, who supported me in any way possible. Thank you for always being there, without you I would not have become the person I am today. Thank you Monika and Susanne, I can always count on you and I am very grateful that I have such awesome sisters.

Last but not least, thank you Sarah. You helped and supported me in so many ways throughout these last years. All the trips and vacations we took and the time we spent together helped me to recharge and kept me motivated and (reasonably) sane.

Abstract

In this work, thermophysical properties of selected high melting metals, alloys and standard reference materials are measured with a multitude of experimental methods. These methods include ohmic pulse-heating, microsecond division of amplitude polarimetry, electromagnetic levitation, dynamic scanning calorimetry and electrostatic as well as electromagnetic levitation in microgravity conditions on-board of parabolic flights and the International Space Station. The thermophysical properties obtained in this work are specific enthalpy, electrical resistivity, density, thermal expansion, thermal diffusivity, thermal conductivity, specific heat capacity, surface tension and viscosity, all as a function of temperature. Uncertainty estimations according to the *guide to the expression of uncertainty in measurement* (GUM) were performed for the obtained properties.

Surface tension and viscosity are measured primarily on board of parabolic flights with the TEMPUS facility. During the seven hour long flight several parabolas are carried out, providing approximately twenty seconds of microgravity each, to record surface tension and viscosity data. Surface tension data were compared to ground-based experiments under the influence of gravity. As viscosity measurement is impossible with electromagnetic levitation devices on-ground, these data were only measured on-board of parabolic flights.

Additionally, measurements on the nickel-based super-alloy L625 were performed in microgravity conditions on-board of the International Space Station.

Zusammenfassung

In dieser Arbeit werden die Ergebnisse von Messungen thermophysikalischer Eigenschaften von hochschmelzenden Metallen, Legierungen und Standardmaterialien präsentiert. Die Methoden zur Bestimmung der thermophysikalischen Eigenschaften umfassen Ohm'sche Pulsheizung, Mikrosekunden Division of Amplitude Polarimetry, elektromagnetische Levitation, dynamische Differenzkalorimetrie, sowie elektrostatische und elektromagnetische Levitation unter Einfluss von Mikrogravitationsbedingungen an Bord von Parabelflügen sowie auf der Internationalen Raumstation. Die in dieser Arbeit gemessenen thermophysikalischen Eigenschaften sind die spezifische Enthalpie, der elektrische Widerstand, die Dichte, die thermische Ausdehnung, die Wärme- und Temperaturleitfähigkeit, die spezifische Wärmekapazität, die Oberflächenspannung und die Zähigkeit, alle als Funktion der Temperatur. Unsicherheitsbetrachtungen gemäß dem *Leitfaden zur Angabe der Unsicherheit beim Messen* (GUM) wurden für die erhaltenen Messgrößen durchgeführt.

Oberflächenspannung und Zähigkeit wurden in erster Linie an Bord von Parabelflügen mit der TEMPUS Anlage bestimmt. Während einer Flugzeit von sieben Stunden werden eine Vielzahl von Parabeln geflogen. Diese Parabeln bieten in etwa zwanzig Sekunden Schwerelosigkeit um Oberflächenspannungs sowie Zähigkeitsdaten aufzunehmen.
Die so erhaltenen Oberflächenspannungsdaten werden mit Daten verglichen, die unter Einfluss der Gravitation auf der Erde mittels elektromagnetischer Levitation bestimmt wurden. Da Zähigkeitsmessungen mit elektromagnetischen Levitationsapparaten auf der Erde nicht durchgeführt werden können, wurden diese Daten nur an Bord von Parabelflügen bestimmt.

Weiters wurden Messungen der Nickelbasis-Superlegierung L625 in Schwerelosigkeitsbedingungen an Bord der Internationalen Raumstation durchgeführt.

Contents

List of Figures

List of Tables

1. Introduction

Knowledge of thermophysical properties, especially in the liquid phase, is of fundamental importance to our daily world. The production of car parts, aircraft turbine blades or even work tools like wrenches, nowadays is dependent on simulations and modelling to ensure highest production yield and durability. While the behaviour of a molten alloy and many properties can be simulated, experimental data are still needed. Any model or simulation, even ab-initio simulations have to be verified in some way. Comparing simulated values to experimentally accessed data increases the credibility of the simulation and paves the way for more complex calculations. Other models may be dependent on input parameters, which can be accessed by an experiment. Apart from modelling, knowledge of thermophysical data helps with the reduction of casting defects or defects occurring during additive manufacturing processes.

Therefore, at the Thermo- and Metalphysics group of the Institute for Experimental Physics at Graz University of Technology, thermophysical properties of metals and alloys have been experimentally characterized for more than 30 years. From fundamental research to up-to-date industrial collaborations, 139 peer reviewed publications, 11 (+2 in the making) PhD and 47 diploma theses have been written, and knowledge has been built and distributed at countless expert conferences and symposia during this long period of time. With the retirement of Prof. Gernot Pottlacher in 2021 and the closure of the group, this work will be the second to last thesis conducted at the Thermo- and Metalphysics group in Graz.

During the work on this thesis, many international collaborations have been built. Together, with the National Institute of Standards and Technology (NIST) in Boulder, CO, USA, experimental work on one of their Standard Reference Materials (SRM) has been performed and the obtained data will

be used by modellers to optimize laser welding and additive manufacturing processes. Details on the measurement and more information can be found in chapter 3.

As part of the European Metrology Programme for Innovation and Research (EMPIR) project 17IND11 "Hi-TRACE" new metrological facilities are being developed at the Laboratoire national de métrologie et d'essais (LNE) in Paris, the Physikalisch Technische Bundesanstalt (PTB) in Berlin and Braunschweig, the Bavarian Center for Applied Energy Research (ZAE) in Würzburg and the Institut Za Nuklearne Nauke Vinca (VINS) in Belgrade. As part of this work, reference measurements on standard materials have been performed to validate the results of the newly developed facilities. More information about the project and measurement can be found in chapter 4.

Together with the European Space Agency (ESA), voestalpine BÖHLER Edelstahl and the Deutsche Zentrum für Luft- und Raumfahrt (DLR) another international collaboration has been formed. The nickel-based super-alloy L625 by voestalpine BÖHLER Edelstahl was characterized by means of pulse-heating and dynamic scanning calorimetry at the Institute of Experimental Physics in Graz and is planned to be analyzed in the TEMPUS facility on the International Space Station (ISS). In order to being allowed on the ISS, the material is tested in micro gravity conditions on board of parabolic flights. Details can be found in chapter 2.5. Additionally, in cooperation with the Japanese Aerospace Exploration Agency (JAXA), the alloy was investigated by means of the electrostatic levitation furnace (ELF) on the Japanese Experiment Module (Kibo) on board the ISS. Results for the super-alloy are presented in Chapter 5.

The assessment of uncertainties in a standardized manner has always been a part of the work of our group. Therefore, uncertainty assessment for this and previous works have been performed according to the "Guide to the Expression of Uncertainty in Measurement" (GUM) [1]. Information on uncertainty assessment can be found in chapter 6.

2. Experimental Methods and Data Evaluation

The experimental methods used to determine thermophysical properties of metals and alloys are listed in this chapter. While the work conducted for this thesis can be divided in three parts, all methods for measuring and evaluating the desired properties are listed and explained in this chapter.

2.1. Ohmic Pulse-Heating

The ohmic pulse heating apparatus (OPA) was set up in the 1990s by Kaschnitz [2]. Since then it has been gradually improved and provides an outstanding method to determine thermophysical properties of conducting materials in the solid, and especially in the liquid phase. Wire-shaped samples are heated up from room temperature, through the liquid phase, finally reaching the boiling point, where the sample explodes. Therefore, the method has also been referred to as "exploding wire technique". A capacitor bank with 500 µF, which can be charged up to maximum voltages of 10 kV, resulting in currents up to 10 kA, delivers the energy needed for the experiment. The wire-shaped samples are clamped with brass electrodes and placed in the sample chamber, which is then flooded with nitrogen. A minor overpressure of 1.3 bar prevents any unwanted electrical discharge in the sample chamber. If necessary, molybdenum knife electrodes can be applied to the wire to measure the voltage drop across the sample. To start the experiment at a very precise time an ignitron in combination with a krytron is used. Such a combination is also used to precisely stop the experiment after a set time. The remainder of the energy stored in the capacitor bank is then distributed, not across the remaining metal vapour,

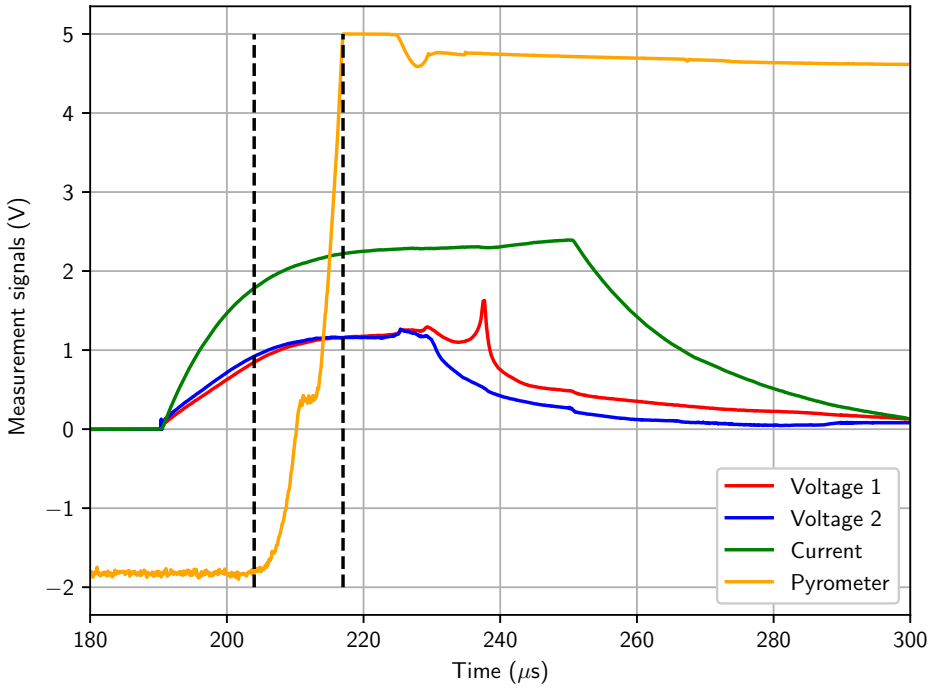

Figure 2.1.: Raw data of a typical OPA measurement. The dashed vertical lines show the region, where the pyrometer signal leaves the background noise and is not yet in saturation. The melting plateau is visible in the pyrometer data.

but rather across graphite resistors (crowbar switching). The termination of the experiment happens, depending on the material investigated, 30 µs to 80 µs after the start. These extremely short experimental durations not only guarantee a suppression of reactions of the investigated material with its surroundings but also ensure that the sample, throughout its liquid phase, does not collapse under gravity.

2.1.1. Measured Quantities

The following quantities are directly measured: the time t, the current I, the voltage drop U, the normal spectral radiance J and the radial expansion d^2/d_0^2. In combination with the Division of Amplitude Polarimeter it is also possible to determine the four Stokes parameters and with that the normal spectral emissivity (see Sec. 2.2). Figure 2.1 depicts typical raw measurement data obtained with OPA. This particular measurement was performed on the NIST SRM 1155a (see Chapter 3). Figure 2.1 shows the obvious limitation in usable data. Depending on the pyrometer used, as well as the normal spectral emissivity of the material observed at the measuring wavelength of the pyrometer, the pyrometer signal leaves the background noise at a certain temperature. While current and voltage data are available below that temperature threshold, temperature cannot be evaluated below it. The upper limit on usable data is reached, once the photo diode of the pyrometer runs into saturation. The upper limit can be shifted towards higher temperatures by adding a neutral density filter into the optical path of the pyrometer. As a neutral density filter transmits only a fraction of the incident light beam, allowing for higher temperatures to be recorded. Simultaneously, the melting plateau is shifted closer to the region of background noise. To access data lower than the temperature threshold, where the pyrometer escapes the background noise, it is possible to measure enthalpy with a DSC and match the OPA enthalpy to the DSC enthalpy (see Sec. 3.2). Figure 2.3 shows raw data for thermal expansion measurement.

Current measurement The current I is measured inductively by a Pearson™current monitor model 3025. The monitor is ring-shaped; the current carrying wire to the lower electrode of the sample chamber passes through the ring of the monitor, which leads to a change in the magnetic flux inside and, thus, a measurable voltage. Great care has to be taken to ensure electrical isolation between the measuring circuit and the discharge circuit. The current monitor is double shielded and mounted inside an aluminium box to ensure isolation.

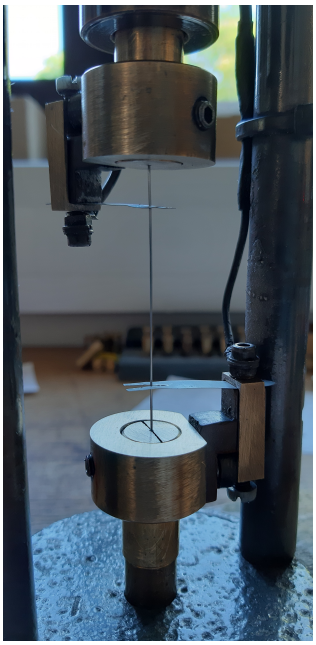

Figure 2.2.: Wire placed in the sample holder with attached voltage knives.

Voltage measurement When evaluating electrical data (electrical resistivity and electrical power) it is possible to attach voltage knives to the sample (see fig. 2.2). Note that this is not done, when measuring the Stokes parameters or the thermal expansion of the material, because the knives apply pressure to the wire, which has a negative effect on the two mentioned measurements (see [3]). The voltage knives are attached to the wire with a distance l from one to the other. The voltage drops from the knives to a common ground is measured and from the difference between these two voltage drops the voltage drop across the piece of wire of length l can be determined.

Normal spectral radiance measurement To measure normal spectral radiance, a selection of different custom-built pyrometers is used. These pyrometers contain different photo-diodes, which are sensitive in diverse temperature ranges. Table 2.1 lists all the available pyrometers at the working group. The maximum temperature of all pyrometers can be extended

Table 2.1.: Pyrometer specifications.

Number	Wavelength nm	FWHM nm	Diode	Temperature range K
1	649.7	37.2	Si	$2100 < T < 5500$
2	902.0	18.2	Si	$2000 < T < 5000$
3	1569.5	83.6	InGaAs	$1100 < T < 2500$
4	2106.7	94.0	InGaAs	$800 < T < 2000$

by adding a neutral density filter to the optical path in front of the pyrometer. The photo diode records a voltage signal that corresponds to the normal spectral radiance of the heated sample at the wavelength of the pyrometer used. It is then necessary to find a way to transfer this signal to a temperature. One way to do this would be to calibrate the pyrometer on a black body source. The pyrometer signal of a black body as a function of Temperature $J(T)$ is given by

$$J(T) = G \int_{\lambda=0}^{\infty} \tau_t \cdot r_\lambda \cdot L_{\lambda,\mathrm{BB}}(\lambda, T)\mathrm{d}\lambda \tag{2.1}$$

which includes G a geometrical factor of the setup, τ_t the transmission factor of the setup, r_λ the spectral sensitivity of the photo diode and $L_{\lambda,\mathrm{BB}}$ the normal spectral radiation of a black body emitter. Equation (2.1) does not include the normal spectral emissivity of the sample as we now consider a black body, with a normal spectral emissivity of 1. Considering Planck's law of radiation, equation (2.1) can be written as

$$J(T) = \frac{K}{\exp \frac{c_2}{\lambda_{IF} T} - 1} \tag{2.2}$$

with c_2 the second radiation constant and λ_{IF} the wavelength of the pyrometer. For a more thorough derivation the reader is referred to previous works (e.g. [4]).

K, the calibration constant[1] of the pyrometer can be determined by calibrating the pyrometer on a black body source or a secondary normal, like

[1] The term calibration constant is misleading, as K is actually a function of temperature and only constant in a first approximation.

a tungsten strip lamp. However, it is praxis to calibrate the pyrometer for each experiment during the experiment itself. This is done by identifying the melting plateau in the pyrometer signal. When a solid material reaches its melting temperature it uses additional heat applied to the material to undergo a phase transition (latent heat). The temperature does not rise and the same is true for the pyrometer signal. When the radiance temperature of the sample at its melting point is known, the melting plateau can be assigned that value and the calibration constant K is determined that way.

Thermal expansion To obtain thermal expansion, the wire is illuminated by a high power studio photo flash. Shadow images of the wire are taken during the experiment every 2.5 µs with an adapted CCD camera system. For more information the reader is referred to publications [5, 6]. From the images a cup-shaped intensity profile is obtained. Taking the full width at half maximum (FWHM), the diameter of the wire at a certain time can be evaluated. Before starting the experiment a sequence of cold images at the same time stamps as during the experiment is recorded. By dividing the diameters of the "hot" and "cold" sequences, the thermal volume expansion is given by

$$\left(\frac{V(t)}{V_0}\right) = \left(\frac{d(t)}{d(t_0)}\right)^2, \tag{2.3}$$

with $d(t)$ the diameter at time stamp t of the hot wire and $d(t_0)$ the diameter at time stamp t of the cold wire. Note: The volume expansion is equal to the radial expansion, because due to high heating rates, longitudinal expansion is suppressed and the expansion is radial only. This has been confirmed by Hüpf (see [7]).

2.1.2. Data Evaluation

A multitude of thermophysical properties are accessible with the OPA setup. We distinguish between electrical data, which are data where the Mo voltage knife electrodes are needed, and expansion data. Electrical data include enthalpy, electrical resistivity, thermal diffusivity and thermal conductivity. Expansion data are thermal expansion, density and critical

point data. Critical point data will not be discussed in this work, the reader is referred to the excellent work of Leitner [8].

Electrical Data

To evaluate electrical data, Sachsenhofer wrote a Matlab code "HOTWIRE" during his diploma thesis [9].

Enthalpy From measured electrical data $U(t)$, which is the voltage across a section of the wire with length l at time t, and the current at time t, $I(t)$, the specific heat $Q_s(t)$ at time t can be calculated

$$Q_s(t) = \frac{1}{m} \int_0^t U(t') \cdot I(t') \mathrm{d}t'. \tag{2.4}$$

The mass m is determined by measuring the length l between the two Mo voltage knife electrodes and the radius r_{RT} of the wire at room temperature. Knowing the density at room temperature D_{RT}, of the analysed material, the mass is calculated by

$$m = D_{RT} \cdot r_{RT}^2 \cdot \pi \cdot l. \tag{2.5}$$

From the definition of enthalpy H and the first law of thermodynamics, a connection between enthalpy and heat supplied to the system is made by

$$\mathrm{d}H = \mathrm{d}Q + V\mathrm{d}p. \tag{2.6}$$

For isobaric processes, like ohmic pulse-heating, the second part in eq. (2.6) is zero. Specific enthalpy can therefore directly be calculated with eq. (2.4)

$$H_s(t) = Q_s(t) = \frac{1}{m} \int_0^t U(t') \cdot I(t') \mathrm{d}t'. \tag{2.7}$$

Electrical resistivity With obtained current and voltage, the time (and later-on temperature) dependent electrical resistivity is accessible. Ohm's law states

$$U = R \cdot I, \tag{2.8}$$

voltage is resistance times current. The resistance is therefore easily accessible. The resistivity of a conducting material is defined as

$$\rho = R \cdot \frac{A}{l}, \tag{2.9}$$

with A the cross-sectional area. Combining eq. (2.8) and eq. (2.9) and using the time-dependent values obtained by OPA measurements yields

$$\rho(t) = \frac{U(t)}{I(t)} \cdot \frac{d^2 \cdot \pi}{4 \cdot l}. \tag{2.10}$$

For certain models it is convenient to use the uncorrected resistivity ρ_{IG}, which is the resistivity when assuming initial geometry and not taking into consideration the radial expansion of the wire.

$$\rho_{\mathrm{IG}}(t) = \frac{U(t)}{I(t)} \cdot \frac{d_{\mathrm{RT}}^2 \cdot \pi}{4 \cdot l} \tag{2.11}$$

When also measuring thermal expansion, the resistivity can be corrected by thermal expanison $\left(\frac{d(t)}{d_{\mathrm{RT}}}\right)^2$

$$\rho(t) = \rho_{\mathrm{IG}}(t) \cdot \left(\frac{d(t)}{d_{\mathrm{RT}}}\right)^2. \tag{2.12}$$

Thermal Conductivity With help of the "Wiedemann-Franz law" it is possible to obtain thermal conductivity of a conducting sample by OPA measurements. The Wiedemann-Franz law establishes a connection between thermal (λ) and electrical (σ) conductivity by

The Wiedemann-Franz-Law

$$\lambda = L \cdot T \cdot \sigma. \tag{2.13}$$

Here, L is the theoretical Lorentz number, which was calculated by Drude and refined by Sommerfeld in 1933 (See e.g. [10]). The theoretical Lorentz number was calculated to a value $L = 2.44 \times 10^{-8}\,\mathrm{W} \cdot \Omega \cdot \mathrm{K}^{-2}$.
The Wiedemann-Franz law was shown to work well in the liquid phase but fails in the solid phase (see e.g. [11]). This is due to the fact that the Wiedemann-Franz law was derived considering the electronic part of thermal conductivity only. In the solid phase the governing part contributing to thermal conductivity is the contribution of lattice phonons. In the liquid phase the lattice is destroyed and the governing contribution is the electric one. The lattice contribution to thermal conductivity can, however, be calculated [12] and added to the electronic part of thermal conductivity, determined with the Wiedemann-Franz law.

Thermal Diffusivity When thermal conductivity λ is known, thermal diffusivity a can be calculated by

$$a = \frac{\lambda}{c_\mathrm{p} \cdot D}. \tag{2.14}$$

Applying the Wiedemann-Franz law and inserting the temperature dependent density D, eq. (2.14) becomes

$$a = \frac{L \cdot T}{\rho_\mathrm{IG} \cdot \cancel{\left(\frac{d(T)}{d_\mathrm{RT}}\right)^2} \cdot c_\mathrm{p} \cdot D_\mathrm{RT} \cdot \cancel{\left(\frac{d_\mathrm{RT}}{d(T)}\right)^2}} = \frac{L \cdot T}{\rho_\mathrm{IG} \cdot c_\mathrm{p} \cdot D_\mathrm{RT}}. \tag{2.15}$$

Equation (2.15) is valid in the liquid phase, where conductivity is governed by electron contribution. For the solid phase, the lattice contribution to thermal conductivity has to be considered and eq. (2.14) is used to calculate thermal diffusivity.

Expansion Data

Figure 2.3 shows backlit shadow images of an unheated and heated wire. Each visible slice in the hot and cold wire pictures corresponds to a cross-section of the wire at a certain time stamp (every 2.5 µs from starting the camera). The picture acquisition system depends on a mechanically masked CCD chip, leaving only 8 pixel-rows open to exposure. The rest of the chip is used as a buffer storage. By summing over the 8 lines, a cup shaped intensity profile is obtained. Taking the full width at half maximum (FWHM) the diameter of the wire at a certain time stamp can be obtained. The ratio of the hot and cold wire picture at the same time stamp is taken to determine the radial expansion, which in the case of fast pulse-heating is equal to volume expansion.

$$\frac{V_0}{V(t)} = \left(\frac{d_0}{d(t)}\right)^2 \tag{2.16}$$

The time (and temperature) dependent density $D(t)$ can be calculated by multiplying the volume expansion with the room temperature density D_{RT}

$$D(t) = D_{\mathrm{RT}} \cdot \left(\frac{d_0}{d(t)}\right)^2 \tag{2.17}$$

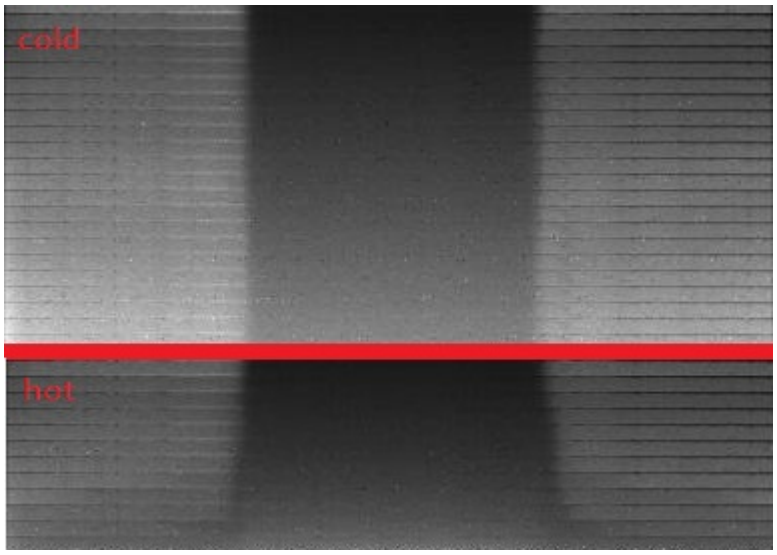

Figure 2.3.: Expansion measurement. Cold is the unheated wire and hot is the heated wire. Time progresses from top to bottom. The first and, therefore, all slices of the hot and cold wire are taken at the same time stamp. The time difference between each slice is 2.5 µs.

Temperature Evaluation

Determination of temperature is a very delicate but important task in high temperature thermophysical property measurements. Due to the high reactivity of liquid metals, contact-less temperature measurement is the status quo in thermometry. As mentioned in section 2.1.1, temperature determination is done via pyrometry.

Once a radiance trace is recorded with any pyrometer it needs to be converted into a temperature, which means the calibration factor K has to be determined by calibration. A practical method to calibrate the pyrometer is to identify the melting plateau in the signal. When the radiance temperature of the material observed is known, the calibration factor K can be determined with eq. (2.2) by

$$K(T_{\mathrm{r,m}}) = J(T_{\mathrm{r,m}}) \cdot \left(\exp\left(\frac{c_2}{\lambda \cdot T_{\mathrm{r,m}}} - 1 \right) \right). \tag{2.18}$$

Here $T_{r,m}$ is the radiance temperature at melting, c_2 is the second radiation constant and λ is the wavelength of the pyrometer.

The radiance temperature as a function of time can then be calculated by

$$T_r(t) = \frac{c_2}{\lambda \cdot \ln\left(\frac{K(T_{r,m})}{J(t)} + 1\right)}. \tag{2.19}$$

When emissivity data are available at the measuring wavelength of the pyrometer it should be included in temperature determination. The true temperature can be calculated from the radiance temperature by

The Pyrometer Correction Formula with known ϵ

$$T(t) = \frac{c_2}{\lambda \cdot \ln\left(\epsilon\left(\lambda, T_r\right) \cdot \left[\exp\left(\frac{c_2}{\lambda \cdot T_r}\right) - 1\right] + 1\right)}. \tag{2.20}$$

Unfortunately, sometimes a material is investigated, where there is no knowledge about the normal spectral emissivity at the measuring wavelength. In order to obtain an estimation of the true temperature, an assumption about emissivity has to be made. This assumption is that emissivity remains constant in the liquid phase. Under that assumption the calibration factor is calculated with eq. (2.18) but instead of the radiance temperature of the material at melting, the true temperature at melting is used.

Once temperature as a function of time is known, all thermophysical properties, which have been determined with the OPA setup, can be analysed as a function of temperature.

2.2. Division of Amplitude Polarimetry

The Divison of Amplitude Polarimeter (DOAP) was purchased in the early 2000s and has been re-established during this work. When a polarized beam of light is reflected of a (conducting) surface the state of polarisation changes. It is now possible to determine so called ellipsometric parameters, which are directly connected to the complex index of refraction and, thus, to the normal spectral emissivity of the sample. Ellipsometry[2] is a widely used technique for steady-state measurements (see e.g. [13]). For example the thickness of thin films on Si substrates can be determined with ellipsometry. An incident laser beam passes a polariser and is reflected of the thin film. The change in the polarisation of the laser beam can then be measured by rotating an analyser until the intensity drops to zero. From the change in polarisation, the thickness of the film can be determined.

Considering a very fast dynamic process, like pulse-heating, any method that relies on rotating parts to determine the state of polarisation would be significantly too slow. In 1982 Azzam suggested a method [14] to measure the four Stokes parameters, which are connected to the state of polarisation, without having to rely on moveable parts. This idea was further developed by Krishnan in 1991 [15]. The reflected incident laser beam i is divided in a reflected beam r and a transmitted beam t by a beam-splitter BS. Both the reflected beam r and the transmitted beam t then each pass a Glan-Thompson prism[3] so that a total of four divided laser beams are recorded with photo detectors. Knowing the apparatus specific calibration matrix $\mathbf{A}$, the four stokes parameters can be calculated from the four intensities by

[2]Note: Polarimetry denotes techniques, where the state of polarisation is considered for the measuring principle. Ellipsometry also considers the state of polarisation, but focuses on elliptic polarised light.

[3]In the original work of Azzam the Glan-Thompson prisms were Wollaston prisms.

The DOAP Master Equation

$$\vec{S} = \mathbf{A}^{-1}\vec{I} \tag{2.21}$$

with $\vec{S} = (S_0, S_1, S_2, S_3)$ the Stokes parameters and $\vec{I} = (I_0, I_1, I_2, I_3)$ the intensities, measured with the DOAP. Therefore, the calibration matrix $\mathbf{A}$ is a 4x4 matrix that needs to be determined in a calibration process.

The DOAP consists of three main parts: A laser, with a wavelength of 684.5 nm, the polarisation state generator (PSG) and the polarisation state detector (PSD). The laser resides in an aluminium box to shield it from the high electromagnetic pulses during the pulse-heating experiment. It is coupled into the PSG with two mirrors. The PSG is equipped with a rotatable linear polariser and a rotatable $\lambda/4$ retarder. Both can be controlled by a step motor. Note: The fact that the polariser and the retarder are rotatable is important for the process of calibration. During measurement neither of them need to be rotated and stay in a fixed position.

2.2.1. Calibration of the Division of Amplitude Polarimeter

As the calibration matrix is a 4x4 matrix, it should be sufficient to generate four linearly independent states of polarisation to calibrate the system. While this would be true for an optical system without imperfections, in reality it is best to generate more than four linearly independent polarisation states. In the so-called equator-pole (E-P) calibration, which was developed by Azzam and Lopez in 1989 [16], significantly more than four states of polarisation are generated in the process. The method is briefly described in this section:

Calibration process: Background

The calibration matrix $\mathbf{A}$ is written as

$$\mathbf{A} = \begin{pmatrix} A_{00} & A_{10} & A_{20} & A_{30} \\ A_{01} & A_{11} & A_{21} & A_{31} \\ A_{02} & A_{12} & A_{22} & A_{32} \\ A_{03} & A_{13} & A_{23} & A_{33} \end{pmatrix} = \left(\vec{A}_0, \vec{A}_1, \vec{A}_2, \vec{A}_3 \right). \tag{2.22}$$

The Stokes vector of linearly polarised light $\vec{S}_{\mathrm{LP}}$ as a function of the azimuth P is represented by

$$\vec{S}_{\mathrm{LP}} = \begin{pmatrix} 1 \\ \cos 2P \\ \sin 2P \\ 0 \end{pmatrix}. \tag{2.23}$$

Therefore, the measured intensity of incident linearly polarised light $\vec{I}_{\mathrm{LP}}$, according to eq. (2.21) is

$$I_{\mathrm{LP}} = \mathbf{A} S_{\mathrm{LP}}, \tag{2.24}$$

which yields

$$\vec{I}_{\mathrm{LP}} = \begin{pmatrix} A_{00} + \cos 2P \cdot A_{10} + \sin 2P \cdot A_{20} \\ A_{01} + \cos 2P \cdot A_{11} + \sin 2P \cdot A_{21} \\ A_{02} + \cos 2P \cdot A_{12} + \sin 2P \cdot A_{22} \\ A_{03} + \cos 2P \cdot A_{13} + \sin 2P \cdot A_{23} \end{pmatrix}. \tag{2.25}$$

The linear polariser of the PSG is rotated from $P = 0°$ to $P = 360°$ in steps of 10° and the corresponding intensity is recorded. Note: It is important that the retarder, which can be mounted on the PSG, is removed for this part of calibration process. The obtained intensity then is fitted according to eq. (2.25) with a least-squares fit and the first three rows of the calibration matrix are determined. Figure 2.4 shows the results of a (mediocre) calibration process. The different colors correspond to the four measured intensities. The markers are the measured intensities as a function of the azimuth and the lines are the corresponding least-squares fits. From visual examination of the results one can determine if a calibration is to be considered, or

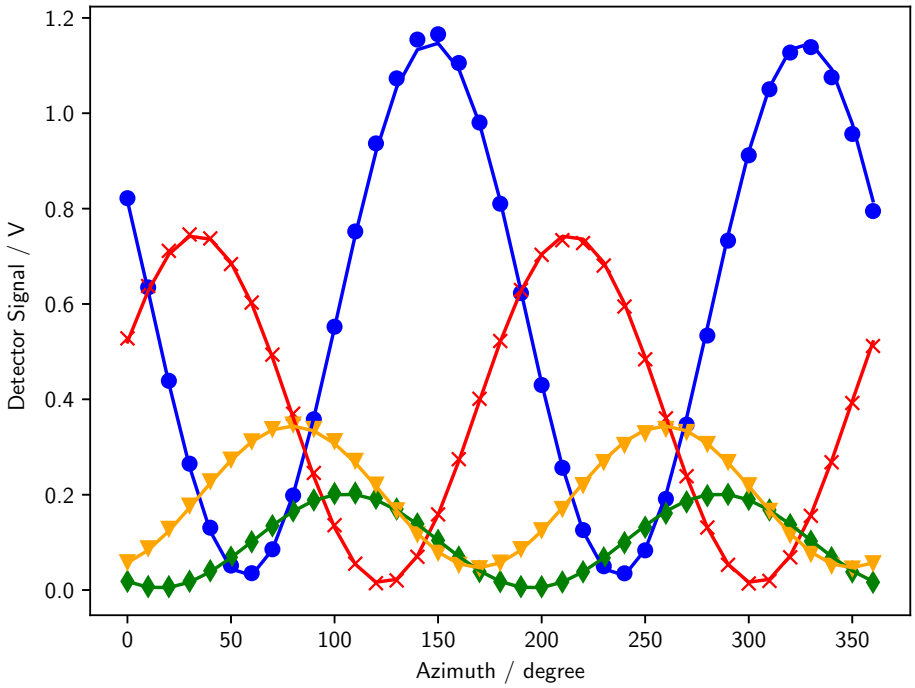

Figure 2.4.: Measured intensities (markers) and least-squares fitted intensity curves (lines) to obtain the first three columns of the calibration matrix.

discarded as bad. For the blue intensity one can identify a deviation between the measured intensities and the least-squares fit. Therefore, the calibration matrix obtained with these data needs to be discarded.

To obtain the last column of the calibration matrix, the circularly polarised states have to be taken into account. To do so, the retarder is mounted on the PSG again and the combination of linear polariser and retarder are rotated clockwise and counter-clockwise thereafter to record the intensities of the left circularly polarised (LCP) states $\vec{I}_{\mathrm{LCP}}$ as well as the intensities of the right circularly polarised (RCP) states $\vec{I}_{\mathrm{RCP}}$. In a perfect world, the intensities of the circularly polarised states are constant. However, as the optical parts of the system, and especially the retarder, are imperfect, oscillations in the circular polarised states occur. Therefore, the mean value of the LCP and RCP values are calculated. The Stokes vector of circularly polarised light is

$$S_{\mathrm{CP}} = \begin{pmatrix} 1 \\ 0 \\ 0 \\ \pm 1 \end{pmatrix}. \tag{2.26}$$

The $\pm$ in the last row corresponds to the difference between LCP and RCP[4]. Doing a matrix multiplication of eq. (2.22) and eq. (2.26) yields

$$\vec{I}_{\mathrm{RCP}} = \vec{A}_0 + \vec{A}_3 \tag{2.27}$$

and

$$\vec{I}_{\mathrm{LCP}} = \vec{A}_0 - \vec{A}_3 \tag{2.28}$$

respectively. The last column of the calibration matrix can therefore be calculated by

$$\vec{A}_3 = \frac{1}{2} \cdot \left(\vec{I}_{\mathrm{RCP}} - \vec{I}_{\mathrm{LCP}} \right). \tag{2.29}$$

Taking another look at eq. (2.27) and eq. (2.28) reveals another way to calculate the $\vec{A}_0$ column of the calibration matrix by

$$\vec{A}_0 = \frac{1}{2} \cdot \left(\vec{I}_{\mathrm{RCP}} + \vec{I}_{\mathrm{LCP}} \right), \tag{2.30}$$

[4]Note: The + is arbitrarily assigned to the RCP states and the - to the LCP states. It could also be the other way, one just has to be consistent.

this is however only used as a verification tool to check the consistency. The first column of the matrix is calculated by eq. (2.25), where a multitude of linearly polarised states is given[5].

Calibration Process: Experimental

The experimental process of calibration was described very thoroughly by Seifter [17]. However, some additional information is given here, as problems and solutions during the calibration arose during this work. Parallel to the work conducted for this thesis, Alexander Eber was working with the DOAP on his master thesis [18]. His findings are summarised as well.

The laser needs a thermalisation time of roughly four hours. The starting point of the calibration (and later on measuring) process, therefore, has to be to start up the laser and wait a minimum of four hours. During the calibration process, the so called 5th detector has to be placed in the optical path. This detector measures the intensity of the laser beam, after the PSG. If the laser were perfect, the state of polarisation would be constant over time. However, this is not the case and fluctuations in the intensity of the laser beam occur. The intensities measured with the PSD therefore have to be normalized with the intensity measured with the 5th detector. The intensity of this detector must not exceed 2 V when starting the calibration process. Seifter designed an attenuator, which is basically a combination of two rotatable linear polarisers, to moderate the incident laser beam. After passing this attenuator, the laser light is therefore linearly polarised, which leads to zero intensity after passing the PSG, if the linear polariser of the PSG is perpendicular to the state of polarisation of the incident beam. A $\lambda/4$ waveplate is placed in the optical path, just before the linear polariser of the PSG to obtain circular polarised light.

To adjust the PSD in a way that the laser spot hits the hole aperture inside, Seifter used the built-in CCD camera. The laser passed a pellicle foil that reflected a small percentage of the incoming laser light into the camera. However, during the long inactivity time of the DOAP system, this foil was

[5]The reason for this is that A the retarder is imperfect and B there are more linearly polarised states as for the circularly polarised states the mean value is used.

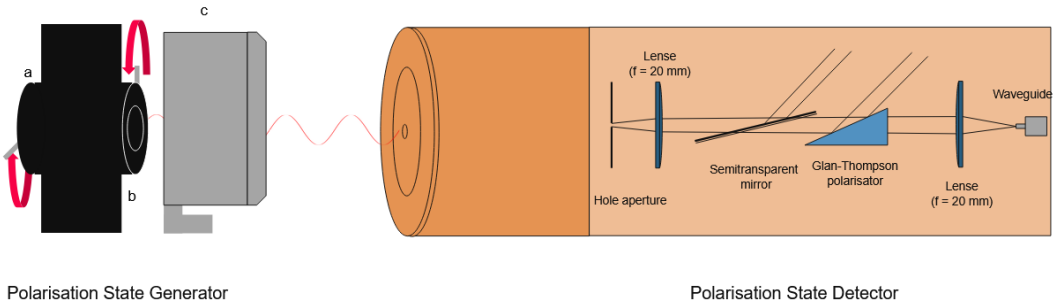

Figure 2.5.: Schematic of the DOAP in calibration mode. The rotatable linear polariser (a), the mountable retarder (b) and the 5th detector (c) are part of the PSG in calibration mode.

damaged and had to be removed (See fig. 2.6). To ensure that the laser spot hits the hole aperture, the top cover as well as the camera has to be removed. It is then possible to directly observe the hole aperture from the top.

Once the laser is coupled in and passes all the optical elements of the measuring system centrally, the $\lambda/4$ waveplate has to be rotated in a way that ensures that the intensity measured with the 5th detector is as constant as possible. When the fast axis of the $\lambda/4$ retarder is not 45° rotated to the polarisation axis of the incident laser light, the resulting state of polarisation is elliptical. This leads to oscillations of the intensity of the laser beam after passing the linear polariser of the PSG. A large oscillation of this intensity makes it impossible to achieve satisfying calibration results. Therefore, the $\lambda/4$ waveplate is pivoted in an aluminium mount and can be fixed with a grub screw. To find the minimum of oscillation, the waveplate is rotated, first in bigger steps (20°) and once a provisional minimum is found, in small steps ($< 1°$) around that provisional minimum. The whole calibration process needs to be done after every rotational step of the waveplate to obtain the intensity values, measured with the 5th detector, as a function of the azimuth P. This process is cumbersome, but finding a minimum in oscillation of the intensity of the incident laser beam is important for the quality of the calibration matrix.

Once the calibration process is satisfyingly concluded, the calibration matrix needs to be verified. To do so, the linear polariser is set to azimuth $P = 0$ and the circular polariser P_{circ} is rotated in steps of 10°. The Stokes parameters

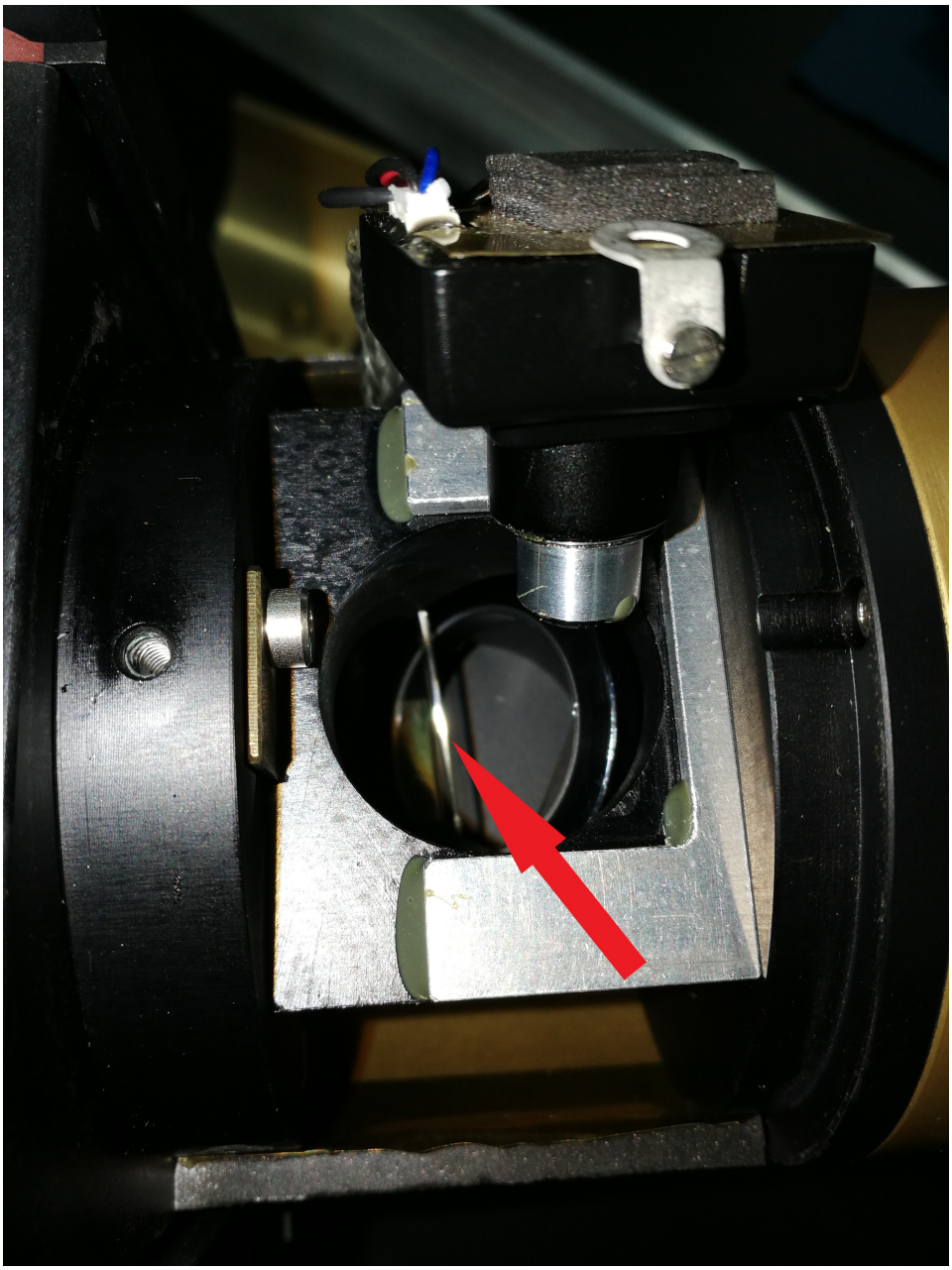

Figure 2.6.: Polarisation State Detector with removed top cover. The damaged pellicle foil is indicated by the red arrow.

are recorded with the PSD and compared to theoretical values S_{TH}:

$$S_{\mathrm{TH}} = \begin{pmatrix} 1 \\ \cos^2 2P_{\mathrm{circ}} \\ \frac{1}{2} \cdot \sin 4P_{\mathrm{circ}} \\ \sin 2P_{\mathrm{circ}} \end{pmatrix}. \tag{2.31}$$

2.2.2. Adjustment to Measuring Angle with BK7 Prism

Once the calibration and verification process is completed, the DOAP may be set up in measuring position. The PSD remains at its place, but the PSG needs to be moved to an angle 140° to the PSD. In the setup at our institute, this also means that the mirror, which couples the laser light into the PSG and which is mounted on the back side of the PSG, needs to be rotated 180°. It is handy to use a slide gauge to check if the mirror mount is parallel to the PSG. The 5th detector is removed from the optical path and the mountable lens, with a focal length $f = 170\,\mathrm{mm}$ is placed on the PSG.

Once the laser light is coupled into the PSG centrally, the BK7 prism can be adjusted. To do so, it is placed in its mounting table, that has two screws to adjust it precisely. The table is set into the holding ring, where usually the pulse-heating vessel resides. Now the PSG is moved with the two screws for translational displacement so that the beam hits the smaller of the two reflecting surfaces. The prism needs to be rotated to ensure that the laser beam is reflected perfectly. To check this, it is handy to use a small piece of paper with a hole cut in its center and place it onto the mountable lens of the PSG. If the reflection of the laser is too high, or too low, the prism is tilted. This needs to be corrected with the two screws on the prism table.

Once the laser is reflected back into itself, the PSG is moved perpendicularly to the the optical axis with the two screws for translational displacement. The laser spot now hits the larger reflecting surface and should be visible on the front of the PSD. Once the PSD is adjusted in a way that the laser hits the hole aperture the software is set to live mode. The ellipsometric parameters of BK7 are well known. If the system is set up correctly, the measured values should be very close to the theoretical values as presented in tab. 2.2.

Table 2.2.: Theoretical ellipsometric and Stokes parameters for BK7 at a wavelength of 684.5 nm under an incident angle of 70°.
S_i ... Stokes parameters,
Δ, Ψ ... Ellipsometric parameters,
n ... Index of refraction,
k ... Extinction coefficient,
ϵ ... Normal spectral emissivity,
deg$P$ ... Degree of polarisation.

Quantity	Value
S_1	-0.7588
S_2	0.6513
S_3	0
S_4	0
Δ	0
Ψ	20.31
n	1.5135
k	0
ϵ	0.958
deg$P$	1

2.2.3. Measurement

Once the system is set up, the angle between the PSG and PSD must not be altered. This means only translational displacements are allowed to adjust the PSD.

A wire is placed into the sample holder, which then is set up in the sample chamber. The PSG is moved perpendicular to the optical axis until it hits the wire. The laser spot, after hitting the wire, gets diffracted and the diffraction band hits the PSD. Now the PSD has to be adjusted, without changing the angle between PSD and PSG by translational movement only. To ensure that the maximum of the diffraction band hits the hole aperture inside the PSD, the "live mode" function of the DOAP software is used. Once the maximum is found, the perfect adjustment for measurement is achieved.

After adjustment of the pyrometer, the software is set to measuring mode and the experiment can be started.

2.3. Dynamic Scanning Calorimetry

Dynamic Scanning Calorimetry (short DSC) is a technique for thermal analysis. The area of application is manifold, however, at the Thermo- and Metalphysics Group of the Institute of Experimentalphysics at Graz University of Technology, it is mostly used to determine specific heat capacity, and in some cases, solidus and liquidus temperatures of alloys. Other applications are e.g. finding glass transition temperatures, phase transitions, purity measurements or drug analysis.

Three commercial machines are available at our group. A NETZSCH DSC 404, a NETZSCH DSC 404C Pegasus and a NETZSCH STA 449 Jupiter. The DSC 404 and its newer brother the 404C Pegasus both are heat flux DSC measuring systems.

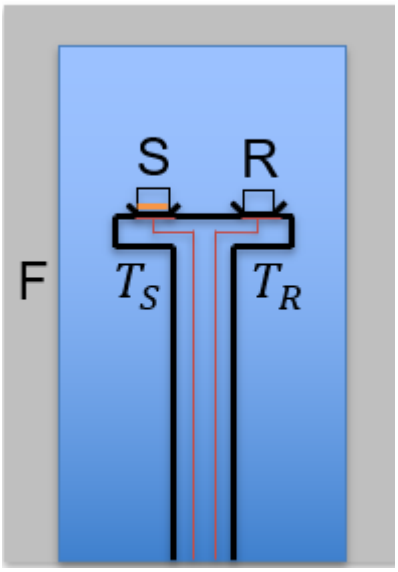

Figure 2.7.: Schematics of a heat flux DSC. F is the furnace, S is the sample crucible and R is the reference crucible.

2.3.1. Heat Flux DSC

The working principle of a heat flux DSC is explained briefly in this section. A schematic drawing of a heat flux DSC is presented in fig. 2.7. A sample holder is placed inside a furnace. The furnace is sealed and can be evacuated and flooded with a protective gas (e.g. Ar). Two crucibles reside on the sample holder, one being the sample crucible, the other being the reference crucible, which remains empty. These crucibles can be made from different materials. In our case they are usually Pt/Rh with Al_2O_3 inlets and a Pt/Rh lid with a small hole, to allow evaporating material to escape and ensure isobaric conditions. When a sample is placed in the sample crucible and the furnace heats up the chamber equally, the temperatures of the two crucibles will be different, due to the specific heat capacity of the sample. The temperatures are measured with two S-type thermocouples underneath the crucibles. From the temperature difference ΔT_{SR} between the sample temperature T_S and the reference temperature T_R, the heat flux Φ can be calculated by

$$\Phi = K(T) \cdot \Delta T_{SR}, \tag{2.32}$$

with a temperature dependent calibration factor $K(T)$ and the temperature T. The total absorbed heat Q then is

$$Q = \int_{-\infty}^{\infty} \Phi \, \mathrm{d}t. \tag{2.33}$$

Looking at the internal energy U of a closed thermodynamic system:

$$\mathrm{d}U = \mathrm{d}Q - \mathrm{d}W, \tag{2.34}$$

with the thermodynamic work W, which can be described by

$$\mathrm{d}W = F\mathrm{d}x = \frac{F}{A}\mathrm{d}A = p\mathrm{d}V, \tag{2.35}$$

representing a constant force F acting on a body with a surface A and displacing the body a distance x. Here p is the pressure acting on the body.

$$\mathrm{d}U = \mathrm{d}Q - p\mathrm{d}V \tag{2.36}$$

As the process is isobaric, the enthalpy H as a thermodynamic potential may be used

$$\mathrm{d}H = \mathrm{d}U + p\mathrm{d}V + V\mathrm{d}p = \mathrm{d}Q + V\mathrm{d}p = \mathrm{d}Q. \tag{2.37}$$

When the calibration factor $K(T)$ is known, the specific heat capacity c_p can be determined from the absorbed heat Q by

$$c_\mathrm{p} = \left(\frac{\mathrm{d}H}{\mathrm{d}T}\right) = \left(\frac{\mathrm{d}Q}{\mathrm{d}T}\right). \tag{2.38}$$

It is possible to determine the calibration factor $K(T)$ by melting materials with well known thermophysical properties, like the specific enthalpy of fusion, however, a different method to determine the specific heat capacity c_p is often used.

2.3.2. Measuring Principle

To determine specific heat capacity, three consecutive measurements have to be performed. The first measuring run is done with empty crucibles. This

is necessary, because no system is perfect. Crucibles have different masses, the thermal contact between the crucible floor and the sample holder is imperfect or even the thermocouples may not react equally. In a perfectly adjusted measuring system, the baseline (which is the measurement run with empty crucibles) would be a flat zero line. However, this is not the case for real systems. By adjusting the position of the sample holder in the furnace and choosing crucibles with similar weights, it is possible to achieve low baselines, but not zero ones. A good value for a baseline is a deviation of less than 2 µV from zero across the full temperature range. Once the baseline is recorded for the measurement, a sapphire disc is placed in the sample crucible. Specific heat capacity of sapphire is a well known function of temperature and sapphire discs with different masses can be purchased from NETZSCH. Once the sapphire run is completed, the sample is placed in the sample crucible and the measurement is repeated. Note: All measurement runs (Baseline, Reference, Sample) have to be performed with the same temperature profile. After completion of all three runs, three DSC curves are obtained (See tab. 2.3). The specific heat capacity of the sample

Table 2.3.: DSC curves obtained for one measurement

Number	Type	Symbol
1	Baseline	Φ_B
2	Reference	Φ_R
3	Sample	Φ_S

$c_{p,S}$ can be calculated with m_R the mass of the reference material, m_S the sample mass, $c_{p,R}$ the specific heat capacity of the reference material, Φ_S the DSC signal of the sample, Φ_R the DSC signal of the reference material and Φ_B the baseline by

THE DSC WORKING EQUATION

$$c_{p,S} = \frac{m_R}{m_S} \cdot c_{p,R} \cdot \frac{\Phi_S - \Phi_B}{\Phi_R - \Phi_B} \tag{2.39}$$

Data evaluation is performed with the NETZSCH Proteus software.

2.4. Electromagnetic Levitation

Electromagnetic levitation (EML) in combination with the Oscillating Drop (OD) method provides a useful technique to measure temperature dependent surface tension and density of a metallic melt. A conducting sample, which is placed in an inhomogeneous electromagnetic field, is levitated and heated up until it melts. The sample performs oscillations, with the driving force being the surface tension of the material. Electromagnetic levitation was suggested as early as 1923 by Muck [19] and three decades later, first experimental results were published by Okress et. al.[20].

2.4.1. Levitation Principle

The alternating current through the levitation coil produces an electromagnetic field with magnetic induction $\vec{B}$. Once a metallic sample is placed in the coil, eddy currents are induced in the sample, generating an opposing electromagnetic field. By performing a Taylor series of the external magnetic field in the region of the metallic sample, the Lorentz force acting on the sample is

$$\vec{F} = -\text{grad}(\vec{m} \cdot \vec{B}), \tag{2.40}$$

with $\vec{m}$ being the magnetic dipole moment of the metallic sample. The time-averaged field of a conducting metallic sphere in a sinusoidal alternating field [21] reads (simplified) as [22]

$$\overline{\vec{F}} = -\frac{\pi R^3}{\mu_0} f(g(R,\sigma)) \cdot \mathrm{grad}\vec{B}^2, \tag{2.41}$$

with f, g functions of the sample radius R and the electrical conductivity σ of the metallic sphere. According to (2.41), the levitational force is therefore proportional to the gradient of the magnetic induction $\vec{B}$. However, the time averaged electrical power $\overline{P}$ reads as [21, 22]

$$\overline{P} = \frac{3\pi R}{\sigma\mu_0^2} h(g(R,\sigma))\vec{B}^2, \tag{2.42}$$

with h, g again functions of R the radius and σ the electrical conductivity of the specimen. Equations (2.41) and (2.42) show that for terrestrial levitation apparatus, levitation force and heating power originate from the same electromagnetic field. It is not possible to levitate the sample without simultaneously heating it up and vice versa. Thus, it is impossible to observe levitating samples quickly cooling down, by shutting off the heating power. Similarly, as long as the levitating field is turned on, surface oscillations are excited. Measurement of viscosity is therefore not accessible by EML measurements under earth's gravity, because the natural damping of the surface oscillations as a function of time would need to be investigated for this purpose.

2.4.2. Oscillating Drop Method

The oscillating drop method (OD) is a method to determine surface tension from a levitated, liquid (deformed) sphere, moving around and oscillating with some frequencies. The deviations from spherical form, due to surface oscillations, can be described by spherical harmonics

Spherical Harmonics

$$\delta R(\theta, \phi, t) = \sum_{l \geq 0} \sum_{m=-l}^{m=+l} a_{l,m}(t) \mathrm{Y}_m^l(\theta, \phi) \tag{2.43}$$

Here $\mathrm{Y}_m^l(\theta, \phi)$ are the spherical harmonics as a function of the polar angle θ and the azimuth ϕ, $a_{l,m}(t)$ are time dependent coefficients. The order of the spherical harmonics is given by l and the degree by m. The oscillations of a liquid drop are linked to the surface tension of the material. While the shape of the droplet can be approximated by superposition of several oscillation modes, the majority can be neglected. For example, mode $l = 0$ requires a change in radius, which is not allowed when assuming incompressible materials. According to Cummings and Blackburn [23], the $l = 1$ mode does not relate to deformation of the surface, but rather a translation of the center of mass and is therefore not considered in the calculations. Any modes $l \geq 3$ are significantly too small in amplitude and are therefore also neglected. Thus, only the $l = 2$ modes remain in the calculations.

Lord Rayleigh published a connection between the surface oscillation ω of a spherical, non-rotating, unconstrained liquid (Rayleigh described water) to its surface tension γ and mass M [24]:

$$\omega_l^2 = l(l-1)(l+2) \cdot \frac{4}{3} \cdot \frac{\pi \cdot \gamma}{M} \tag{2.44}$$

As described above, only the $l = 2$ stay in consideration. Surface tension is connected to the fundamental frequency (Rayleigh frequency) $\nu_\mathrm{R} = \omega_\mathrm{R}/2\pi$ by eq. (2.44) with the

Rayleigh Equation

$$\gamma = \frac{3}{8} \cdot \pi \cdot M \cdot \nu_{\mathrm{R}}^2. \tag{2.45}$$

Again it has to be noted that eq. (2.44) was derived for spherical, non-rotating, unconstrained drops of water. When performing EML on ground, and under the influence of gravity, the sample gets deformed to a droplet-like shape. As eq. (2.44) shows no dependence on the order m, the obtained frequency is degenerated. For the $l = 2$ modes this corresponds to a 5-fold degeneracy. However, as eq. (2.44) does not hold under the influence of gravity, this degeneration is lifted for terrestrial experiments, resulting in 5 distinguishable peaks in the frequency spectrum when performing experiments under the influence of gravity.

Cummings and Blackburn derived a correction to the Rayleigh frequency ω_{R} for terrestrial EML experiments [23]

$$\omega_{\mathrm{R}}^2 = \frac{1}{5} \cdot \left(\omega_{2,0}^2 + 2 \cdot \omega_{2,|\pm 1|}^2 + 2 \cdot \omega_{2,|\pm 2|}^2 \right) - \overline{\omega}_t^2 \left(1.90 + 1.20 \cdot \frac{z_0}{R} \right)^2, \tag{2.46}$$

with $\omega_{2,|\pm l|}^2$ the angular velocities of the respective modes, R the radius and

$$z_0 = \frac{g}{2 \cdot \overline{\omega}_t^2}, \tag{2.47}$$

with the gravity g and the mean square of the translation frequency $\overline{\omega}_t^2$.

2.4.3. Experimental Details

The heart of the EML apparatus is the vacuum chamber, where the sample holder and the coil reside. It is connected to a rotary vein pump and a turbomolecular pump to achieve a vacuum with ambient pressures down to

5×10^{-6} mbar. The vacuum chamber is also attached to an ambient gas system. A variety of four different high purity gases are available: ALPHAGAZ 1 Ar, ARCAL 10, ALPHAGAZ 2 He and a mixture of He + 4%$_{\text{vol}}$$H_2$. The coil is connected to a high frequency generator with a frequency of approximately 380 kHz. The whole electrical circuit is water-cooled. The temperature is recorded with a commercial pyrometer (LumaSense Technologies, IMPAC IGA 6 Advanced). Imaging is performed with two fast cameras, one mounted at the top (Microtron EoSens CL, allowing a frame capturing rate of 506 fps at full resolution), monitoring the top surface of the sample, the other at the side (Basler avA1000-120km, allowing a frame capturing rate of 120 fps at full resolution) to observe the side surface. The top camera is used to determine surface tension, the side camera is used to determine density. More information on the setup can be found in [25].

2.4.4. Data Evaluation

Surface Tension

Surface tension is obtained by analysing video images of the oscillating sample from the top view. Performing an edge detection algorithm on the single frames of the video allows to determine the center of mass and an arbitrary number of radii as a function of time. Data for every frame in the video contains the center of mass in the x-y plane, radii from the center of mass to the edge of the sample in steps of 5° and the total number of pixels associated with the sample surface. The translation frequencies in x- and y-direction $\nu_{t,x}$ and $\nu_{t,y}$ can be easily obtained by performing a Fourier Transformation on the x and y coordinates of the sample's center of mass. The translation frequency in z-direction $\nu_{t,z}$ is not directly observable, as that would require video data in the x-z or y-z plane. However, it is possible to estimate $\nu_{t,z}$ from

$$\nu_{t,z} = 2 \cdot \nu_{t,y} = 2 \cdot \nu_{t,x}, \tag{2.48}$$

if the magnetic field shows a linearity along the z-axis.

Performing Fourier transformations on an arbitrary radius R_i and the radius perpendicular to it $R_{i+90°}$ as well as the Fourier transformation of the sum

and difference between these radii allows the determination of the oscillation frequencies of the $l = 2$ modes. A more thorough explanation can be found in the Master thesis of *A. Werkovits* [26] or *O. Klemmer* [27].

Density

As density data, obtained with EML measurements, are not presented in this work, the reader is referred to previous theses, e.g. [3, 25–27], for an explanation on density determination.

2.5. TEMPUS - Tiegelfreies Elektromagnetisches Prozessieren von Proben unter Schwerelosigkeit

In this section the TEMPUS (Tiegelfreies Elektromagnetisches Prozessieren von Proben unter Schwerelosigkeit) facility is explained. TEMPUS was designed and built by the Deutsche Zentrum für Luft- und Raumfahrt (DLR) in 1991 [28]. TEMPUS provides an electromagnetic levitation technique under microgravity conditions on-board of the International Space Station (ISS) and on-board of parabolic flights.

2.5.1. Measurement and Data Evaluation

As explained in section 2.4, when performing electromagnetic levitation measurements on ground, the electromagnetic field, responsible for levitating the metallic sample, also heats the sample and is responsible for exciting surface oscillations. Therefore, it is not possible to determine viscosity with electromagnetic levitation on ground. Once the field is shut down, the levitation force vanishes and the sample drops due to gravity. In microgravity, no levitation force is needed, thanks to the lack of gravity. The levitating sample only needs to be held in place with a positioning electromagnetic field. With TEMPUS, viscosity measurements are possible,

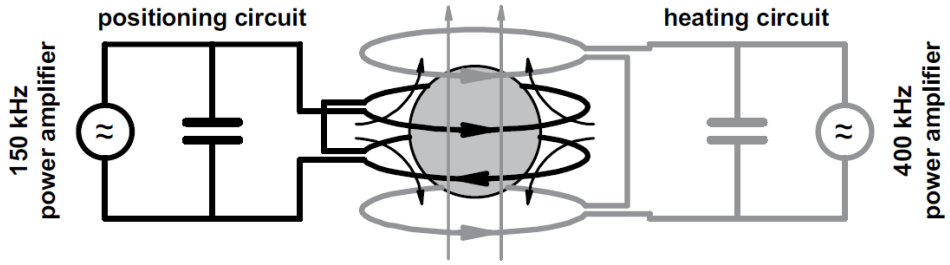

Figure 2.8.: Schematic drawing of the TEMPUS facility. Picture adapted from [29].

additional to surface tension measurements. Figure 2.8 shows a schematic of the TEMPUS facility. Contrary to on ground EML, TEMPUS uses two decoupled circuits: One circuit that produces a quadrupole shaped field, which is used to position the weightless sample, and another circuit that produces a dipole shaped field, which is used to inductively heat the sample (see [29]). The advantage of this setup is that the positioning circuit has very little heating power, while the heating circuit does not influence the positioning of the sample. Once the heating circuit is turned off, the sample cools down and allows to measure the viscosity from the observed dampening of surface oscillations. Measurements are performed under UHV conditions. Therefore, materials with high vapour pressures (e.g. manganese), are not suitable for measurement with TEMPUS.

Temperature Measurement

Temperature measurement with TEMPUS is performed via two-color pyrometry. The advantage of a two-color pyrometer over a pyrometer with one wavelength is that the often unknown behaviour of emissivity as a function of temperature and wavelength $\epsilon(\lambda, T)$ can be neglected by taking the radiation ratio [30]. The pyrometer operates in a temperature range from 300 °C to 2400 °C and has a measuring frequency of 1×10^5 Hz. Due to the UHV conditions, evaporation is a considerable factor. The apparatus is designed in a way, that evaporating material does not deploy on the pyrometer lens, which would lead to an apparent lowering of the temperature. Instead, the sample radiation is coupled into the pyrometer by a

set of mirrors. The reflectivity of the mirrors is often not changed by the evaporated material, as described by Neuhaus et. al. [31]. More details of the temperature measurement with TEMPUS can be found in [28].

Surface Tension and Viscosity Measurement

To measure surface tension in microgravity with the TEMPUS apparatus, the oscillating drop method can be used. The surface oscillations of the samples are recorded with a high speed camera with a frame rate of 500 Hz. By identifying the change in radius of the sample from the obtained pictures and performing a Fourier transformation, the oscillations are accessible in the frequency space. Identifying the position of the single peak (unlike for terrestrial experiments, experiments in microgravity show a 5-fold degeneracy of the $l = 2$ mode, thus, a single peak is displayed) in frequency space allows the determination of surface tension according to eq. (2.45).

Identifying the time constant of the decaying oscillations gives access to the viscosity of the sample. According to Lamb's equation [32], the viscosity η is

Lamb's Equation

$$\eta = \frac{3}{20 \cdot \pi} \cdot \frac{M}{R} \tau^{-1}. \tag{2.49}$$

Here, M is the mass of the sample, R is the radius of the unperturbed sample and τ is the time constant, which can be determined by fitting the time-dependent oscillation amplitude by

$$r(t) = r_0 + A \cdot \sin(\omega \cdot t + \phi) \cdot \exp\left(-\frac{t}{\tau}\right) \tag{2.50}$$

2.5.2. Sample Coupling Electronics (SCE)

Additionally, it is possible to determine radius changes inductively with the "Sample Coupling Electronics (SCE)" [29]. A schematic drawing of the TEMPUS heating circuit with sample coupling electronics is presented in fig. 2.9.

The impedance of the capacitor $Z_{\text{cap}} = \frac{1}{i\omega C}$ and the impedance of the coil $Z_{\text{coil}} = R + i\omega L$ can be determined by a calibration measurement of R, L and C without a sample.

$$\frac{I_0}{U_0} \cdot \exp(-i\phi) = \frac{1}{Z_{\text{cap}}(\omega) + \frac{1}{Z_{\text{coil}}} + Z_{\text{sample}}(\omega, \rho, a)}, \tag{2.51}$$

makes a connection between the amplitude of the alternating voltage drop U_0, the amplitude of the alternating current I_0 (across and over the levitation circuit) and the impedances of the capacitor $Z_{\text{cap}} = \frac{1}{i\omega C}$, the coil $Z_{\text{coil}} = R + i\omega L$ and the impedance of the sample $Z_{\text{sample}}(\omega, \rho, a)$. Here, ϕ is the phase difference between voltage and current, ω is the angular frequency of voltage and current, ρ is the sample's resistivity and a the sample's radius. It is therefore possible to determine the sample's radius and resistivity by measuring I_0 and U_0, as well as the phase difference ϕ and the angular frequency ω. Given the time-dependent radius of the sample as well as the pyrometer signal as a function of temperature, it is possible to determine the oscillation frequency and the time constant of the dampening to obtain surface tension and viscosity. The evaluation routine is explained in the following section.

Data Reduction SCE

The data reduction process shown in this section has been proposed by Dr. Georg Lohöfer, to whom I would like to express my gratitude. Figure 2.10 shows an experiment from one parabola. Indicated by the red lines, three heating pulses are visible. During the first, broader, pulse, the sample melts and can be investigated during the two narrower pulses. The resonance circuit frequency is plotted in blue and the pyrometer trace is plotted in

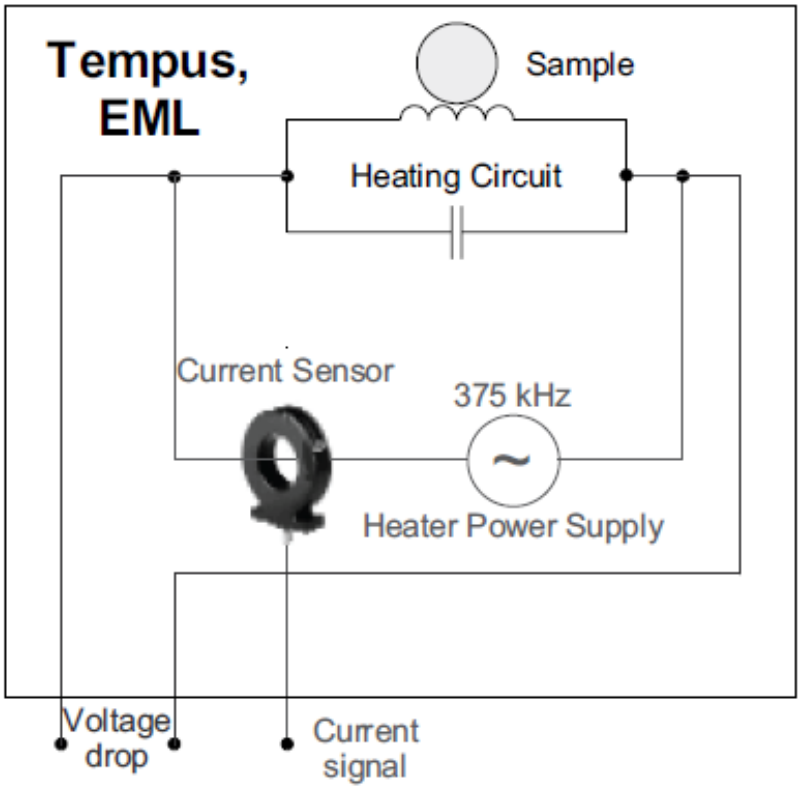

Figure 2.9.: Schematic drawing of the TEMPUS heating circuit with sample coupling electronics. Figure adapted from [29].

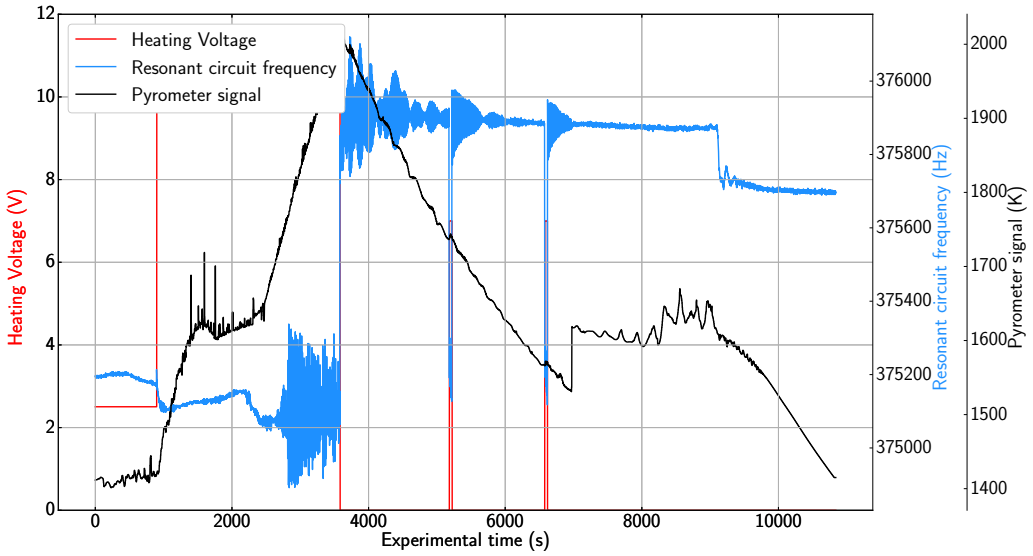

Figure 2.10.: SCE data from one parabola. The red line shows the heating voltage. Three pulses are performed during each parabola. The blue line shows the resonance circuit frequency, from which the sample radius can be determined. The black line shows the pyrometer signal.

black. It is visible that the sample gets excited to oscillate by the pulses and the oscillations dampen after the pulse. The first step is to cut out the oscillations corresponding to one pulse. This is shown in figure 2.11. The figures now show plots as a function of "reset experimental time". This means that the new time zero corresponds to the starting point of the cut-out pulse. To determine the sample radius, the mean resonant circuit frequency has to be determined and subtracted from the oscillations. This is done by fitting an exponential function to the resonant frequency data. Additionally, the sample temperature, which has already been corrected to the true temperature, is plotted in blue. To deal with the changing emissivity of the surface, due to oxides, the sample temperature is fitted linearly. Once the mean resonant circuit frequency is determined and subtracted from the oscillations, the sample radius in arbitrary units can be plotted. This is depicted in fig. 2.12. In order to determine the time constant of the dampening, the absolute value of the sample radius can be plotted and fitted linearly. The reciprocal value of the slope of the linear fit is the time

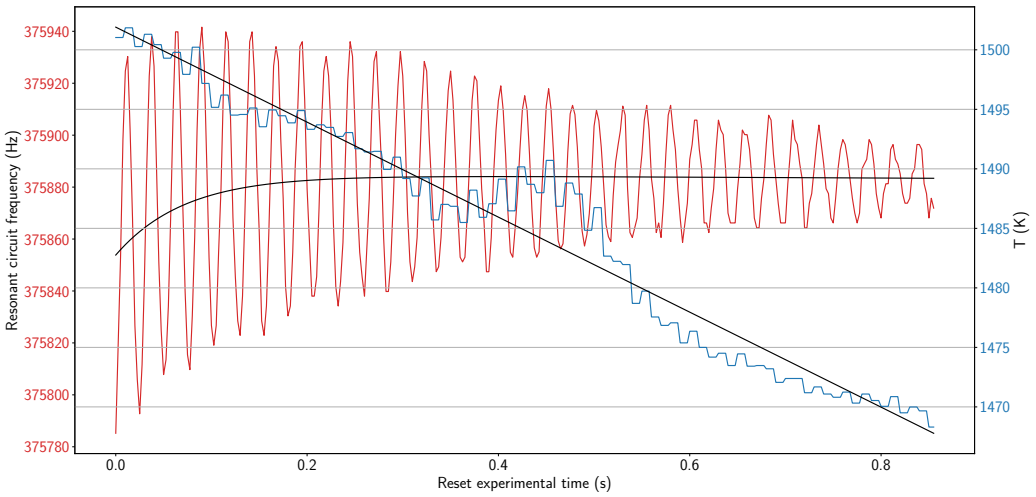

Figure 2.11.: Cut-out pulse data. The red line is the oscillating resonance circuit frequency. The black exponential line represents the mean resonance circuit frequency. The blue line is the true temperature of the sample, which is fitted linearly, represented by the linear black line.

constant. This is shown in fig. 2.13. As visible in fig. 2.11, the temperature reduces drastically during one pulse. It has therefore been suggested by Dr. Xiao Xiao that the pulse has to be divided into overlapping parts. An example for this is shown in fig. 2.14. The pulse data are divided into a green, a red and a blue part, where each adjoining parts overlap for some data points. Each part is fitted separately with a damped sine function

$$a(t) = y_0 + A \cdot \exp\left(-\frac{t}{\tau}\right) \cdot \sin\left(\pi \cdot \frac{(t - t_c)}{\omega}\right). \tag{2.52}$$

With eq. (2.52) not only the time constant τ is accessible, but also the oscillation frequency ω. For each segment, a temperature according to the linear fit, seen in fig. 2.11 can be attributed. Thus, it is possible to achieve a better temperature resolution for each pulse. However, in some cases the sample oscillates two frequencies that are very close to each other. The result is a beat and somewhat deformed oscillation data of the radius.

In order to deal with situations like this, one possibility is to fit the changing

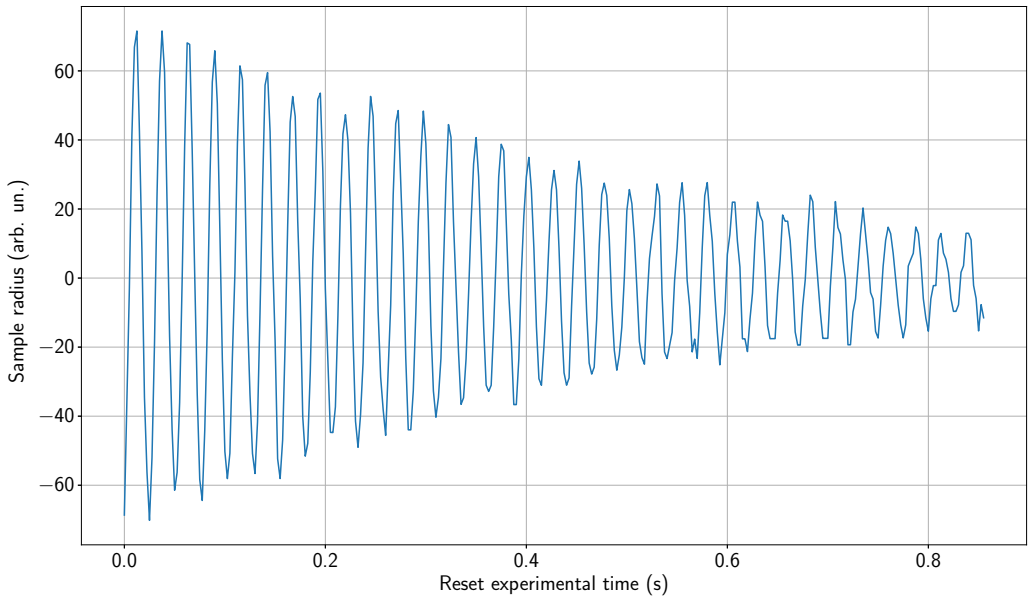

Figure 2.12.: The sample radius in arbitrary units as a function of time. The mean resonance circuit frequency has been subtracted from the oscillating resonance circuit frequency.

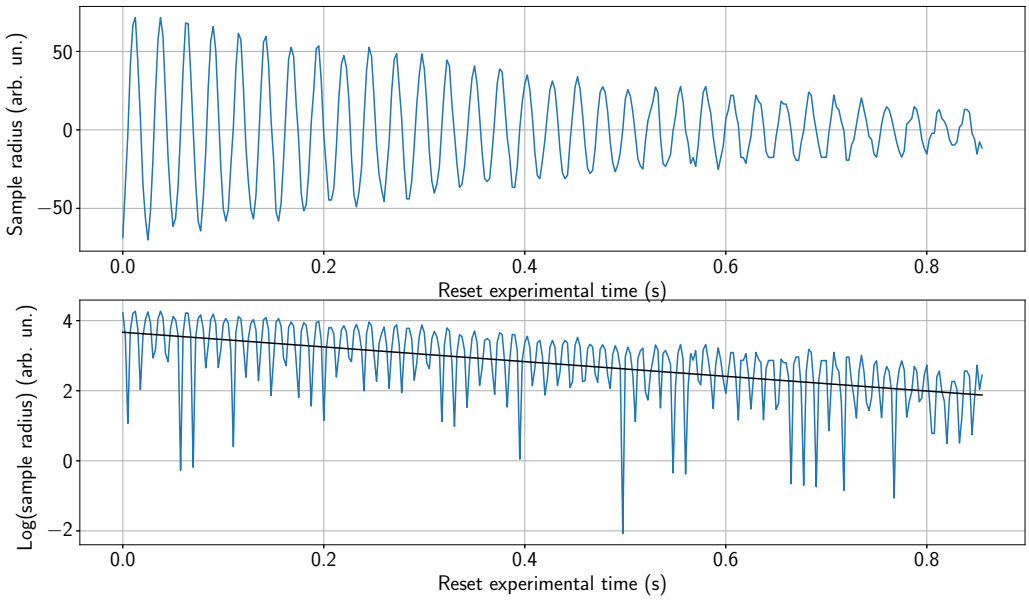

Figure 2.13.: The absolute value of the sample radius, plotted logarithmically. The data have been fitted by a linear regression to obtain the time constant.

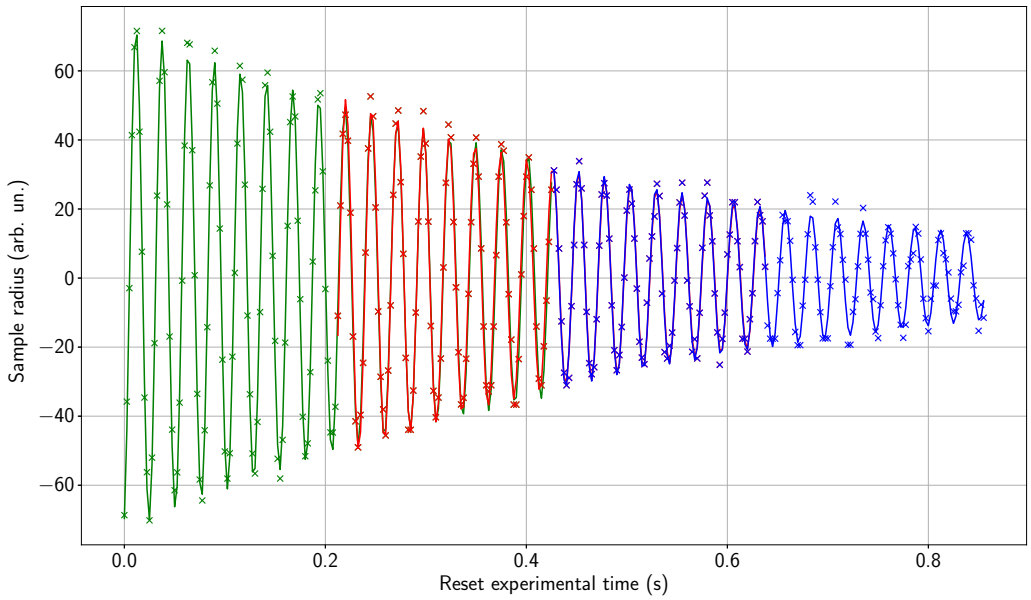

Figure 2.14.: The sample radius as a function of time. The crosses mark the measured SCE data, the lines are fitted damped sine functions. The pulse has been divided into three overlapping parts.

radius $\Delta a(t)$ as a function of time with

$$\Delta a(t) = A \cdot \exp\left(-\frac{t}{t_0}\right) \cdot \sin\left[\pi\left(\frac{t-t_A}{\omega_A}\right)\right] \cdot \sin\left[\pi\left(\frac{t-t_B}{\omega_B}\right)\right], \quad (2.53)$$

representing a superposition of two sine functions with two frequencies ω_A and ω_B. As there are now six parameters that need to be optimized numerically, it is advisable to try to reduce the number of parameters. This can be done by taking the square of eq. (2.53)

$$\begin{aligned}\Delta a^2(t) = \quad & A^2 \exp\left(-\frac{2t}{t_0}\right) \sin^2\left[\pi\left(\frac{t-t_A}{\omega_A}\right)\right] \sin^2\left[\pi\left(\frac{t-t_B}{\omega_B}\right)\right] \\ = \quad & A^2 \exp\left(-\frac{2t}{t_0}\right) \frac{1}{2}\left\{1 - \sin\left[2\pi\left(\frac{t-t'_A}{\omega_A}\right)\right]\right\} \\ & \frac{1}{2}\left\{1 - \sin\left[2\pi\left(\frac{t-t'_B}{\omega_B}\right)\right]\right\}. \quad (2.54)\end{aligned}$$

The next step is to consider the fast oscillations as noise and take the average over them. By doing so eq. (2.54) yields

$$\left\langle \Delta a^2(t) \right\rangle = \frac{A^2}{4} \exp\left(-\frac{2t}{t_0}\right) \left\{1 - \sin\left[2\pi\left(\frac{t-t'_A}{\omega_A}\right)\right]\right\}. \quad (2.55)$$

With eq. (2.55) it is now possible to determine the time constant and, thus, viscosity, when dealing with pulses that display a beat-like behavior, as shown in fig. 2.15. As the fast oscillations are taken out of the equation, it is not possible to determine surface tension with this formalism. One way to obtain surface tension values from these types of data is to perform a FFT on the oscillations, or to fit them with one sine function in order to determine the oscillation frequency only.

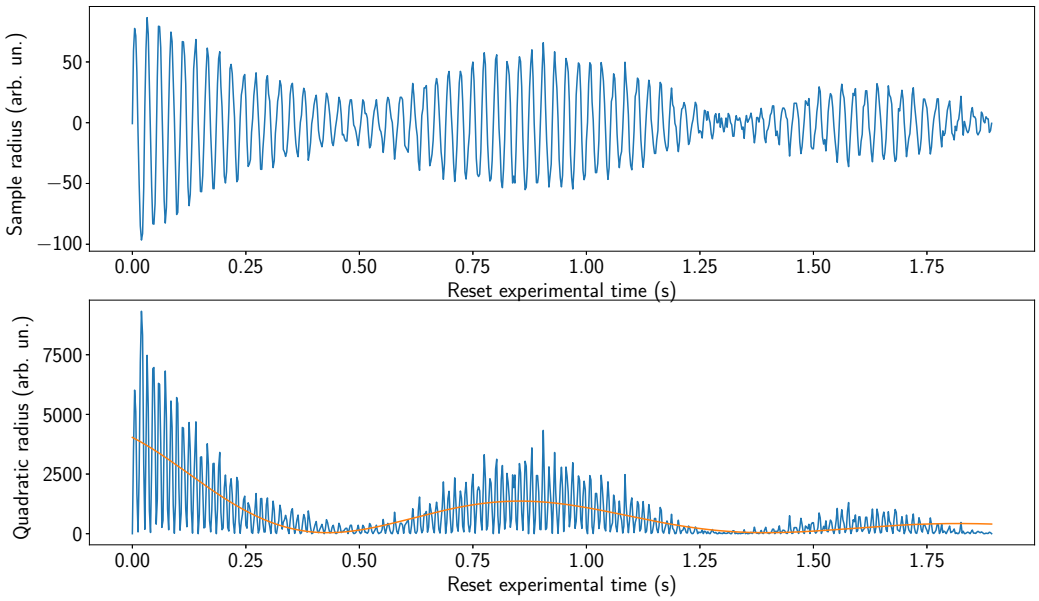

Figure 2.15.: Oscillation data of a pulse that displays beat. The upper image shows the oscillating radius. The lower image is the squared oscillation data, fitted with two oscillation frequencies.

2.6. Electrostatic Levitation Furnace on-board the International Space Station (KIBO Module)

Another levitation technique to obtain thermophysical properties is electrostatic levitation (ESL). Contrary to EML, where an inhomogeneous, oscillating magnetic field is applied, ESL utilizes an electrostatic field, which is applied by an arrangement of electrodes and requires feedback control to account to changes in the sample position. A great advantage of ESL over EML is the fact that with ESL, successful levitation is dependent on the surface charge of the sample, but not on eddy currents induced in a conducting sample, as it is the case for EML apparatus. Therefore, a multitude of materials, including metals, alloys, semiconductors and ceramics can be processed with ESL techniques. Another advantage of ESL methods is that levitation and sample heating are decoupled. The sample could be levitated by applying an electrostatic field which does not heat up the sample and utilizing a powerful laser to heat it. ESL experiments are often conducted in high vacuum, which has obvious disadvantages: Samples with high vapour pressures (e.g. Mn, Cr) evaporate easily in high vacuum conditions.

One of the two major advantages to ELF, compared to ground-based EML and ESL experiments are that the sample is spherical, which means that it follows theoretical models better. Samples in EML experiments are always slightly deformed due to the inhomogeneous levitation field, even in microgravity. The second advantage of the ELF apparatus is the placement of the lasers, which are arranged in a tetrahedron. This arrangement ensures a more uniform heating across the entire surface, limiting possible Marangoni convection, a problem that occurs in ground-based ESL measurements, where the lasers heat the sample from one side only. In EML apparatus, convection is always present, due to the levitation field, even in microgravity. Based on the work by Rhim et al. in 1993 [33], ESL techniques have been refined and the Japanese Aerospace Exploration Agency (JAXA) developed their Electrostatic Levitation Furnace (ELF), which has been launched to the ISS in 2016 by two flights (HTV-5 and OA-4) [34].

2.6.1. Experimental Details

The ELF is installed in the Multi-Purpose Small Payload Rack (MSPR-2) in the Japanese Experimentation module Kibo. The sample cartridge, into which the sample holder, with up to 20 samples can be inserted, as well as the experimental chamber, is installed in the work volume (WV) of the MSPR-2. The electrodes, in-between the sample is levitated, reside in the sample cartridge. To bring the sample into the levitation field, two rods are available, which push the sample into the center of the chamber. ESL methods, unlike EML methods require a real-time positioning system. In EML methods the field applied creates a potential well, which contains the sample. This is not the case with ESL methods. Gravity on the ISS plays a different role than what one has to deal with on earth. While there is no big gravity vector pointing towards the center of the earth, any heavy object surrounding the measurement system effects the sample with gravitational pull. To counteract these effects, a positioning system is needed. This system consists of two orthogonally positioned He-Ne lasers (wavelength 638 nm), which project shadow images onto a sensor, that measures vertical and horizontal positions. This setup has been previously described by Rhim et al. [33]. Additional information can be found in [34]. Six equally sized electrodes reside in the sample cartridge. The voltages distributed over these electrodes are connected to the positioning system to ensure a stable sample position.

To melt and heat the sample, four semiconductor lasers with a wavelength of 980 nm and a power of 40 W are distributed in the experimental chamber. These lasers can be controlled from the ground-based experiment controller. Temperature is measured with a commercial pyrometer in a range from 300 °C to 3000 °C. Two cameras observing the sample are used for density measurement (black and white camera with 60 Hz imaging resolution) as well as observing the overall behaviour of the sample.

Surface tension and viscosity can be measured by means of the oscillating drop method. To excite the surface oscillations, a sinusoidal electrical field is superimposed for a short time. The decaying oscillation amplitude is measured by collimating a laser beam, which creates a shadow image of the sample onto a photo detector. From fluctuations of the laser power,

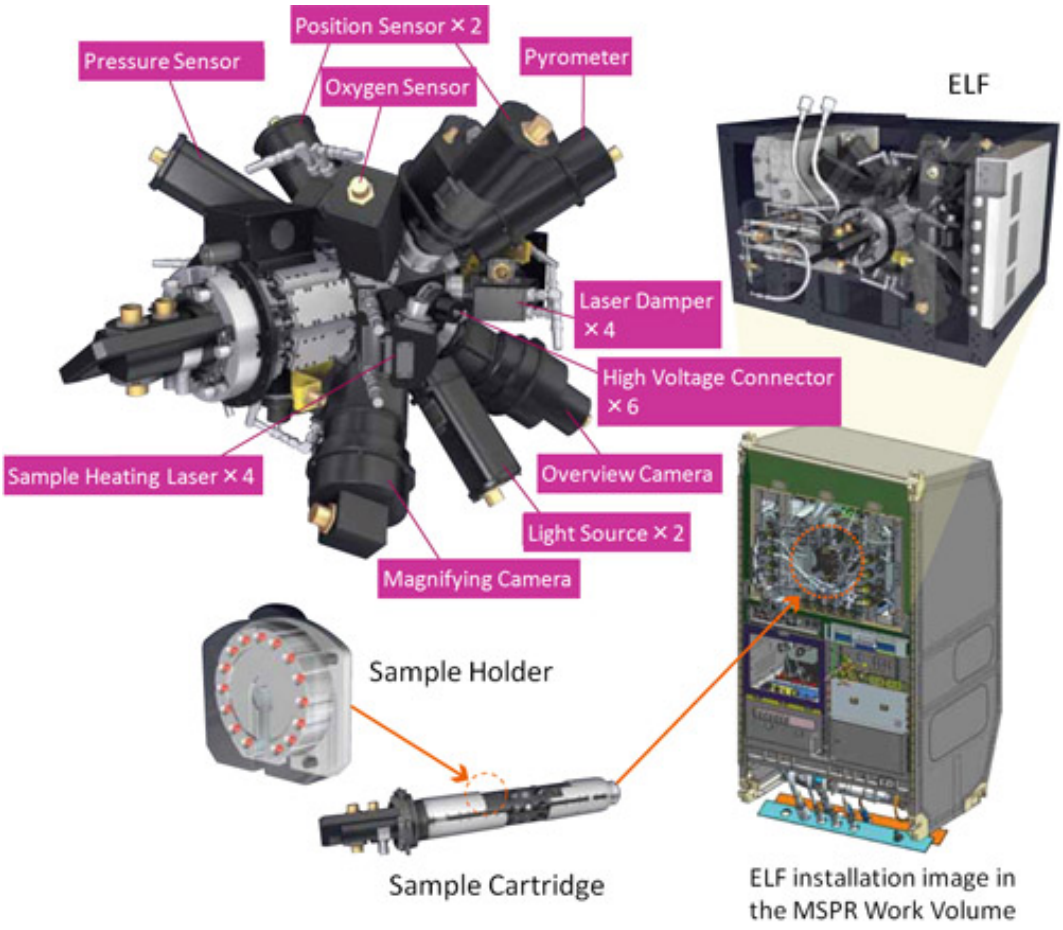

Figure 2.16.: Drawing of the ISS-ELF experimental chamber, sample holder, sample cartridge and ELF installation in the MSPR work volume. Picture adapted from [35].

measured with that detector, the oscillation frequency and the decay time constant can be determined. A part of the apparatus is an UV lamp. This lamp functions not only as a background light for the shadow images, taken with the black-white camera for density measurements, but also maintains the charge of the sample thanks to the photoelectric effect[6]. The UV lamp resides in the small experiment area (SEA) of the MSPR-2.

The sample cartridge needs to be inserted into the chamber by the crew on-board the ISS, but after that, the experiment is fully controlled by ground personnel. In fact, experiments can only be conducted during the sleeping times of the ISS crew, to minimize any disturbances. When observing and performing experiments from ground the terms "loss of signal" (LOS) and "acquisition of signal" (AOS) are a constant companion. The ISS communicates with the ground by a network of ground stations and geostationary satellites. There are certain periods of time, where the line of sight is impeded. LOS is the time during which no communication between ground and space station is possible. This happens when the space station enters the Earth's shadow from the perspective of the geostationary satellite, or structures of the space station come in-between the antenna of the space station and the satellite. AOS is the time when communication between station and ground is possible [36]. LOS and AOS can be pre-planned and the experiment is conducted in a way, that LOS does not hinder it. Video communication is transmitted over the K_U-band, voice and data over the S-band. For the experiment to be successfully conducted, it is important to have both bands in AOS.

Testing routine

As mentioned above, the ELF apparatus is controlled remotely from the ground station in Japan. At the beginning of a testing day, the atmosphere inside the experimental chamber needs to be exchanged. This process includes opening a hatch to space to pump out the ambient atmosphere inside the chamber, closing the hatch, and filling the chamber with protective gas, or air. Testing of refractive metal samples is accomplished by processing in a protective shielding gas (0.172 MPa) to limit oxidation while noble metals

[6] With super-alloys the sample charge changes.

are processed in air (0.2 MPa) to limit evaporation. The sample, which is processed, is then selected from the sample carousel and needs to be statically charged by catching it with one of the push rods. After charging the sample, it is levitated and ready for the first heating process, referred to as "baking". Here, the sample is heated up close to the melting temperature but not melted to ensure no water vapour or other residual contamination remains on the sample's surface. When processing super-alloys the sample tends to change its polarity. A negatively charged sample suddenly gets positively charged. This so-called "sample inversion" has in the past caused many problems and lead to losing samples. Improvements to the apparatus made it possible to deal with such inversions. After baking is completed, the sample is cooled down again and recharged with one of the pushing rods. After levitating it again, the sample is ready to be melted and submitted to exciting oscillations. Typically, a so-called "oscillation sweep" is performed, exciting the sample with varying frequencies and recording the response. After the measurement the sample is cooled down and retrieved.

3. NIST Standard Reference Material 1155a

3.1. Motivation

As mentioned in Chapter 1, experimentally obtained data are of great value for simulations and modelling. The measurement of NIST SRM 1155a, an AISI 316 L stainless steel is a good example. The material is a standard reference material, designed by NIST, with a very well defined chemical composition. It was designed to calibrate and develop methods to analyse material compositions. As the material a) has a very well defined composition, and b) is available at NIST in large quantities, it is used by a working group of NIST in Boulder, CO, to perform laser welding experiments (see, e.g. [37]). For an industrial use of laser welding, or additive manufacturing, initial parameters, crucial to the outcome of the product, need to be known beforehand. A company cannot rely on time and cost intensive trial-and-error approaches to find these parameters. Therefore, NIST decided to group up with other national and international institutions to work together on the material (see fig. 3.1).

Experimental data are determined and simulations and models are developed. The Thermo- and Metalphysics group in Graz was contacted by NIST and asked to provide thermophysical data. As part of this work, the material was characterized by means of ohmic pulse-heating, dynamic scanning calorimetry and electromagnetic levitation. While there are experimentally obtained thermophysical data available for many AISI 316 L steels (see e.g. [38–40]), the composition varies between these steels. In our publication [41], we argued that the variation in data of just one thermophysical property (thermal diffusivity), owing to different compositions, results in large

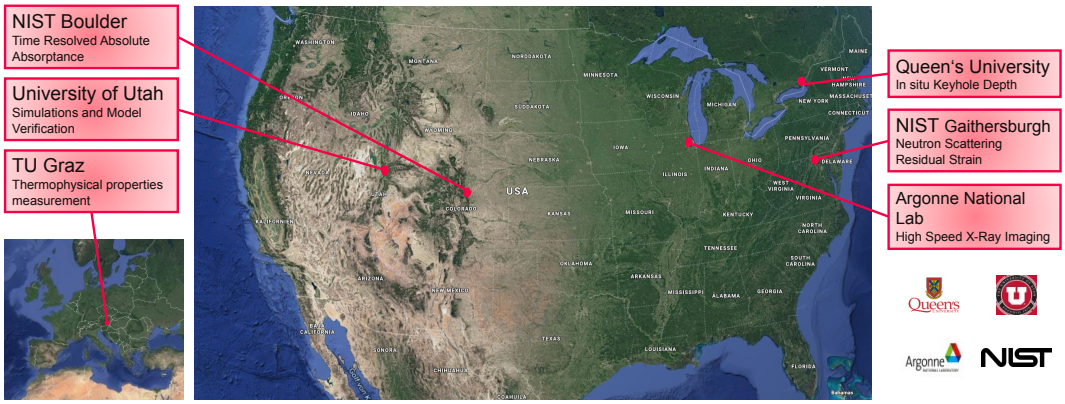

Figure 3.1.: Institutes working on the NIST SRM 1155a. Simulation and experimental work.

uncertainty of the thermal gradient, which is crucial for development of many metallurgical phenomena. Therefore, when developing models and simulations it is important to use data, obtained experimentally, not on similar steels, but on the exact same steel.

Table 3.1.: Obtained thermophysical properties and methods used for their determination. H_s ... Specific enthalpy, ρ_{IG} ... Uncorrected electrical resistivity, ρ ... Corrected electrical resistivity, D ... Density, $\frac{V(T)}{V_0}$ ... Thermal expansion, c_p ... Specific heat capacity, γ ... Surface tension.

Property	Unit	Temperature range	Method
H_s	$kJ \cdot kg^{-1}$	$500 < T \,/\, K < 2800$	OPA + DSC
ρ_{IG}	$\mu\Omega \cdot m$	$500 < T \,/\, K < 2800$	OPA + DSC
ρ	$\mu\Omega \cdot m$	$500 < T \,/\, K < 2800$	OPA + DSC
D	$kg \cdot m^{-3}$	$500 < T \,/\, K < 2800$	OPA
$\frac{V(T)}{V_0}$	1	$500 < T \,/\, K < 2800$	OPA
c_p	$kJ \cdot kg^{-1}K^{-1}$	$473 < T \,/\, K < 1253$	DSC
γ	$mN \cdot m^{-1}$	$1680 < T \,/\, K < 1880$	EML

3.2. Experimental Details and Results

Tab. 3.1 lists all obtained thermophysical properties and the methods used to determine them. Details about measurements and data evaluation can be found in chapter 2. In this chapter experimental details, specific to the characterisation of the NIST SRM 1155a and details about the material, are explained. As mentioned before, the material is classified as an AISI 316 L stainless steel. The exact chemical composition can be found in tab. 3.2.

3.2.1. Material Composition and Determination of Melting Temperatures

Table 3.2.: Certified mass fraction values for SRM 1155a. *Oxygen content was estimated from one or more NIST or collaborator test methods. [42]

Element	Mass Fraction / %	Coverage Factor, k
Carbon (C)	0.0260 ± 0.0036	2.45
Cobalt (Co)	0.225 ± 0.018	2.26
Chromium (Cr)	17.803 ± 0.099	2.20
Copper (Cu)	0.2431 ± 0.0050	2.20
Iron (Fe)	64.71 ± 0.12	2.00
Manganese (Mn)	1.593 ± 0.060	2.06
Molybdenum (Mo)	2.188 ± 0.015	2.18
Niobium (Nb)	0.0082 ± 0.0014	3.18
Nickel (Ni)	12.471 ± 0.056	2.20
Phosphorus (P)	0.0271 ± 0.0012	2.11
Silicon (Si)	0.521 ± 0.017	2.03
Titanium (Ti)	0.0039 ± 0.0012	2.45
Vanadium (V)	0.0725 ± 0.0046	2.23
Tungsten (W)	0.0809 ± 0.0059	2.45
Oxygen (O)*	0.003	

To determine the solidus and liquidus temperature, a combination of OPA and DSC measurements were performed. Under normal circumstances,

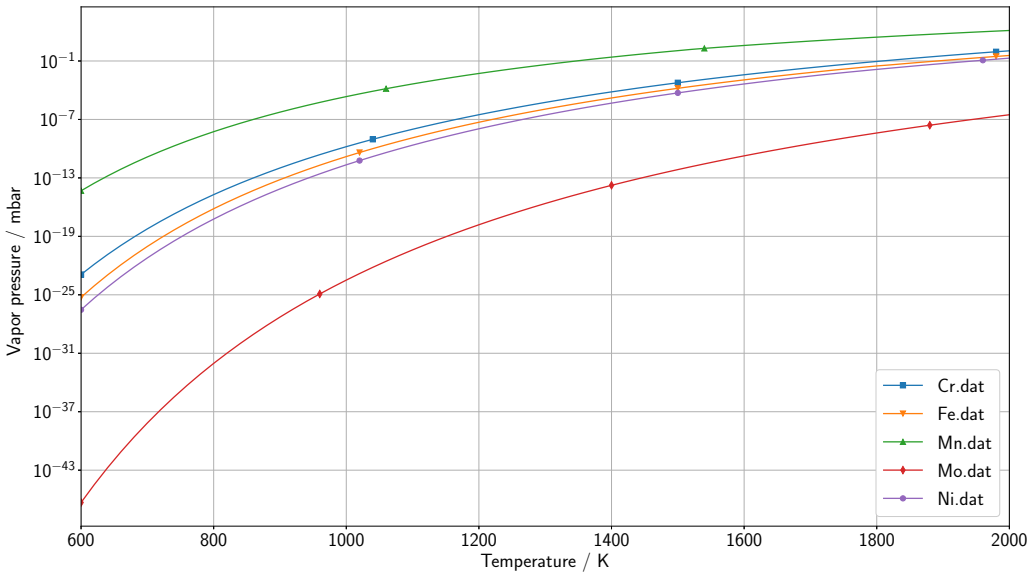

Figure 3.2.: Vapor pressures of the elements with the highest mass fraction values for NIST SRM 1155a. Vapor pressure data from the TU Wien VaporPressure Calculator [44].

these temperatures can be determined by performing solely DSC or DTA. However, as the material contains roughly 1.6 % manganese (see tab. 3.2), which has a very high vapour pressure and tends to evaporate easily, a different approach has to be taken into consideration. The solidus temperature with DSC or DTA measurements is performed by heating up a small piece of the specimen to a temperature above the presumed melting point. When melting starts, energy is needed to break the bonds in the material and the sample's temperature will not rise. This is called latent heat. Therefore, the temperature difference between the sample crucible and reference crucible in the DSC will increase significantly and the DSC signal will rise. The onset of this rise in the DSC signal is the solidus temperature, or for a pure metal, the melting temperature. For a thorough guide to determining melting points with DCS/DTA measurements the reader is referred to the work of Barrall [43]. When heating NIST SRM 1155a to 1500 K multiple times, more and more manganese evaporates from the sample, leading to a rising in the onset value for each heating cycle. Figure 3.2 shows the vapor pressures of

the elements with the highest mass fractions in the composition of the SRM. The vapour pressure of manganese is orders of magnitude larger than that of other components and leads to significant loss of Mn during heating.

A different approach to determine the solidus temperature is to combine DSC measurements with OPA measurements. Specific heat capacity c_p is easily accessible via DSC. Integrating c_p with respect to temperature yields specific enthalpy:

$$H(T) = \int_{473\,\mathrm{K}}^{T} c_p(T')\mathrm{d}T' + (473\,\mathrm{K} - 298\,\mathrm{K}) \cdot c_p(473\,\mathrm{K}). \tag{3.1}$$

Equation (3.1) is easily explained: DSC temperature range starts at 473 K, while OPA enthalpy measurements start from room temperature (298 K). To compare both (equal) enthalpies, the missing enthalpy part in the DSC measurements has to be added. It is assumed that c_p is constant from 473 K to room temperature, which is reflected in the second part of eq. (3.1). Once enthalpy as a function of temperature ($H(T)$) is found, temperature as a function of enthalpy ($T(H)$) is obtainable as well. As mentioned before, specific enthalpy is accessible via OPA measurements from room temperature. The problem with OPA is that temperature is not available under a certain threshold, due to the sensitivity of the photo diode of the pyrometer (see tab. 2.1). It is however possible to match enthalpy values obtained by OPA measurements with those obtained via DSC. As the specific enthalpy at a certain temperature is the same, regardless the method used to obtain it, enthalpy matching provides a possibility to expand the temperature range to lower temperatures for OPA measurements. Not only is this very useful when extending the temperature range for quantities measured with OPA, it also provides a method to determine melting temperatures. Plotting temperature data from DSC measurements as a function of enthalpy and comparing it with the pyrometer signal as a function of enthalpy allows to read the onset temperature of the melting. Figure 3.3 (a) shows data from DSC measurements: The small red squares are directly measured specific heat data, which have been integrated to obtain enthalpy. The solid light blue line is a quadratic fit to the measured data, extrapolated to the enthalpy value of the onset melting, indicated by the dark blue dashed line. Figure 3.3 (b) shows pyrometer data as a function of OPA-obtained enthalpy, represented by the red dots. The solid phase and the melting plateau have been

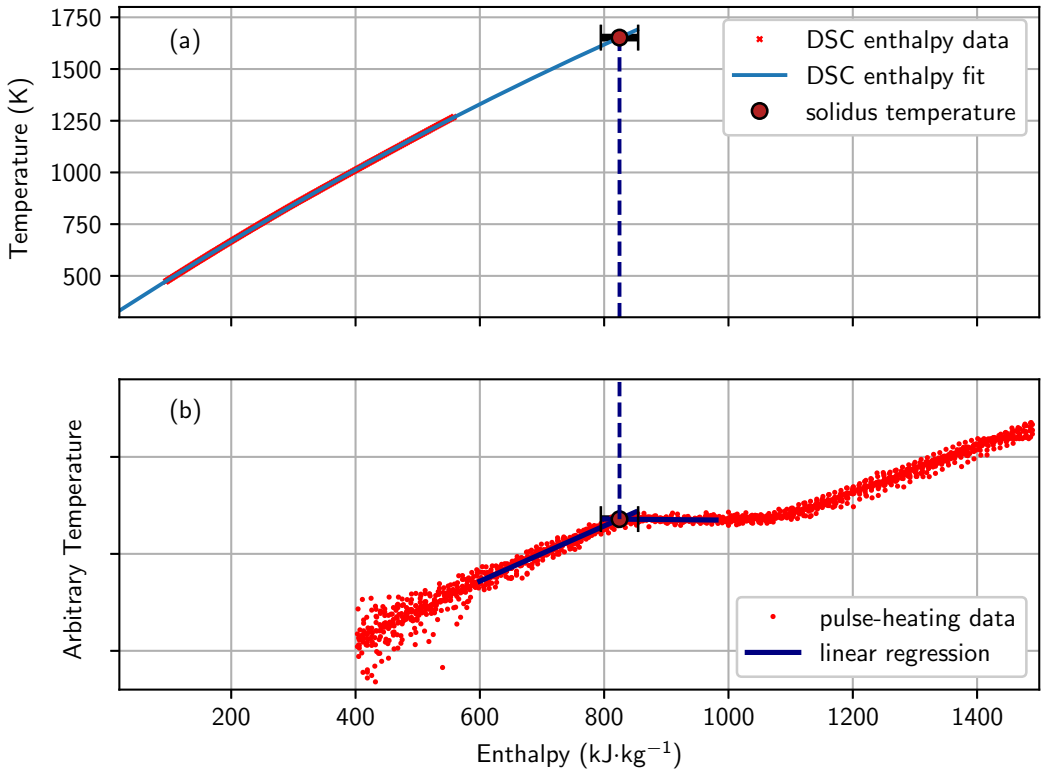

Figure 3.3.: Enthalpy matching to obtain the solidus temperature of NIST SRM 1155a. Published in [41].

Table 3.3.: Solidus and liquidus temperature of SRM 1155a. T is the temperature and ΔT is the temperature uncertainty ($k = 2$). Published in [41].

	T / K	ΔT / K
T_s	1675	15
T_l	1708	30

linearly fitted, represented by the dark blue solid lines. The intersection of the two linear fits yield the onset of the melting plateau. The filled red circle corresponds to the solidus temperature. Thanks to the very short experimental duration of OPA measurements and the high heating rates, it is unlikely that evaporation processes take place in OPA measurements. Therefore, melting point temperature determination by enthalpy matching is a useful tool for materials which contain elements that tend to evaporate easily during slow heating processes, like DSC or EML.

Obtaining liquidus temperatures via DSC or DTA measurements is not as straight forward as solidus determination. Ferreira et al. [45] reviewed measurement specifications to obtain exact liquidus temperatures. While in theory, the endothermic peak value of a DSC/DTA curve should give the liquidus temperature of a material, great care has to be taken when interpreting DSC curves. It has been shown by Pedersen et al. [46] that different heating rates alter the position of the endothermic peak in the DSC thermogram. To achieve equilibrium conditions, a heating rate of $0\,\mathrm{K}\cdot\mathrm{s}^{-1}$ would be needed. Therefore, a multitude of heating rates have to be run on a sample and the endothermic peak as a function of heating rate has to be plotted and fitted. The fit will then be extrapolated to a heating rate of $0\,\mathrm{K}\cdot\mathrm{s}^{-1}$, yielding the liquidus temperature of the specimen. The melting temperatures and their uncertainties are presented in tab. 3.3. Figure 3.4 shows specific heat capacity measured by means of DSC.

3.2.2. Electrical Data

As mentioned in chapter 2, the mass of the investigated wires, which is needed to obtain many thermophysical properties, is calculated from room

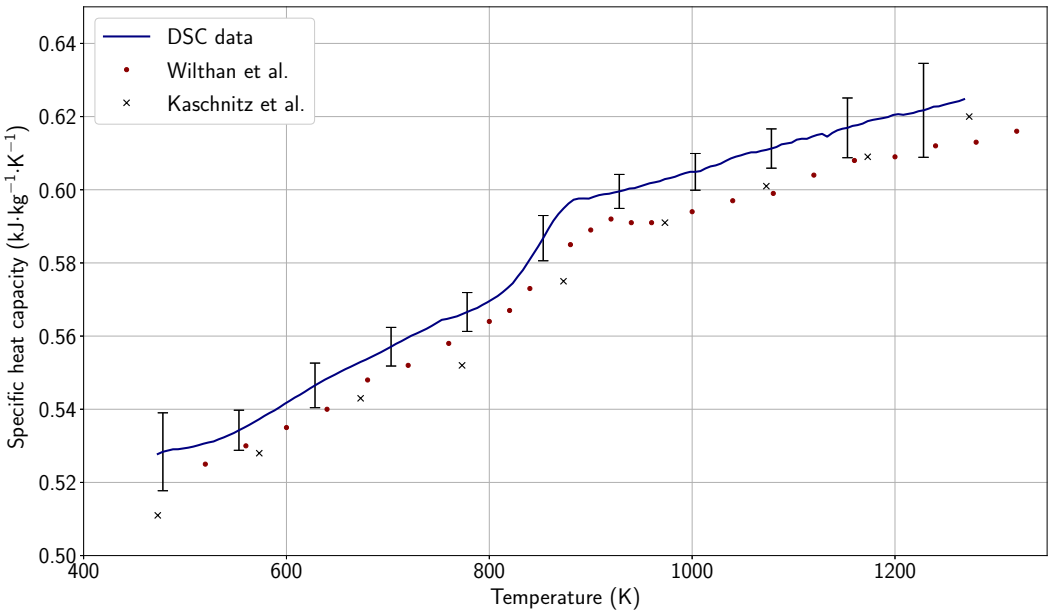

Figure 3.4.: Specific heat capacity determined with DSC measurements for the NIST SRM 1155a. The blue line represents data from this work. The red dots represent data from the literature of a similar steel by Kaschnitz et al. [47]. The black crosses represent data from the literature of a similar steel by Mills et al. [48]. Published in [41].

density. Therefore, room density has to be determined beforehand. Cylinders with a diameter $d = (10.98 \pm 0.01) \times 10^{-3}\,\mathrm{m}$ and a height $h = (5.19 \pm 0.01) \times 10^{-3}\,\mathrm{m}$ (diameter and height have been measured 30 times with a micrometer screw) have been machined and weighed with a Mettler Toledo PB303 balance.

With a measured mass $m = (3.883 \pm 0.001) \times 10^{-3}\,\mathrm{kg}$ the room temperature density was determined to be $D_{\mathrm{RT}} = (7904 \pm 25)\,\mathrm{kg \cdot m^{-3}}$.

Specific Enthalpy in kJ·kg^{-1}

Specific enthalpy was determined by OPA and DSC measurements and compared to data from the literature of similar steels. Figure 3.5 shows specific enthalpy for the NIST SRM 1155a. The temperature range of the OPA measurements, which is limited by the range of the pyrometer, has been extended by DSC measurements. In the temperature range $470 \leq T/\mathrm{K} \leq 1270$ specific enthalpy can be described by the following polynomial

$$H_{\mathrm{S}}(T) = -139 + 0.459 \cdot T + 7.16 \cdot 10^{-5} \cdot T^2, \quad 470 \leq T/\mathrm{K} \leq 1270. \tag{3.2}$$

In the temperature range $1260 \leq T/\mathrm{K} \leq 1675$ specific enthalpy can be described by

$$H_{\mathrm{S}}(T) = -374 + 0.714 \cdot T, \quad 1260 \leq T/\mathrm{K} \leq 1675. \tag{3.3}$$

Finally, in the temperature range $1708 \leq T/\mathrm{K} \leq 2900$ specific enthalpy can be described by

$$H_{\mathrm{S}}(T) = -335 + 0.847 \cdot T, \quad 1708 \leq T/\mathrm{K} \leq 2900. \tag{3.4}$$

Electrical Resistivity in $\mu\Omega$·m

Electrical resistivity was determined by OPA and DSC measurements and compared to data of similar steels from the literature. Resistivity data is

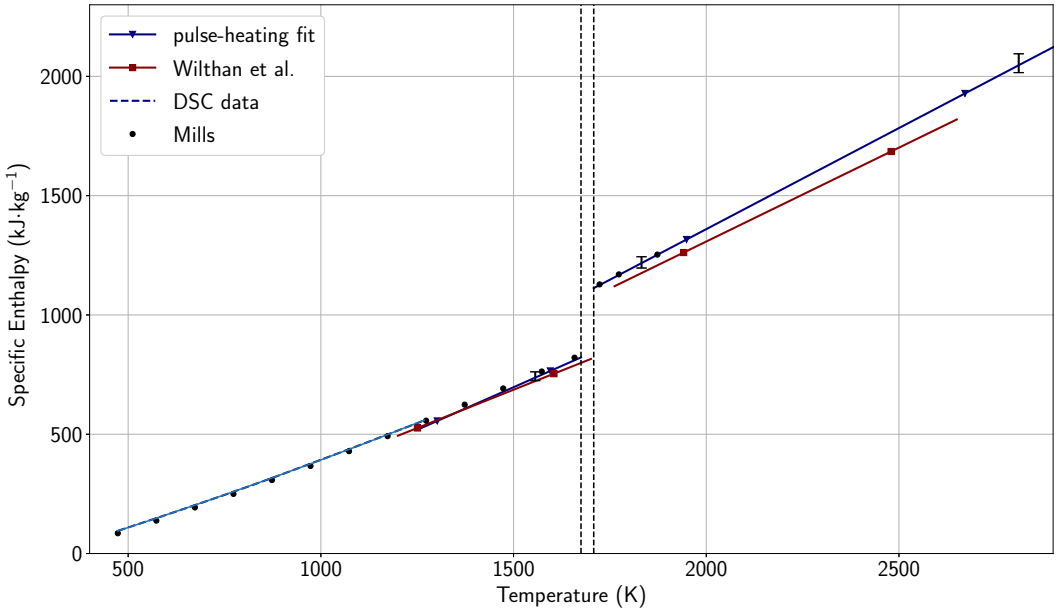

Figure 3.5.: Enthalpy data for NIST SRM 1155a. The solid blue lines represent linear regressions to the experimental data. The solid red lines represent data from the literature of a similar steel by Wilthan et al. [40]. The black circles represent data from the literature of a similar steel by Mills et al. [48]. Published in [41].

given as corrected, meaning the thermal expansion has been taken into account, and as uncorrected, meaning initial geometry is assumed. The reason for presenting both is simply that some models use corrected resistivity, while others need uncorrected resistivity as input. Figure 3.6 shows electrical resistivity for the NIST SRM 1155a. The temperature range of the OPA measurements, which is limited by the range of the pyrometer, has been extended by DSC measurements. In the temperature range $470 \leq T/\mathrm{K} \leq 1270$ electrical resistivity, corrected for thermal expansion can be described by the following polynomial

$$\rho_{\mathrm{corr}}(T) = 0.598 + 8.723 \cdot 10^{-4} \cdot T - 2.466 \cdot 10^{-7} \cdot T^2, \quad 470 \leq T/\mathrm{K} \leq 1270. \tag{3.5}$$

In the temperature range $1260 \leq T/\mathrm{K} \leq 1675$ electrical resistivity, corrected for thermal expansion can be described by the following polynomial

$$\rho_{\mathrm{corr}}(T) = 0.977 + 2.605 \cdot 10^{-4} \cdot T, \quad 1260 \leq T/\mathrm{K} \leq 1675. \tag{3.6}$$

In the temperature range $1708 \leq T/\mathrm{K} \leq 2900$ electrical resistivity, corrected for thermal expansion can be described by the following polynomial

$$\rho_{\mathrm{corr}}(T) = 1.154 + 1.893 \cdot 10^{-4} \cdot T, \quad 1260 \leq T/\mathrm{K} \leq 1675. \tag{3.7}$$

The electrical resistivity, assuming initial geometry $\rho_{\mathrm{IG}}(T)$, as a function of temperature in the temperature range $470 \leq T/\mathrm{K} \leq 1270$ is given by the following polynomial

$$\rho_{\mathrm{IG}}(T) = 0.624 + 7.951 \cdot 10^{-4} \cdot T - 2.613 \cdot 10^{-7} \cdot T^2, \quad 470 \leq T/\mathrm{K} \leq 1270. \tag{3.8}$$

The electrical resistivity, assuming initial geometry $\rho_{\mathrm{IG}}(T)$, as a function of temperature in the temperature range $1260 \leq T/\mathrm{K} \leq 1675$ is given by the following polynomial

$$\rho_{\mathrm{IG}}(T) = 1.026 + 1.477 \cdot 10^{-4} \cdot T, \quad 1260 \leq T/\mathrm{K} \leq 1675. \tag{3.9}$$

The electrical resistivity, assuming initial geometry $\rho_{\mathrm{IG}}(T)$, as a function of temperature in the temperature range $1708 \leq T/\mathrm{K} \leq 2900$ is given by the following polynomial

$$\rho_{\mathrm{IG}}(T) = 1.263 + 2.021 \cdot 10^{-5} \cdot T, \quad 1708 \leq T/\mathrm{K} \leq 2900. \tag{3.10}$$

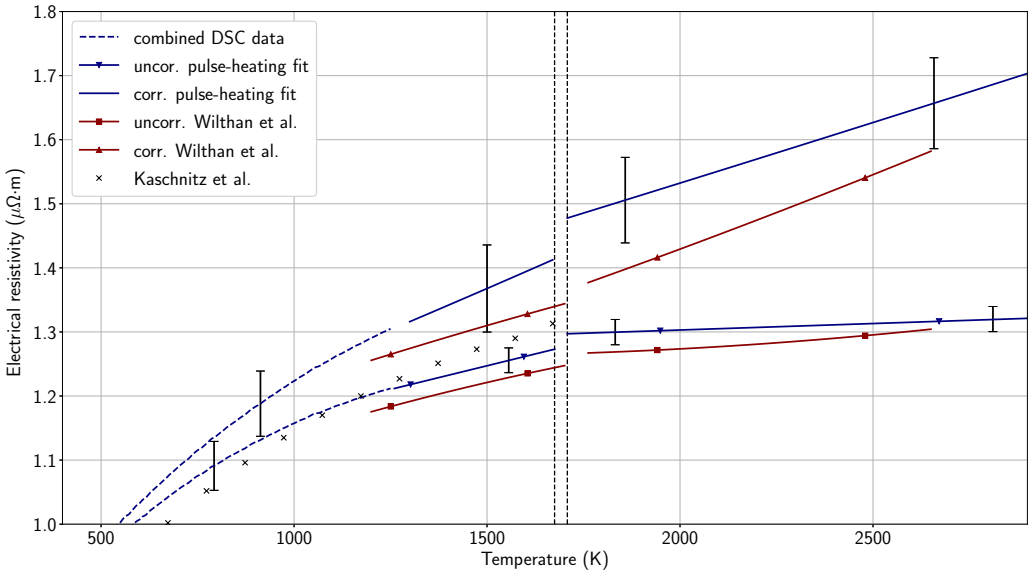

Figure 3.6.: Electrical resistivity data for NIST SRM 1155a. The solid blue lines represent linear regressions to the experimental data. The solid red lines represent data from the literature of a similar steel by Wilthan et al. [40]. The black crosses represent data from the literature of a similar steel by Kaschnitz et al. [47]. Published in [41].

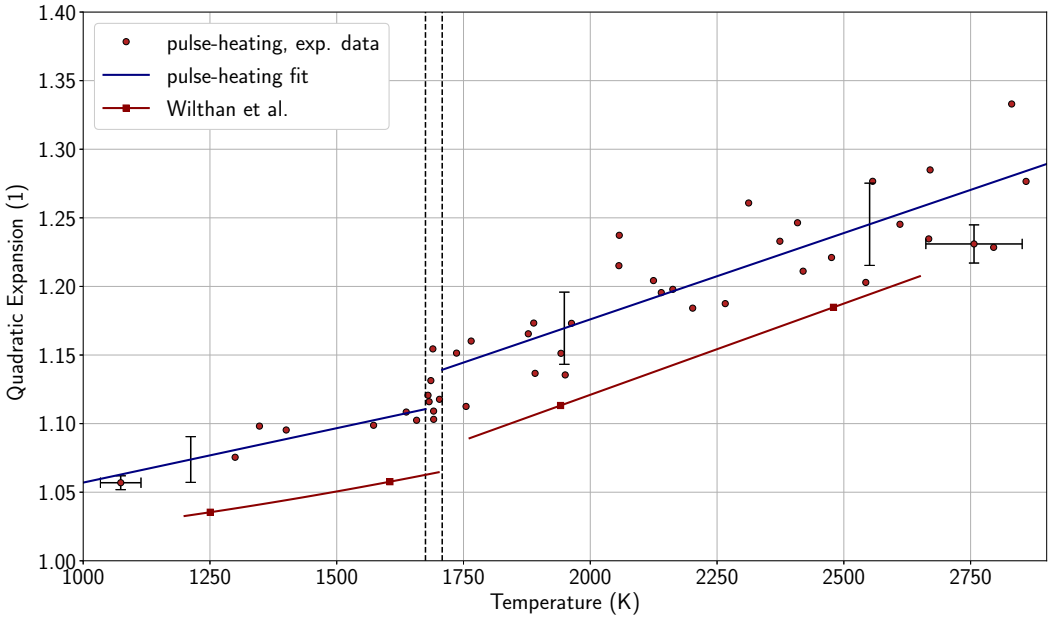

Figure 3.7.: Thermal radial expansion as a function of temperature for the NIST SRM 1155a. The red circles represent the measured experimental data. The solid blue line represents linear regressions to the data. The solid red line represents data from the literature by Wilthan et al. [40].

3.2.3. Expansion Data

In this section, thermal expansion and density as a function of temperature for the SRM is presented.

Thermal Expansion

Figure 3.7 shows thermal expansion data for NIST SRM 1155a. The red circles represent the measured experimental data. The solid blue line represents linear regressions to the data. The solid red line represents data from the literature by Wilthan et al. [40]. Thermal radial expansion is shown in fig. 3.7. The data were fitted linearly in the temperature range $500 \leq T/\mathrm{K} \leq 1675$

in the solid phase by

$$\left(\frac{d(t)}{d_0}\right)_s^2 = 9.777 \cdot 10^{-1} + 7.933 \cdot 10^{-5} \cdot T, \quad 500 \leq T/\mathrm{K} \leq 1675. \tag{3.11}$$

In the liquid phase, expansion data have been fitted in the temperature range $1708 \leq T/\mathrm{K} \leq 2900$ linearly by

$$\left(\frac{d(T)}{d_0}\right)_l^2 = 9.243 \cdot 10^{-1} + 1.258 \cdot 10^{-4} \cdot T, \quad 1708 \leq T/\mathrm{K} \leq 2900. \tag{3.12}$$

Density in $\mathrm{kg \cdot m^{-3}}$

Density as a function of temperature is presented in fig. 3.8. The red circles represent the measured experimental data. The solid blue line represents linear regressions to the data. The solid red line represents data from the literature by Wilthan et al. [40]. The solid green line represents data from the literature by Fukuyama et al. [39]. Density data in the solid phase have been fitted linearly in the temperature range $500 \leq T/\mathrm{K} \leq 1675$ by

$$D_s(T) = 8.0512 \cdot 10^3 - 5.638 \cdot 10^{-1} \cdot T, \quad 500 \leq T/\mathrm{K} \leq 1675. \tag{3.13}$$

In the liquid phase, density data have been fitted linearly in the temperature range $1708 \leq T/\mathrm{K} \leq 2900$ by

$$D_l(T) = 8.0464 \cdot 10^3 - 6.607 \cdot 10^{-1} \cdot T, \quad 1708 \leq T/\mathrm{K} \leq 2900. \tag{3.14}$$

3.2.4. Thermal Conductivity and Thermal Diffusivity

Thermal Diffusivity in $\mathrm{m^2 \cdot s^{-1}}$

Thermal diffusivity data are presented in fig. 3.9 Additionally to OPA and DSC measurements, laser-flash measurements have been performed at the Österreichische Gießerei-Institut in Leoben, Austria. In the solid phase,

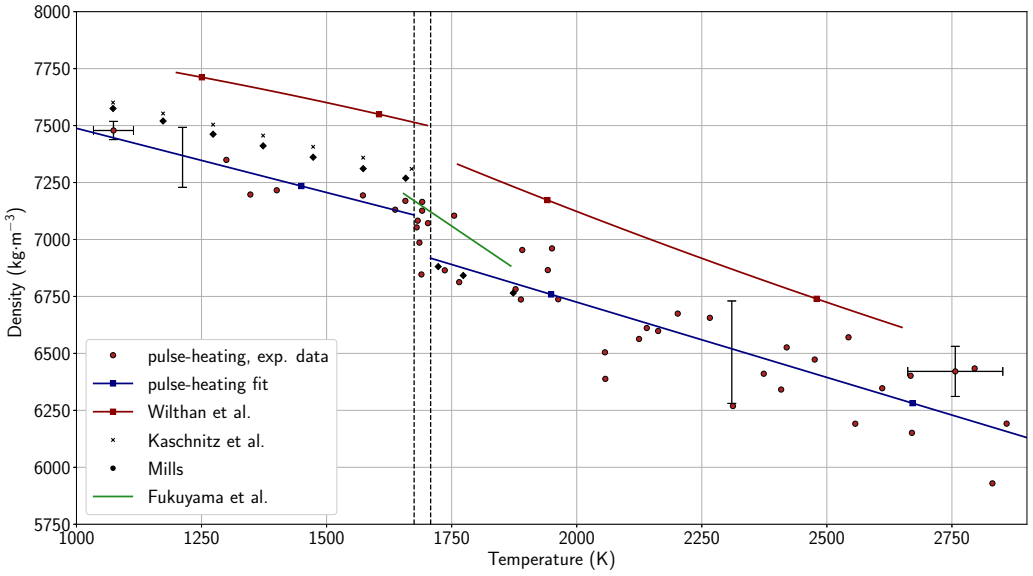

Figure 3.8.: Density as a function of temperature for the NIST SRM 1155a. The red circles represent the measured experimental data. The solid blue line represents linear regressions to the data. The solid red line represents data from the literature by Wilthan et al. [40]. The solid green line represents data from the literature by Fukuyama et al. [39]. The black diamonds represent literature values by Mills et al. [48]. The black crosses represent literature data by Kaschnitz et al. [47]. Published in [41].

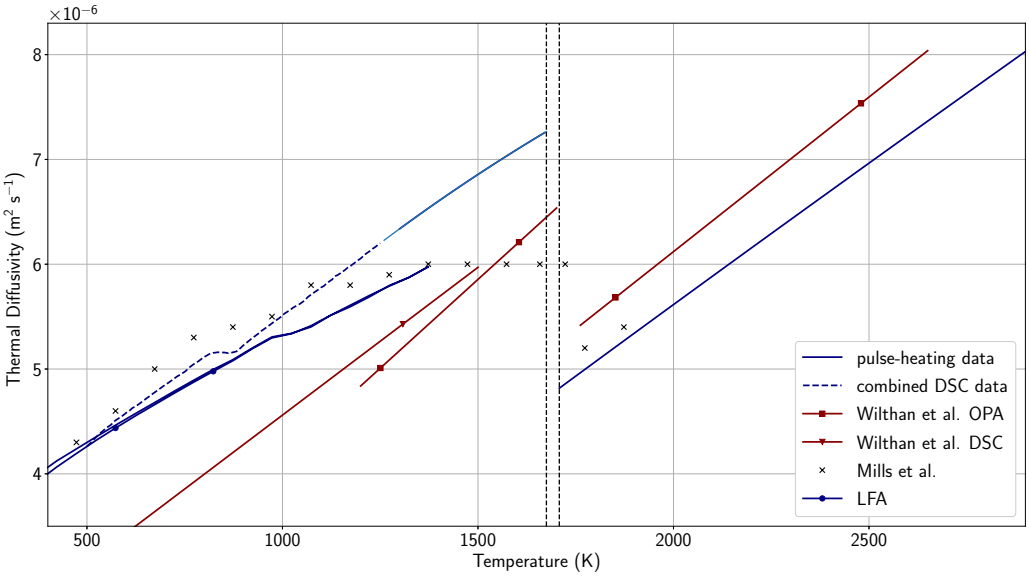

Figure 3.9.: Thermal diffusivity data for the SRM 1155a. The solid blue line represents data from OPA experiments. The dashed blue line represents data from combined measurements of DSC and OPA. The red lines represent data from the literature by Wilthan et al. [40]. The black crosses represent data from the literature by Mills et al. [48]. The solid blue line with squares represent laser flash measurements, performed at the Österreichische Gießerei-Institut.

thermal diffusivity has been fitted quadratically in the temperature range $1260 \leq T/\mathrm{K} \leq 1675$ by

$$a_\mathrm{s}(T) = 1.667 \cdot 10^{-6} + 4.465 \cdot 10^{-9} \cdot T - 6.701 \cdot 10^{-13} \cdot T^2, \quad 1260 \leq T/\mathrm{K} \leq 1675. \tag{3.15}$$

In the liquid phase, thermal diffusivity has been fitted linearly in the temperature range $1708 \leq T/\mathrm{K} \leq 2900$ by

$$a_\mathrm{l}(T) = 2.695 \cdot 10^{-9} + 2.234 \cdot 10^{-9} \cdot T, \; 1708 \leq T/\mathrm{K} \leq 2900. \tag{3.16}$$

Thermal Conductivity in $\mathrm{W \cdot K^{-1}}$

Thermal conductivity from combined DSC and OPA measurements has been fitted in the solid phase in a temperature range $500 \leq T/\mathrm{K} \leq 1250$ by

$$\lambda_\mathrm{s}(T) = 9.382 + 1.722 \cdot 10^{-2} \cdot T - 1.653 \cdot 10^{-6} \cdot T^2, \quad 500 \leq T/\mathrm{K} \leq 1250. \tag{3.17}$$

Thermal conductivity from OPA measurements in the solid phase has been fitted in a temperature range $1300 \leq T/\mathrm{K} \leq 1675$ by

$$\lambda_\mathrm{s}(T) = 6.525 + 2.086 \cdot 10^{-2} \cdot T - 2.689 \cdot 10^{-6} \cdot T^2, \quad 1300 \leq T/\mathrm{K} \leq 1675. \tag{3.18}$$

In the liquid phase, thermal conductivity has been fitted in a temperature range $1708 \leq T/\mathrm{K} \leq 2900$

$$\lambda_\mathrm{l}(T) = 2.27 + 1.764 \cdot 10^{-2} \cdot T - 1.394 \cdot 10^{-6} \cdot T^2, \quad 1300 \leq T/\mathrm{K} \leq 1675. \tag{3.19}$$

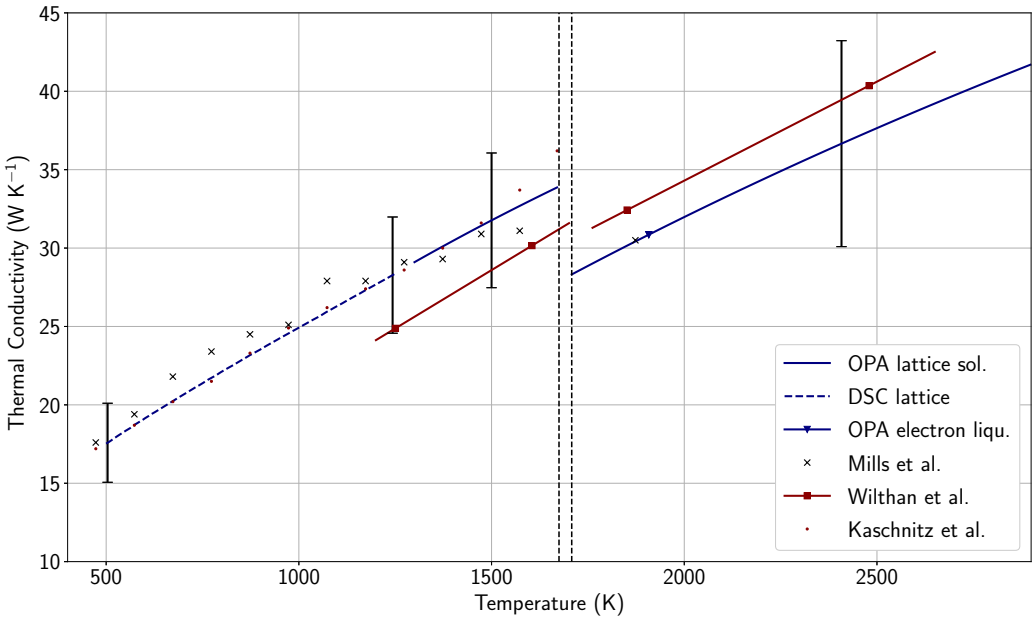

Figure 3.10.: Thermal diffusivity data for the SRM 1155a. The solid blue line represents data from OPA experiments. The dashed blue line represents data from combined measurements of DSC and OPA. The red lines represent data from the literature by Wilthan et al. [40]. The black crosses represent data from the literature by Mills et al. [48]. The red dots represent data from the literature by Kaschnitz et al. [47].

3.2.5. Surface Tension in mN·m^{-1}

Results for surface tension for the NIST SRM 1155a are presented in this section. Measurements were performed with EML in combination with the oscillating drop method. Table 3.2 shows the composition of the SRM. The high vapour pressure of Mn leads to significant evaporation when the samples are liquid for too long. Therefore, the samples had to be liquid for a short period of time only. Thomas Leitner devised a measuring routine to deal with strongly evaporating samples. The samples are levitated and heated up until they are liquid and immediately cooled down by a He gas flow, directed at the samples. Then, the gas flow is reduced until the sample is liquid again and a certain temperature is reached. Data are recorded and the sample is cooled down by increasing the He flow again. A second temperature can now be reached, by controlling the gas flow. Once data acquisition is finished, the sample needs to be landed. This way, the time the sample is in its liquid phase is reduced and evaporation is minimized drastically. The drawback of this method is that the amount of samples which need to be prepared and levitated is very high. A total of 15 samples were investigated in order to achieve satisfying results for surface tension. Figure 3.11 shows the results for surface tension of the SRM in comparison with data from the literature. All steels from the literature classify as AISI 316, or AISI 316L, but differ in composition. Especially interesting for surface tension is the sulfur (S) content, as it has a great influence on surface tension, see e.g. [50]. Table 3.4 summarizes and compares S content of the different steels investigated. Figure 3.11 shows a satisfying trend of rising surface tension with decreasing S content. The only exception being the literature values by Brooks and Quested, who state a S content of 50 ppm before the experiment. However, they do not state S content after the experiment. Surface tension as a function of temperature $\gamma(T)$ has been fitted linearly in the temperature range $1680 \leq T/\mathrm{K} \leq 1880$ by

$$\gamma(T) = (1266 \pm 115) + (0.19 \pm 0.07) \cdot T. \tag{3.20}$$

To visualize the problematic of evaporation and the need to rethink the measuring process, fig. 3.12 shows the comparison of results of briefly molten samples to those which have been liquid for a long period of time. The samples that have been levitated and molten for approximately 30

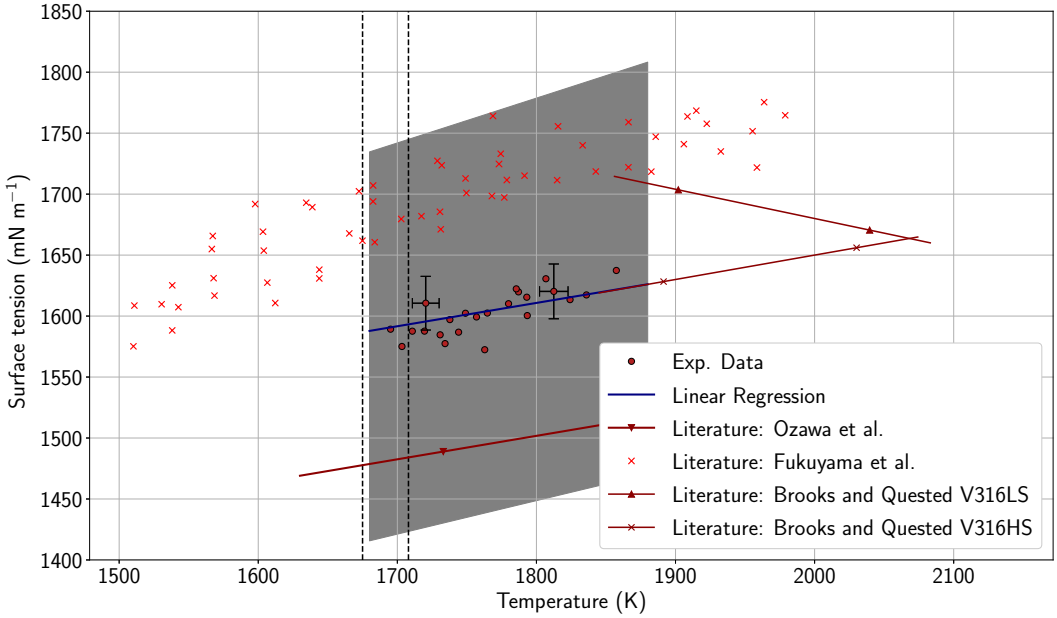

Figure 3.11.: Surface tension of the NIST SRM as a function of temperature. Red circles represent the experimentally measured data of this work. The solid blue line represents a linear regression to the experimentally obtained data. The uncertainty of the fit is represented by the grey area. Red crosses represent surface tension data of an AISI 316 stainless steel by Fukuyama et al. [39]. The solid red line with upwards facing triangles as markers represents surface tension data of an AISI 316 stainless steel by Ozawa et al. [49]. The solid red line with crosses as markers represents surface tension data of an AISI 316 stainless steel with high sulfur content by Brooks and Quested [50]. The solid red line with downwards facing triangles as markers represents surface tension data of an AISI 316 stainless steel with low Sulfur content by Brooks and Quested [50].

Table 3.4.: Sulfur (S) content of AISI 316 steels. If known, the S content in ppm is presented before and after the experiment was conducted.

Reference	S in ppm before	S in ppm after
This work	20	16 to 18
Ozawa et al. [49]	30	6
Fukuyama et al. [39]	12	10
Brooks and Quested LS [50]	10	unknown
Brooks and Quested HS [50]	50	unknown

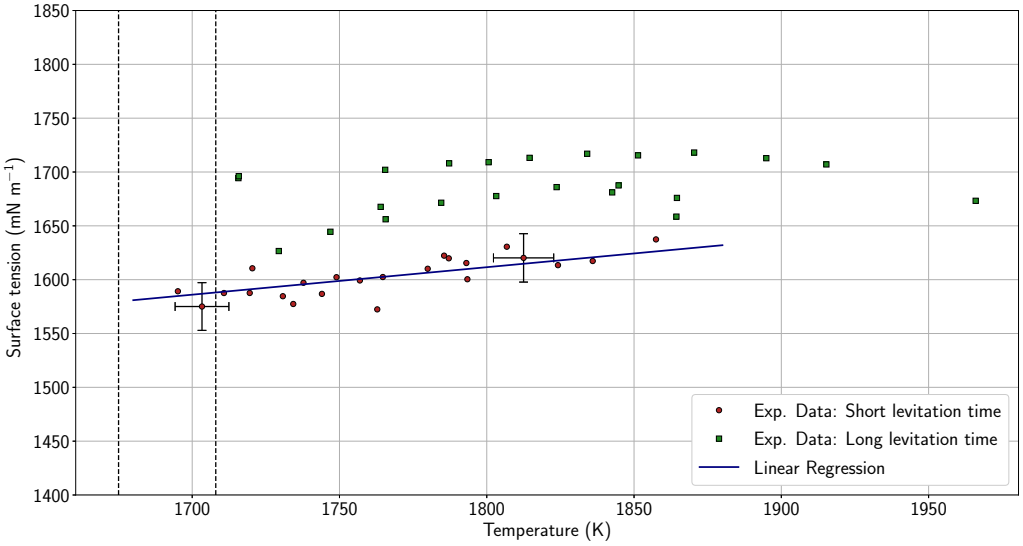

Figure 3.12.: Influence of levitation time. The red circles represent surface tension results of 15 briefly levitated samples. The green squares represent surface tension results of 2 samples, which have been levitated for approximately 30 minutes.

minutes (green squares in fig. 3.12) show a significantly higher surface tension than those that have been levitated for some minutes only (red circles in fig. 3.12). While it was not possible yet to measure S content, Mn content before and after the experiment of the briefly levitated samples and the long levitated samples was determined via energy-dispersive X-ray spectroscopy (EDX). As expected, Mn vanished completely in the long levitated samples but a significant amount of Mn remained in the samples which have been levitated for a short period of time. The results of the EDX analysis are attached in the appendix.

4. Hi-TRACE

4.1. Introduction

Graz University of Technology (TUG) is part of the European Metrology Programme for Innovation and Research (EMPIR) project 17IND11 "Hi-TRACE". The goal of the project is to establish new methods for characterising the thermophysical properties of any solid material up to 3000 °C, and launch a network of reference facilities and materials available to industry [51]. Other partners involved in the project are: Laboratoire national de métrologie et d'essais (LNE, project leader), National Physical Laboratory (NPL), Physikalisch-Technische Bundesanstalt (PTB), Institut Za Nuklearne Nauke Vinca (Vinca), Ariane Group, Commissariat à l'ènergie atomique et aux énergies alternatives (CEA), University of Applied Sciences Würzburg-Schweinfurt (FHWS), Joint Research Centre - European Comission (JRC), Bavarian Center for Applied Energy Research (ZAE Bayern) and Netzsch Gerätebau GmbH (NETZSCH).

While Graz University of Technology will not develop new methods, as stated in the project description, it's contribution to the project has been to provide comparative measurements in order to validate newly developed methods of other institutes. The project is aiming at the solid phase of high-melting metals and alloys up to a temperature of 3000 °C. The experimental methods used at TUG are the ohmic pulse-heating system and the microsecond Division of Amplitude Photo-polarimeter. During this thesis, measurements of specific heat capacity and thermal diffusivity were performed. Normal spectral emissivity measurements were conducted, under the guidance of the author, by Alexander Eber during his master's thesis [18].

4.2. Results

4.2.1. WP1: Thermal Diffusivity

In the following section results for WP1 are presented: Thermal diffusivity a as a function of temperature T are presented. A minimum of three experiments per material were performed and the data from each experiment as well as a fitted polynomial are plotted. To determine thermal diffusivity, the measurement of specific enthalpy $H_S(T)$ in and specific electrical resistivity without considering thermal expansion ρ_{IG} needs to be performed. Data are compared with values from the literature.

Molybdenum

Figure 4.1 depicts specific enthalpy data as a function of temperature. Enthalpy data in $\mathrm{kJ{\cdot}kg^{-1}}$ were linearly fitted by the following polynomial:

$$H_{\mathrm{S}}(T) = -629 + 0.529 \cdot T, \qquad 2260 < T/\mathrm{K} < 2895 \tag{4.1}$$

Figure 4.3 depicts electrical resistivity (assuming initial geometry) data as a function of temperature. Resistivity data in $\mu\Omega{\cdot}\mathrm{m}$ were linearly fitted by the following polynomial:

$$\rho_{\mathrm{IG}}(T) = -0.123 + 3.106 \cdot 10^{-3} \cdot T, \qquad 2260 < T/\mathrm{K} < 2895 \tag{4.2}$$

Thermal diffusivity was then calculated using eq. (2.15) and is presented in fig. 4.5. The reason for the high uncertainty at the beginning of the measurement as opposed to the lower uncertainty at the end of the solid phase derives from the fact that specific heat capacity is a function of temperature in the solid phase, see e.g. [53].

Thermal diffusivity in $\mathrm{m^2{\cdot}s^{-1}}$ for molybdenum was fitted linearly in the temperature range $2260 < T/\mathrm{K} < 2895$ by

$$a(T) = 1.978 \cdot 10^{-5} - 1.074 \cdot 10^{-9} \cdot T, \qquad 2260 < T/\mathrm{K} < 2895 \tag{4.3}$$

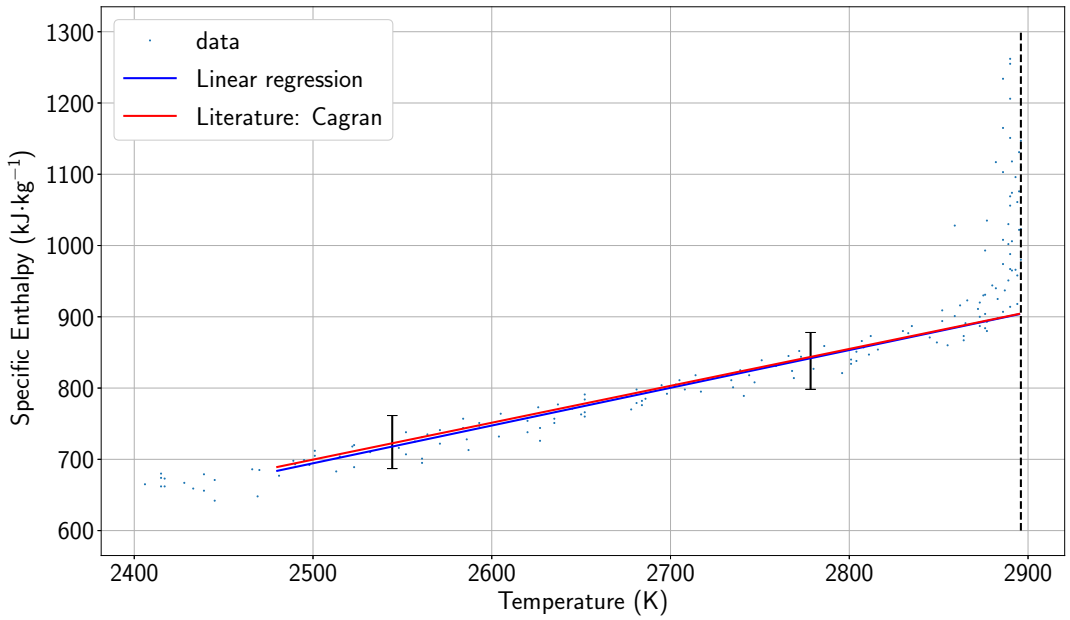

Figure 4.1.: Specific enthalpy H_S as a function of temperature T for molybdenum. The blue dots represent the experimental data, the blue solid line is a linear fit, the red solid line represents data from the literature by Cagran et al. [52]. The melting point is indicated by the dashed black line.

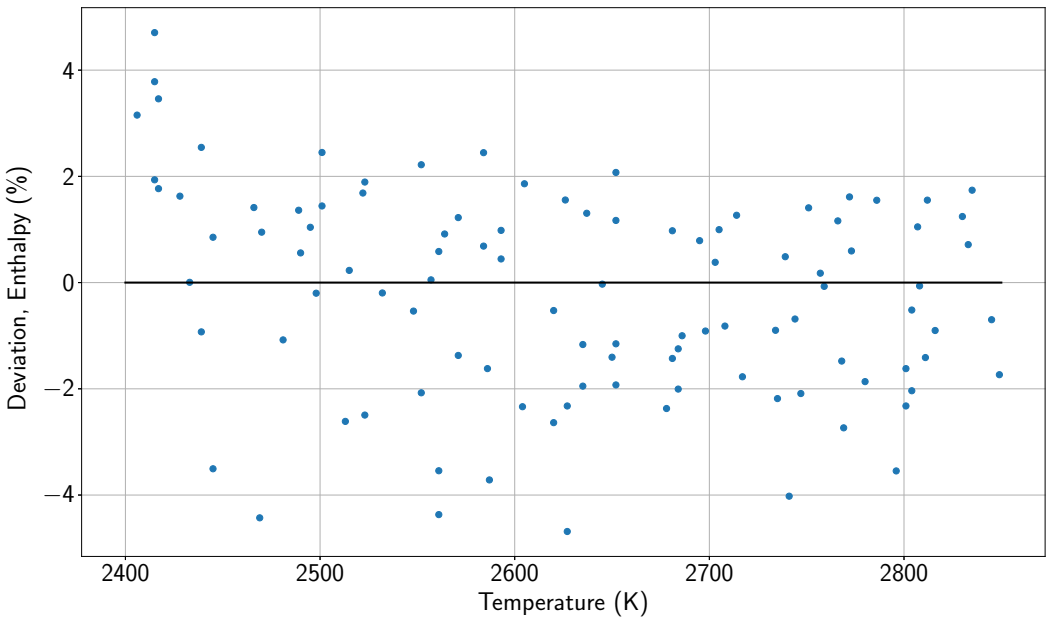

Figure 4.2.: Deviation of the data points from the linear fit in percent for specific enthalpy of molybdenum.

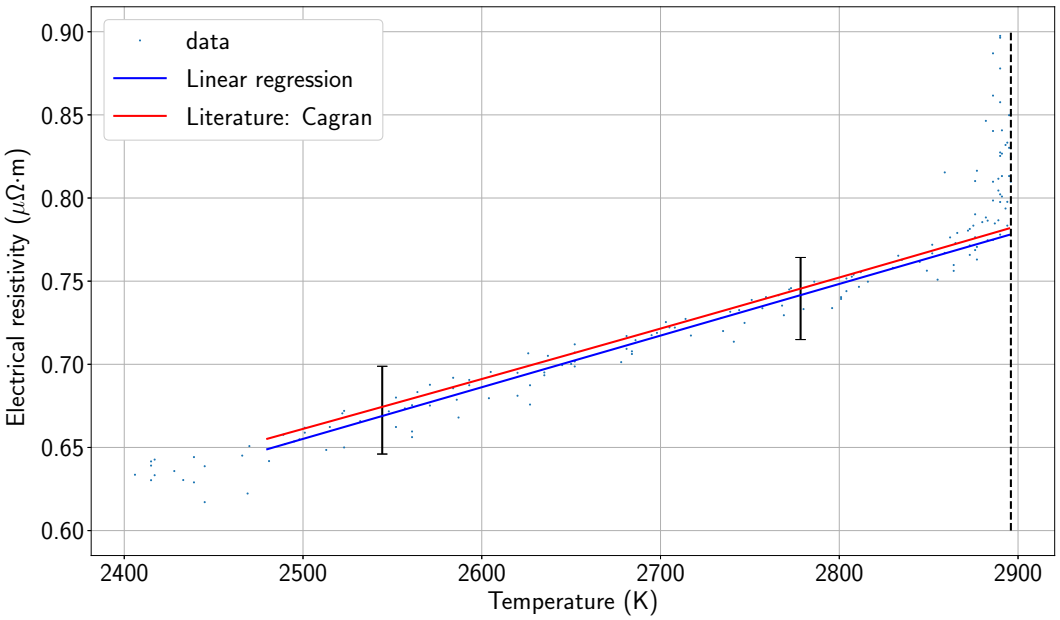

Figure 4.3.: Electrical resistivity ρ_{IG} as a function of temperature T for molybdenum. The blue dots represent the experimental data, the blue solid line is a linear fit, the red solid line represents data from the literature by Cagran et al. [52]. The melting point is indicated by the dashed black line.

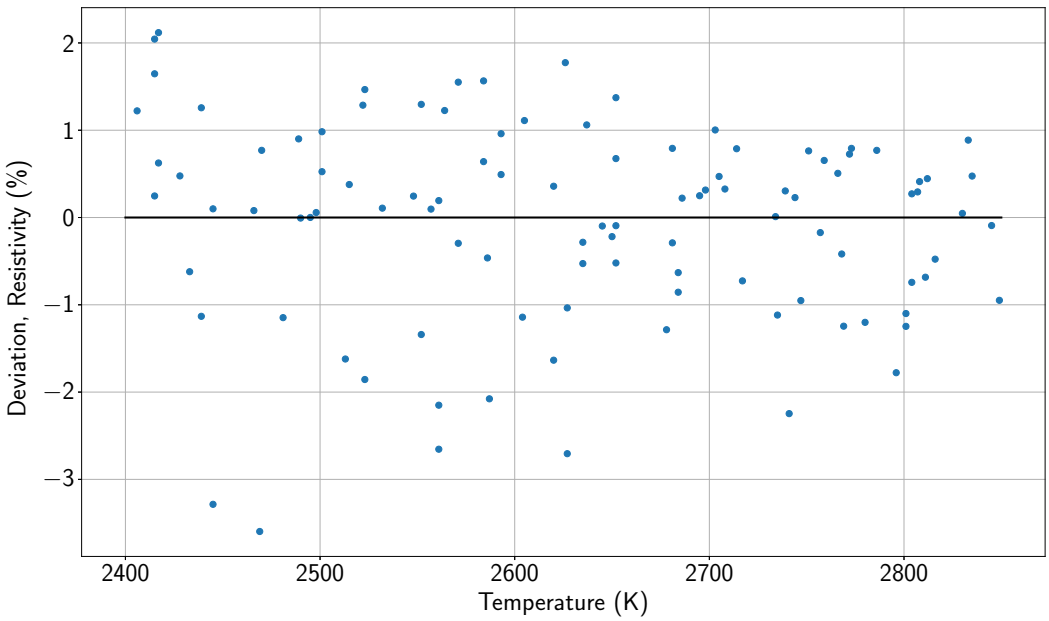

Figure 4.4.: Deviation of the data points from the linear fit in percent for electrical resistivity of molybdenum.

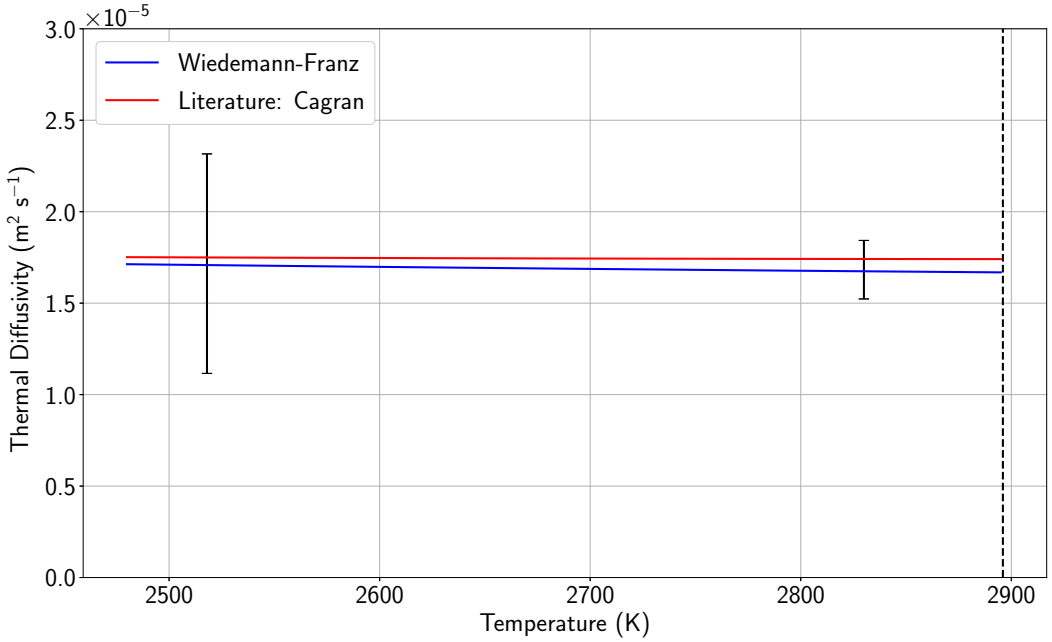

Figure 4.5.: Thermal diffusivity as a function of temperature. The solid blue line represents data from this work, evaluated with the Wiedemann-Franz-law. The red line represents data from the literature by Cagran et al. [52]. The melting point is indicated by the dashed black line.

Tungsten

Figure 4.6 depicts specific enthalpy for tungsten data as a function of temperature. Enthalpy data in $\mathrm{kJ \cdot kg^{-1}}$ were quadratically fitted by the following polynomial:

$$H_S(T) = 126 - 8.345 \cdot 10^{-3} \cdot T + 3.723 \cdot 10^{-5} \cdot T^2, \qquad 2480 < T/\mathrm{K} < 3570. \tag{4.4}$$

Figure 4.8 depicts electrical resistivity (assuming initial geometry) data as a function of temperature for tungsten. Resistivity data in $\mu\Omega \cdot \mathrm{m}$ were linearly fitted by the following polynomial:

$$\rho_{IG}(T) = -8.66 \cdot 10^{-2} + 3.237 \cdot 10^{-4} T, \qquad 2480 < T/\mathrm{K} < 3570. \tag{4.5}$$

Thermal diffusivity was then calculated using eq. (2.15) and is presented in fig. 4.10. Thermal diffusivity in $\mathrm{m^2 \cdot s^{-1}}$ for tungsten was fitted quadratically in the temperature range $2480 < T/\mathrm{K} < 3570$ by

$$a(T) = 6.814 \cdot 10^{-5} - 2.43 \cdot 10^{-8} \cdot T + 2.752 \cdot 10^{-12} \cdot T^2, \qquad 2480 < T/\mathrm{K} < 3570. \tag{4.6}$$

4.2.2. WP2: Specific Heat Capacity

Molybdenum

For specific heat capacity, specific enthalpy needs to be measured. Results for specific enthalpy are given in section 4.2.1. From the slope of specific enthalpy, specific heat capacity at the end of the solid phase can be estimated. For Mo specific enthalpy was estimated to $c_p = (0.53 \pm 0.02)$ kJ $\mathrm{kg^{-1}K^{-1}}$.

Tungsten

In the case of tungsten, specific enthalpy could be fitted quadratically. The derivative with respect to temperature yields an estimation for specific heat

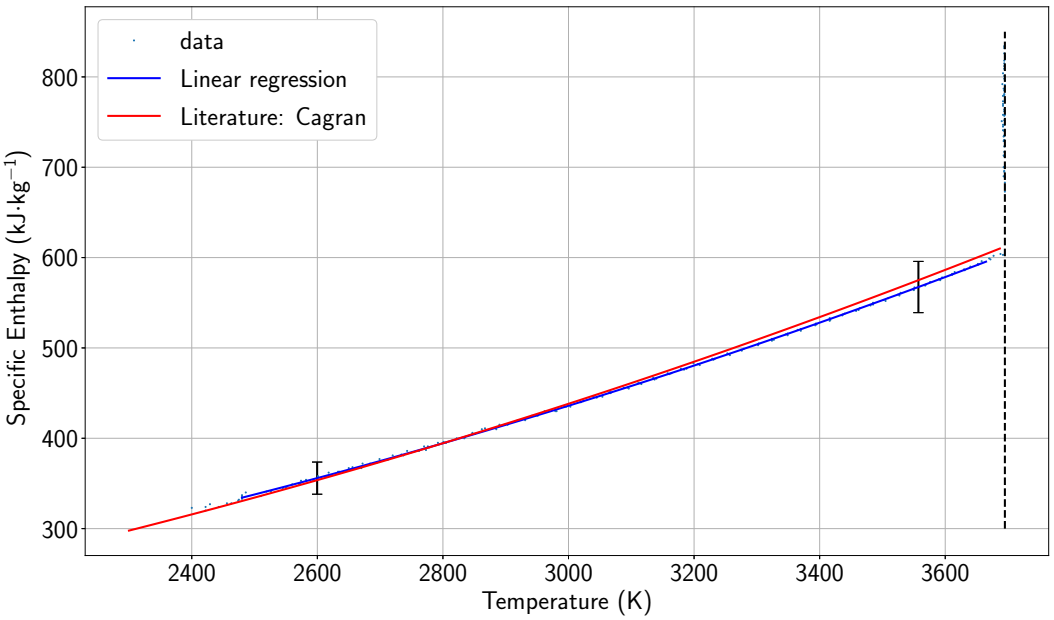

Figure 4.6.: Specific enthalpy H_S as a function of temperature T for tungsten. The blue dots represent the experimental data, the blue solid line is a quadratic fit, the red solid line represents data from the literature by Cagran et al. [52]. The melting point is indicated by the dashed black line.

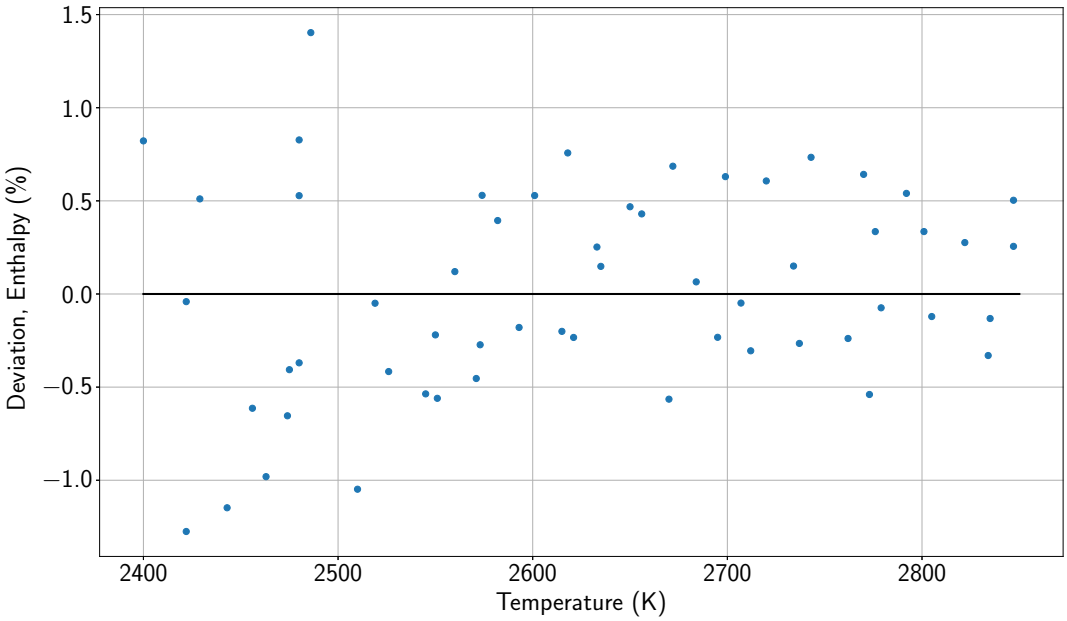

Figure 4.7.: Deviation of the data points from the linear fit in percent for specific enthalpy of tungsten.

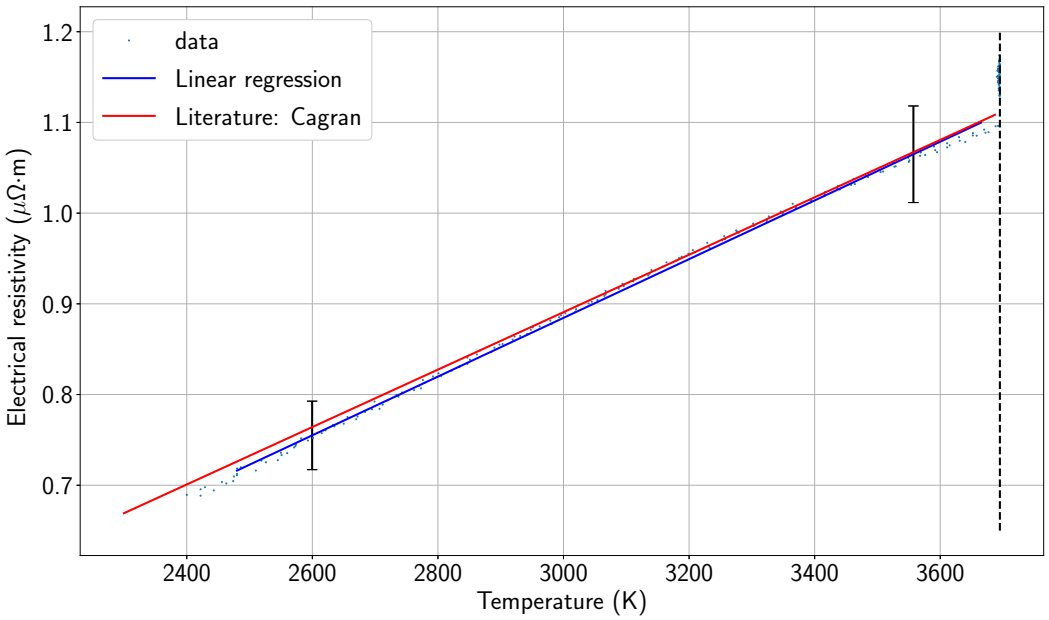

Figure 4.8.: Electrical resistivity ρ_{IG} as a function of temperature T for tungsten. The blue dots represent the experimental data, the blue solid line is a linear fit, the red solid line represents data from the literature by Cagran et al. [52]. The melting point is indicated by the dashed black line.

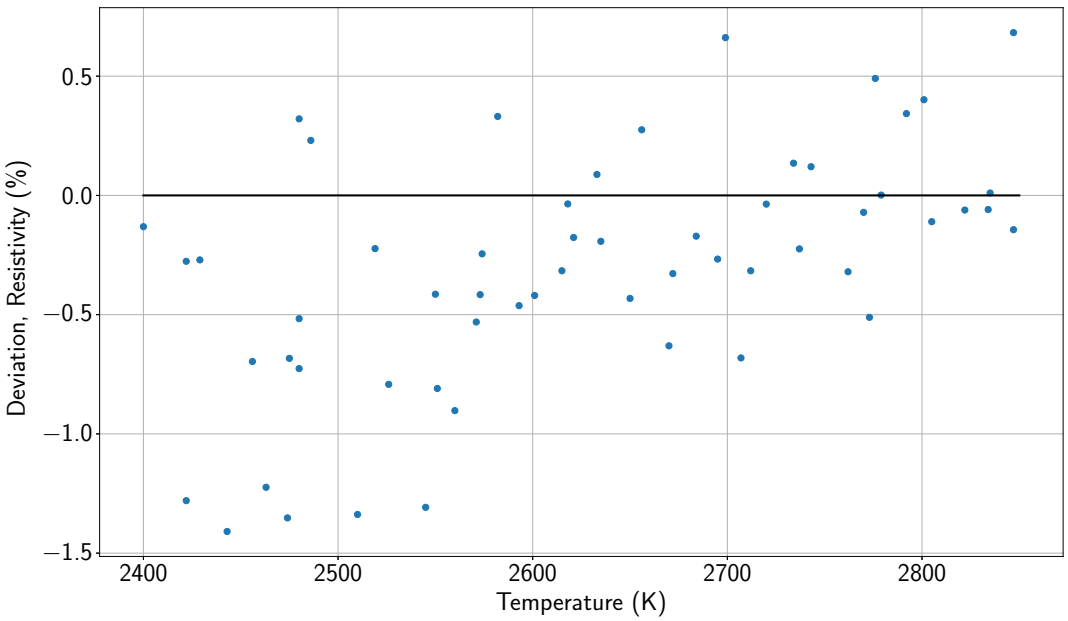

Figure 4.9.: Deviation of the data points from the linear fit in percent for electrical resistivity of tungsten.

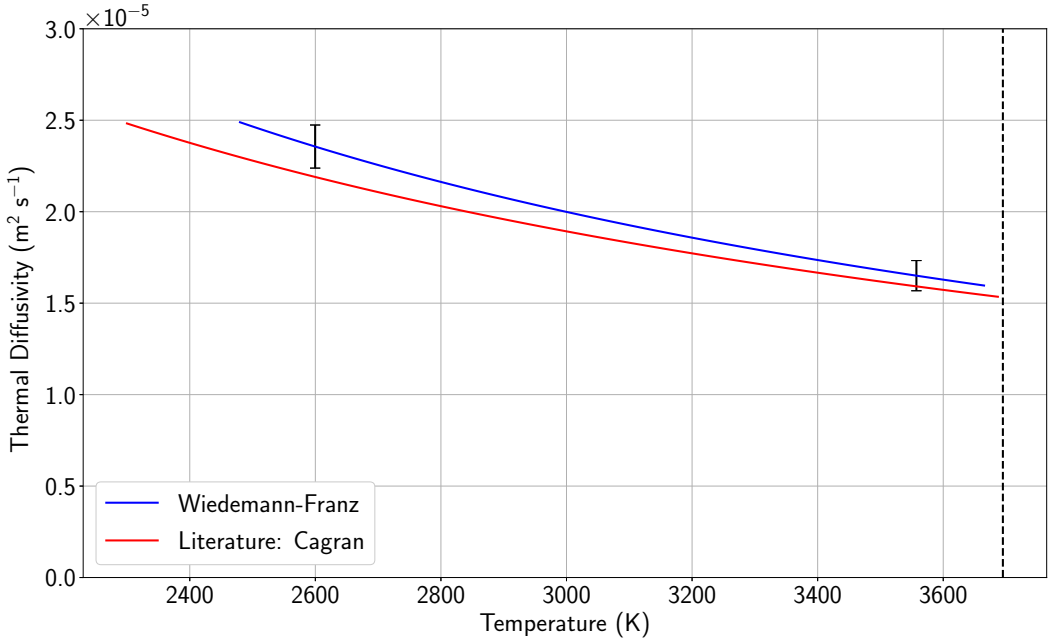

Figure 4.10.: Thermal diffusivity as a function of temperature for tungsten. The solid blue line represents data from this work, evaluated with the Wiedemann-Franz-law. The red line represents data from the literature by Cagran et al. [52]. The melting point is indicated by the dashed black line.

capacity in the temperature range $2480 \leq T/\mathrm{K} \leq 3570$. The linear function for specific heat capacity in $\mathrm{kJ{\cdot}kg^{-1}K^{-1}}$, by deriving eq. (4.4) yields

$$c_\mathrm{p}(T) = -8.345 \cdot 10^{-2} + 7.45 \cdot 10^{-5} \cdot T, \qquad 2480 < T/\mathrm{K} < 3570. \tag{4.7}$$

4.2.3. WP3: Emissivity and Temperature of Fusion

To determine temperature of fusion, an absolute calibration of the pyrometer needs to be performed to obtain the calibration constant K as explained in section 2.1. It was planned to travel to PTB Berlin to calibrate a tungsten strip lamp and conduct the temperature of fusion measurements this way. However, like the rest of the world, also the members of the Hi-TRACE project were heavily impacted by the still on-going pandemic. As a result no calibration could be performed and temperature of fusion could not be determined when this thesis was written.

Molybdenum

Results for molybdenum have been published in [54] as well as in Eber's master's thesis [18]. As the measurement and evaluation of the data were performed under this author's guidance throughout this thesis, they are summarized here as well. Figure 4.11 shows normal spectral emissivity at 684.5 nm for solid and liquid molybdenum as a function of radiance temperature T_r. The red lines represent linear regressions of the data. The solid blue line represents data from the literature by Cagran et al. [52]. The solid phase exhibits two clusters which can each be fitted linearly, as indicated by the dashed red lines. The solid red line in-between those lines represents the linear regression of the upper and lower cluster combined. This fit is represented by

$$\epsilon_{684.5,\mathrm{solid}} = 0.623 - 6.31 \cdot 10^{-5} \cdot T_\mathrm{r}, \qquad 1650 < T_\mathrm{r}/\mathrm{K} < 2490. \tag{4.8}$$

In the liquid phase normal spectral emissivity at 684.5 nm, $\epsilon_{684.5,\mathrm{liquid}}$, is fitted by

$$\epsilon_{684.5,\mathrm{liquid}} = 0.153 - 4.71 \cdot 10^{-5} \cdot T_\mathrm{r}, \qquad 2550 < T_\mathrm{r}/\mathrm{K} < 3190. \tag{4.9}$$

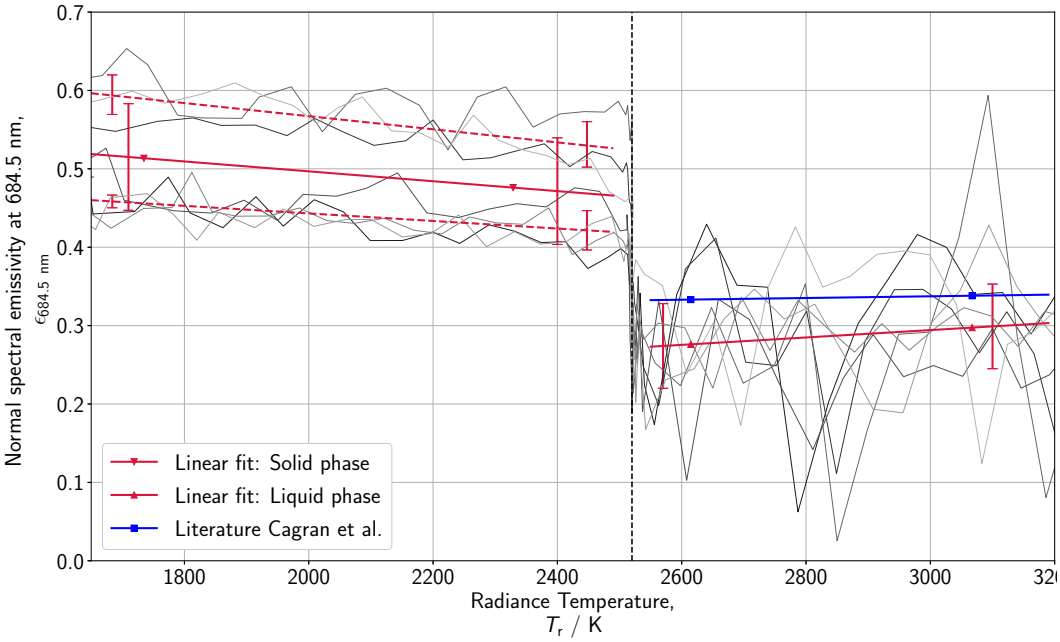

Figure 4.11.: Normal spectral emissivity as a function of radiance temperature for molybdenum. The red lines represent linear regressions of the data. The solid blue line represents data from the literature by Cagran et al. [52]. Figure adapted from [54].

During the evaluation of the liquid phase data, a discrepancy between the obtained values and previously measured data of our group, published in [52], had been detected. Re-evaluation of the original raw data of those previously published showed that the previously published data are indeed too high. These findings have been published in [54].

5. Nickel-Based Superalloy L625

5.1. Motivation

Voestalpine Böhler Edelstahl GmbH & Co KG produces its own version of the nickel-based superalloy 625[1]. The material captivates through great corrosion resistance and general strength and resistance up to very high temperatures and it is a viable material for marine, nuclear and aerospace use. As safety is of utter importance in these fields, knowledge about the behaviour of thermophysical properties is needed for engineers, working with the material. Designing and building for example a turbine blade for a reactor or jet engine is done by casting, or nowadays additive manufacturing, and therefore highly dependent on exact knowledge of thermophysical properties in the liquid phase at high temperatures. As already mentioned before, due to the high reactivity of molten alloys, container-less methods have to be used to access these high temperatures. While many thermophysical properties are more or less easily accessible by ground-based container-less experiments, like ohmic pulse-heating or electromagnetic levitation, others (e.g. viscosity) require different techniques.

A main factor, that impedes levitation techniques on our planet, is gravity. With EML, liquid metal droplets are levitated by an inhomogeneous electromagnetic field against gravity (see sec. 2.4). This leads to deformed samples, which would be perfectly spherical (due to the surface tension of the liquid material) in no- or microgravity conditions and does not allow for the levitating field, which simultaneously heats up the sample, to be turned off during measurements. Therefore, not only surface tension measurement gets slightly more difficult on ground, but also viscosity measurement with ground-based EML techniques is impossible. Other levitation techniques,

[1] (DIN 2.4856, UNS No6625, EN NiCr22Mo9Nb)

like electrostatic levitation (ESL) decouple the heating circuit from the levitation circuit, but the problem gravity provides still exists. The solution to this problem is to conduct experiments in places with very low (apparent) gravity, under so called microgravity conditions. The International Space Station (ISS) is circulating the earth in a low orbit (approx. 400 km above ground) with a speed of $7.66\,\mathrm{km}\cdot\mathrm{s}^{-1}$. Objects on-board the ISS as well as the ISS itself, are therefore in a constant free fall around the earth. As objects fall with the same acceleration, independent of their masses, they appear to be weightless on board the ISS. Thus, microgravity conditions are achieved on board the ISS, even if the gravity field of planet earth would only be reduced to 90 % due to the height of the orbit, where the station travels.

On board the ISS, thermophysical property measurement is performed by the Japan Aerospace Exploration Agency (JAXA) on the Japanese experiment module "Kibo" and by the European Space Agency (ESA) on the European experiment module "Columbus". While experiments on the Japanese module were scheduled to be performed in July 2020, measurements on the European module can only be performed, once the material has been tested under microgravity conditions on board of parabolic flights, conducted by French company Novespace in Bordeaux-Mérignac, in cooperation with DLR and ESA. Tests in microgravity on board of parabolic flights were scheduled to take place in May 2020, but due to the outbreak of SARS-CoV-2 and the ongoing pandemic, these experiments were rescheduled to September 2020. Additionally the flights took place in Germany with intensified security regulations. It was therefore not possible to attend the flights in person. The JAXA ELF experiments on-board the ISS were experimentally challenging. Delayed at first, due to technical problems with the apparatus made measurements possible in December, as opposed to June, when testing was planned.

Table 5.1.: Chemical composition as presented by voestalpine BÖHLER Edelstahl [55]. Numbers represent mass-percentage.

Cr	Mo	Al	Nb	Ni
$\leq$ 21.00	8.50	0.18	3.40	bal.

Table 5.1 shows the composition of the alloy as specified by voestalpine BÖHLER Edelstahl.

5.2. Ground-based Results

5.2.1. Ohmic pulse-heating

OPA measurements for the super-alloy L625 include specific enthalpy as a function of temperature $H_S(T)$ and uncorrected electrical resistivity as a function of temperature $\rho_{IG}(T)$. Expansion measurement was not possible at this point, as the apparatus was set up to simultaneously measure electrical data and normal spectral emissivity with the µs-DOAP and it is impossible to have the apparatus set up in a way which allows to measure expansion data together with the µs-DOAP. A wire with a diameter d = 0.6 mm was drawn out of the material by voestalpine BÖHLER Edelstahl GmbH & Co KG. A total of four samples were analysed to obtain the presented data. Figure 5.1 shows specific enthalpy as a function of temperature. No enthalpy data for comparison could be found in the literature. The experimental data are represented by gray dots and were fitted, quadratically in the solid phase and linearly in the liquid phase.

Enthalpy in kJ·kg^{-1} as a function of temperature in the solid phase was fitted quadratically in the range $1000 \leq T/\mathrm{K} \leq 1568$ by

$$H_{S,s}(T) = 495 - 5.912 \cdot 10^{-1} \cdot T + 4.807 \cdot 10^{-4} \cdot T^2, \quad 1000 \leq T/\mathrm{K} \leq 1568. \tag{5.1}$$

Enthalpy in kJ·kg^{-1} as a function of temperature in the liquid phase was fitted linearly in the range $1640 \leq T/\mathrm{K} \leq 2000$ by

$$H_{S,l}(T) = -173 + 0.72 \cdot T, \qquad 1640 \leq T/\mathrm{K} \leq 2000. \tag{5.2}$$

Electrical resistivity in µΩ·m, assuming initial geometry, is presented in fig. 5.2. The solid phase was fitted linearly in the range $1050 \leq T/\mathrm{K} \leq 1400$ and cubically in the range $1400 \leq T/\mathrm{K} \leq 1568$. The linear part of the solid phase of electrical resistivity as a function of temperature was fitted by

$$\rho_{IG,s}(T) = 1.299 + 6.797 \cdot 10^{-6} \cdot T, \qquad 1050 \leq T/\mathrm{K} \leq 1400. \tag{5.3}$$

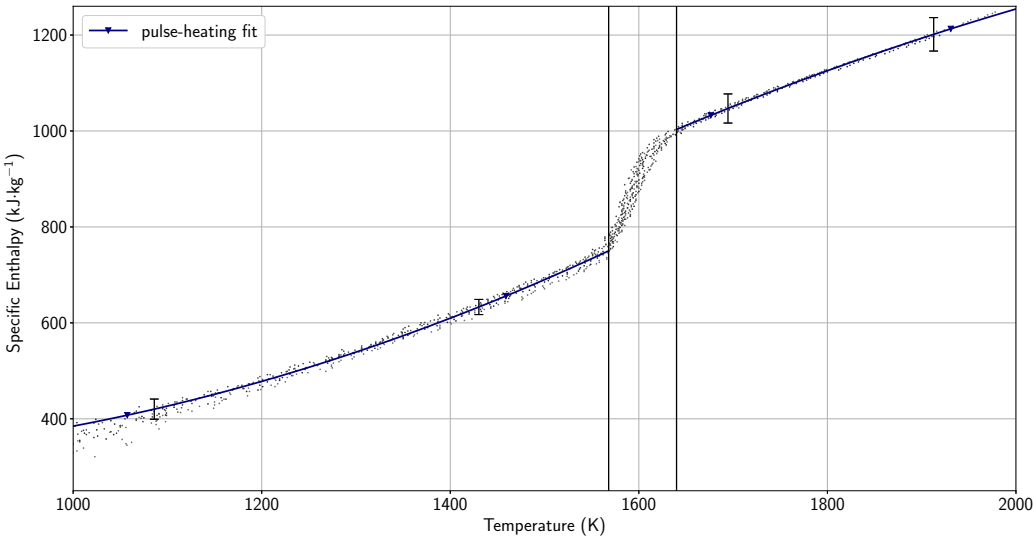

Figure 5.1.: Specific enthalpy data as a function of temperature for the super-alloy L625. The solid blue lines represent regressions to the experimental data, which are represented by the gray dots.

The non-linear part, closer to the melting, of electrical resistivity in μΩ·m, assuming initial geometry, was fitted cubically in the temperature range $1400 \leq T/\mathrm{K} \leq 1568$ by

$$\rho_{\mathrm{IG,s}}(T) = -38 + 8.155 \cdot 10^{-2} \cdot T - 5.581 \cdot 10^{-5} \cdot, T^2 + 1.268 \cdot 10^{-8} \cdot T^3 \qquad 1400 \leq T/\mathrm{K} \leq 1568. \tag{5.4}$$

In the liquid phase, data were fitted linearly in the temperature range $1640 \leq T/\mathrm{K} \leq 2000$ by

$$\rho_{\mathrm{IG,l}}(T) = 1.224 + 4.156 \cdot 10^{-5} \cdot T, \qquad 1640 \leq T/\mathrm{K} \leq 2000. \tag{5.5}$$

Resistivity data are compared to values from the literature by Maglic et al. [56] and Kaschnitz et al. [57]. Data by Kaschnitz et al. are corrected for thermal expansion, data by Maglic et al. assume initial geometry. It has to be noted that the alloy in the literature was an Inconel625 alloy and not the L625 alloy produced by voestalpine BÖHLER Edelstahl GmbH & Co KG.

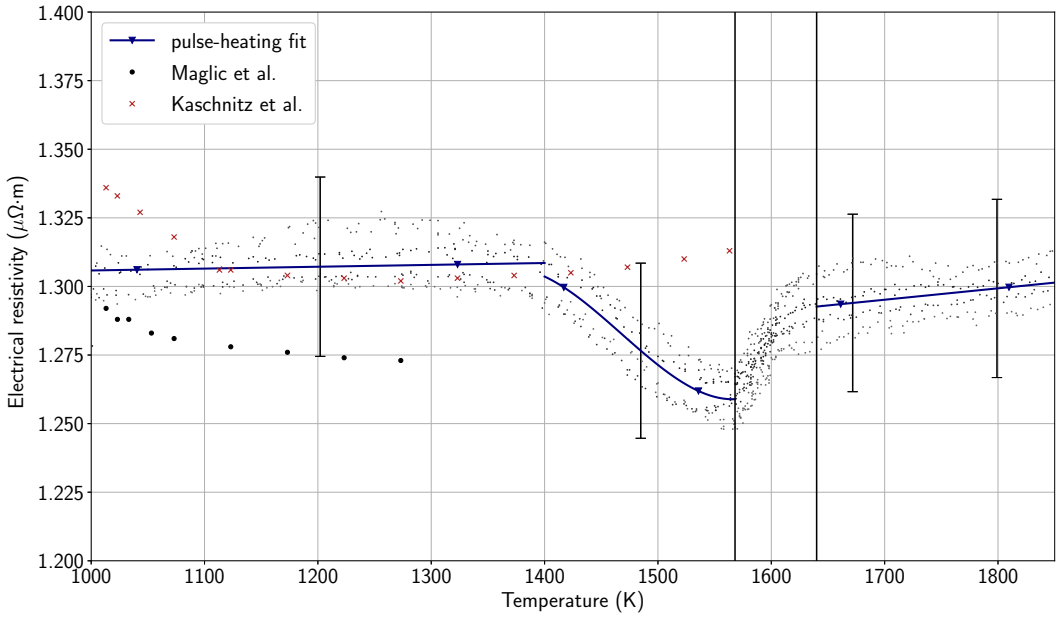

Figure 5.2.: Electrical resistivity, assuming initial geometry, as a function of temperature for the super-alloy L625. The solid blue lines represent regressions to the experimental data, which are represented by the gray dots. Obtained data are compared to values from the literature by Maglic et al. [56], represented by the black circles and by Kaschnitz et al. [57], represented by the red crosses.

The data obtained during this work agree with the data from the literature.

5.3. Microgravity Results

5.3.1. TEMPUS

In this section results from the latest parabolic flight campaign are presented. The L625 alloy was measured on day 3. Six parabolas of the thirty parabolas performed during the day were used for the alloy. Table 5.2 shows the parabolas with comments from the operators. While for each parabola two

Table 5.2.: Overview of the performed parabolas for Alloy L625.

Parabola	Sample ID	Comment
0	1	Not liquid
1	1	OK, SCE
2	1	Solidified during 1st pulse
4	1	Solidified during 1st pulse
5	1	Solidified during 2nd pulse
8	1	Solidified during 2nd pulse
9	1	Solidified during 2nd pulse
10	1	Solidified during 2nd pulse

pulses were performed to record the damped surface oscillations, great care has to be taken when evaluating the obtained data. If the sample solidifies during a pulse, it might be impossible to obtain useful surface tension and viscosity data. As presented in tab. 5.2 all measurements were performed on one sample. The sample was prepared by DLR in an arc furnace and had a mass m = 1.0435 g with an average diameter d_{avg} = 6.0 mm. Figure 5.3 represents SCE viscosity data $\eta(T)$ from the TEMPUS experiments on board of parabolic flights under microgravity. Viscosity data in mPa·s were fitted with a Vogel-Fulcher fit in the range $1520 \leq T/\mathrm{K} \leq 1690$ by

$$\eta(T) = 8.514 \cdot 10^{-3} \cdot \exp\left(\frac{1.131 \cdot 10^4}{T}\right), \qquad 1520 \leq T/\mathrm{K} \leq 1690. \tag{5.6}$$

Figure 5.4 shows SCE surface tension data as a function of temperature from the TEMPUS experiments on-board of parabolic flights under microgravity. Surface tension data in $\mathrm{N{\cdot}m^{-1}}$ were fitted linearly in the range $1520 \leq T/\mathrm{K} \leq 1690$ by

$$\gamma(T) = 1.948 - 1.948 \cdot 10^{-5} \cdot T, \qquad 1520 \leq T/\mathrm{K} \leq 1690. \tag{5.7}$$

TEMPUS data were compared to ground-based EML measurements by Leitner [58]. Fig. 5.4 shows a very good agreement between the microgravity results and the results from ground-based levitation measurements.

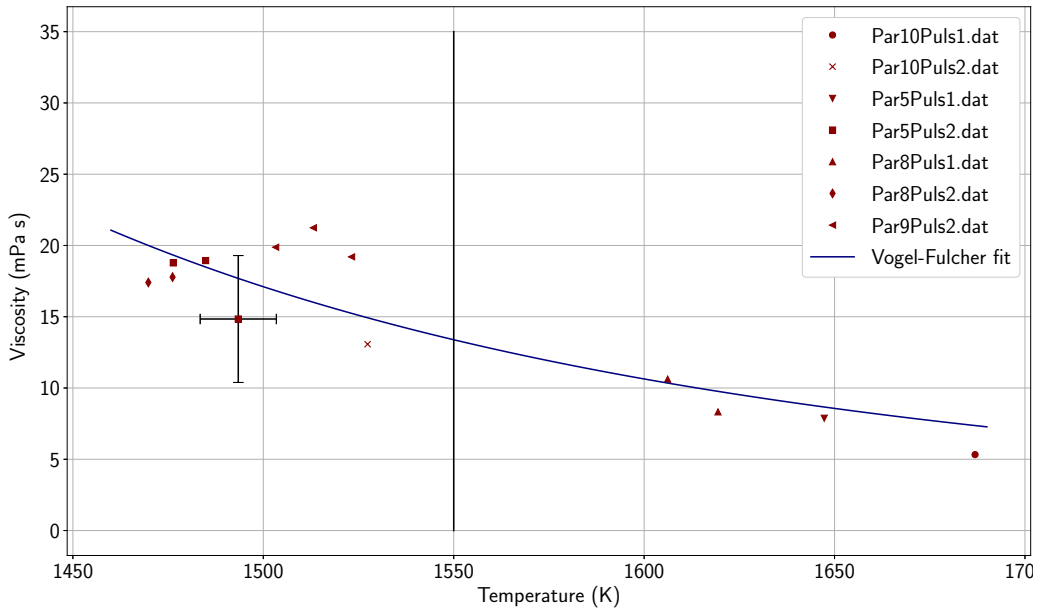

Figure 5.3.: Viscosity data for alloy L625. The markers represent viscosity data from different pulses. The blue line represents a quadratic regression. The vertical black line represents the liquidus temperature of the material.

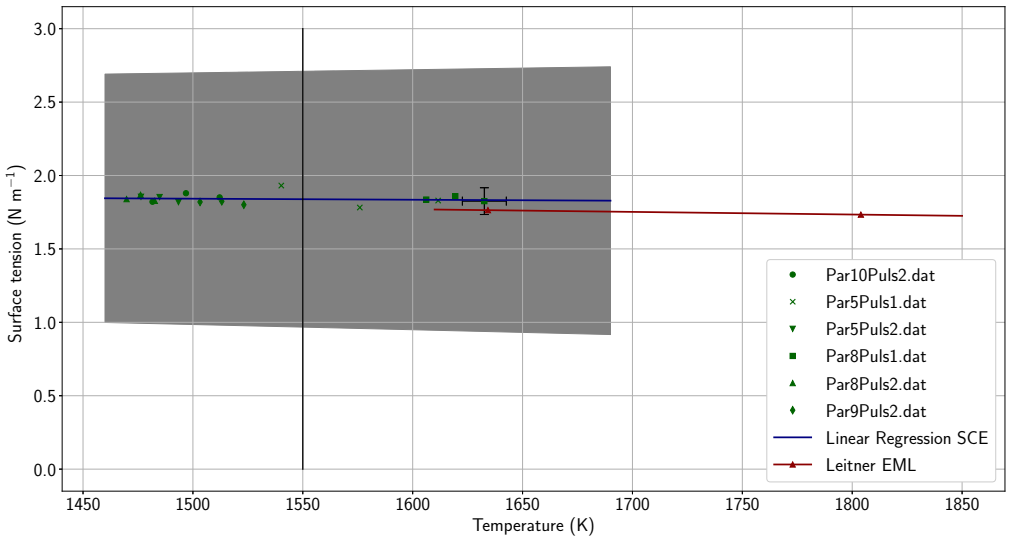

Figure 5.4.: Surface tension data for alloy L625. The markers represent surface tension data from different pulses. The blue line represents a linear regression. The uncertainty of the fit is represented by the grey area. The vertical black line represents the liquidus temperature of the material. The solid red line represents ground-based EML data by Leitner [58].

5.3.2. JAXA ELF

Surface Tension and Viscosity

A total of three samples were processed with the JAXA ELF apparatus at the point this thesis was written. No evaluated data for surface tension or viscosity are available yet, but some interesting observations were made and are summarized in this section.

The first sample was melted but appeared to solidify after some time. When the laser power was increased in order to remelt the sample, it showed strong evaporation and had to be cooled down. After cooling down, the sample was reheated. An oscillation sweep was performed on the sample, which was not unsuccessful, as the sample did oscillate. While the pyrometer showed a temperature larger than 1600 °C, the camera showed that the sample was deformed and had many lumps. The experiment was stopped and the sample was retrieved.

The second sample exhibited a very similar behaviour. When heating the sample to melt it, evaporation started. During the oscillation sweep, the sample displayed not the expected spherical shape of a molten liquid in microgravity, but was again lumpy. The experiment was then stopped and the sample retrieved.

The third sample was processed at the next testing day. Oscillations could be excited but the sample displayed the typical anomalies.

As the samples need to be analysed, once they return back to earth and testing is not completed yet, no graphical results are presented in this work. The assumption is that the samples oxidised during the heating process and it were the oxides on the sample surface that evaporated. Another indication for sample oxidation is that the sample seemed to solidify, although the temperature, displayed by the pyrometer, was higher than its liquidus temperature. It is possible that the oxidation on the surface raised the melting temperature to higher values. However, no final conclusion can be drawn at this point as the samples need to be observed and subjected to further investigations. Space experiments are complex and hard to perform. The Japanese team, responsible for the JAXA ELF apparatus, ensured a safe

processing of the sample by designing a controlling circuit to deal with the surface charge changing during the baking process. All available data will be sighted and the samples analysed further.

Density

Preliminary density data could be obtained from two of the three analysed samples. Detailed information about the data analysis process can be found in the PhD thesis of Jannatun Nawer which is in preparation at the moment. A short overview over the difficulties in obtaining density data with the JAXA ELF setup is given in this section.

Density data are obtained by analysing the video data of the JAXA ELF camera, which provides shadow images of the sample. The camera has a temporal resolution of 60 Hz, but as a large amount of video data is sent from the ISS to earth via a downlink, the video data are interlaced resulting in a temporal resolution of 30 Hz. The first challenge is to synchronize the temperature data from the pyrometer with the video footage. After that the x, y and z position of the sample has to be plotted together with temperature to find segments in the video data, where the sample position is stable. Finally the sphericity of the sample needs to be checked. Only segments where the sample is stable and spherical provide useful density data.

Figure 5.5 shows preliminary density data from the JAXA ELF experiments. The dark and lightgrey markers represent density data for two different samples. The solid blue line represents a linear regression to the obtained experimental data. Density data $D(T)$ in $\mathrm{kg \cdot m^{-3}}$ as a function of temperature were fitted linearly in the temperature range $1630 \leq T/\mathrm{K} \leq 1760$ by

$$D(T) = 8994 - 0.781 \cdot T, \qquad 1630 \leq T/\mathrm{K} \leq 1760. \tag{5.8}$$

The data obtained with JAXA ELF in microgravity are compared to ground-based data by Heugenhauser and Kaschnitz [59] (Push-rod Dilatometry) and preliminary ground-based EML data by Leitner [58]. While the slope between all data sets is in excellent agreement, micro-gravity data are 1.7 % higher than the push-rod dilatometry data and 3 % higher than the ground

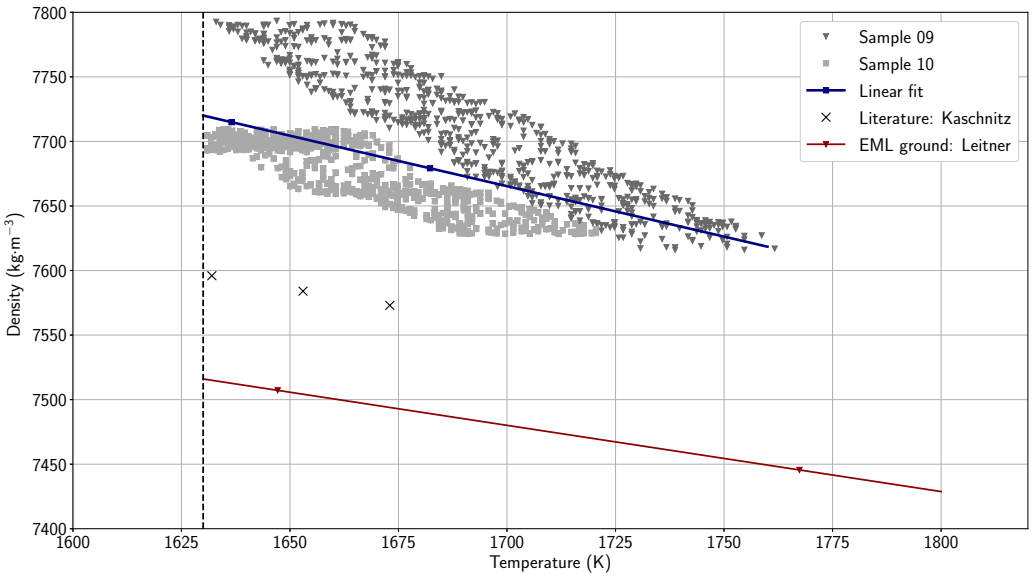

Figure 5.5.: Preliminary density data for alloy L625. The darkgrey downwards facing triangles represent data obtained with JAXA ELF from sample 09, the lightgrey squares represent data obtained with JAXA ELF from sample 10. The solid blue line represents a linear fit to the experimentally obtained data. The solid red line represents preliminary data obtained with the ground-based EML setup by Leitner [58]. The black crosses represent data from the literature by Heugenhauser and Kaschnitz [59]. The dashed vertical line represents the liquidus temperature of the alloy.

based EML data. So far no thorough uncertainty analysis was performed, but a first estimate suggests uncertainty for microgravity results obtained with JAXA ELF to be at least 3 %.

6. Uncertainty

This chapter focuses on uncertainty determination of the different measurement techniques, used in this work. If not indicated otherwise, all uncertainty estimation was performed according to the "Guide to the Expression of Uncertainty in Measurement" (GUM) [1] with a coverage factor $k = 2$. As many of these techniques have been used for measurement at the Thermo- and Metalphysics Group of the Institute of Experimental Physics at Graz University of Technology, uncertainty determination was described in the past. If a good and thorough description of uncertainty determination for a method can be found in the literature, the reader is referred to the corresponding publication or thesis.

6.1. Ohmic Pulse-heating Apparatus

6.1.1. Electrical Data

Uncertainty determination for electrical data was performed following the doctoral thesis of Wilthan [60]. The uncertainty estimation routine was adopted by Macher [61] who provided a Matlab code to determine uncertainty for electrical data obtained with the ohmic pulse-heating system. Exemplary results for uncertainty for the NIST SRM 1155a are presented in tab. 6.1

6.1.2. Expansion Data

Uncertainty determination for expansion data was performed following the doctoral thesis of Leitner [8] and the publication of Matus [62] who

Table 6.1.: Assessed uncertainties of the measured thermophysical properties $\rho_{\mathrm{IG}}(T)$ (electrical resistivity, assuming initial geometry) and $H_s(T)$ (specific enthalpy) for NIST SRM 1155a.

Property y	Unit	Uncertainty	State	Method
$\rho_{\mathrm{IG}}(T)$	$\mu\Omega\cdot\mathrm{m}$	2.5 %	solid	OPA
$\rho_{\mathrm{IG}}(T)$	$\mu\Omega\cdot\mathrm{m}$	2.5 %	liquid	OPA
$H_s(T)$	$\mathrm{kJ\cdot kg^{-1}}$	2.5 %	solid	OPA
$H_s(T)$	$\mathrm{kJ\cdot kg^{-1}}$	2.9 %	liquid	OPA

devised a method to determine uncertainty coefficients of linear regressions. Exemplary results for uncertainty of the NIST SRM 1155a are presented in tab. 6.2.

Table 6.2.: Assessed uncertainties of the measured thermophysical properties $D(T)$ (Density) and $\rho_{\mathrm{corr}}(T)$ (electrical resistivity, corrected for thermal expansion).

Property y	Unit	Uncertainty	State	Method
$D(T)$	$\mathrm{kg\cdot m^{-3}}$	2.5 %	solid	OPA
$D(T)$	$\mathrm{kg\cdot m^{-3}}$	3 %	liquid	OPA
$\rho_{\mathrm{corr}}(T)$	$\mu\Omega\cdot\mathrm{m}$	5.5 %	solid	OPA
$\rho_{\mathrm{corr}}(T)$	$\mu\Omega\cdot\mathrm{m}$	4.5 %	liquid	OPA

6.2. Microsecond Division of Amplitude Photopolarimeter

Uncertainty estimation of the µs-DOAP was the task of A. Eber who conducted his master thesis [18] under the guidance of this author. Eber analysed a multitude of influences on uncertainty of the µs-DOAP and concluded that the biggest part, contributing to uncertainty, originates from repeatability. Additionally, µs-DOAP emissivity data show an oscillating behaviour which deserves to be studied intensely in order to improve the

obtained results. The resulting uncertainty for emissivity data obtained with the μs-DOAP lies in the range of 10 % of the measured value.

6.3. Dynamic Scanning Calorimetry

Uncertainty for DSC measurements is governed by the repeatability, assuming the apparatus is calibrated correctly and the experimenter takes all precautions, necessary to ensure measurement quality. This includes setting up the crucibles on the sample holder in a reproducible way, cleaning the samples and making sure the surrounding room temperature stays constant during a measurement cycle. The uncertainty estimation, determined statistically, for specific heat capacity measurements on the NIST SRM 1155a is presented in 6.3.

6.3.1. Solidus Determination by Enthalpy Matching

The procedure to estimate the uncertainty for solidus temperature by enthalpy matching of DSC and OPA data, as explained in section 3.2 is described in this section. Temperature as a function of enthalpy, obtained with DSC measurements is fitted quadratically and extrapolated to the assumed solidus temperature. The pyrometer signal of the OPA measurements is plotted as a function of enthalpy, also obtained with OPA, and fitted linearly in the solid phase, close to the melting and at the melting plateau. These two fits are performed several times to find the worst case scenarios (overestimating enthalpy at the solidus temperature and underestimating enthalpy at the solidus temperature). The two worst case enthalpy values are inserted in the extrapolation of temperature as a function of enthalpy of the DSC data to determine the uncertainty of the solidus temperature. For NIST SRM 1155a the uncertainty of the solidus temperature was ΔT_s = 10 K.

6.3.2. Combining DSC and OPA data

Uncertainty estimation for the corrected and uncorrected electrical resistivity from combined DSC and OPA data is found in tab. 6.3.

Table 6.3.: Assessed uncertainties of the measured thermophysical properties. If not indicated with an asterisk all uncertainty values are calculated according to the GUM with a coverage factor $k = 2$. Asterisk: uncertainty value assessed statistically.

Property y	Unit	Uncertainty	State	Method
$\rho_{\mathrm{IG}}(T)$	$\mu\Omega\cdot\mathrm{m}$	3 %	solid	DSC + OPA
$\rho_{\mathrm{corr}}(T)$	$\mu\Omega\cdot\mathrm{m}$	5 %	solid	OPA + DSC
$c_{\mathrm{p}}(T)$*	$\mathrm{kJ\cdot kg^{-1}K^{-1}}$	1.8 % to 3 %	solid	DSC

6.4. Electromagnetic Levitation

Uncertainty for surface tension data with the EML apparatus was analysed thoroughly by Werkovits [26]. The uncertainty of single data points was estimated accordingly and the uncertainty of the fit parameters was estimated following the guide of Matus [62].

6.5. TEMPUS - Tiegelfreies Elektromagnetisches Prozessieren von Proben unter Schwerelosigkeit

Sample Coupling Electronics data was used to determine surface tension and viscosity. Uncertainty estimation for this method was mainly governed by the evaluation process. As explained in section 2.5, data from single pulses needed to be singled out and analysed in order to obtain surface tension and viscosity. Choosing the starting and ending point of single pulse data influences the resulting oscillation frequency and damping constant.

By choosing several different starting and ending points for the singled-out pulse data, an estimation of the uncertainty for viscosity and surface tension data was made. The uncertainty for viscosity was estimated (conservatively) to be in the range of 10 % of the measured value. The uncertainty for surface tension was estimated to be in the range of 5 % of the measured value, as the evaluation process was more stable to different starting and ending points.

7. Conclusion and Outlook

Thermophysical properties of tungsten, molybdenum, the NIST Standard Reference Material 1155a and the nickel-based superalloy 625 were determined experimentally. The methods used in this work were ohmic pulse-heating, microsecond division of amplitude polarimetry, dynamic scanning calorimetry, electromagnetic levitation on ground as well as electromagnetic levitation and electrostatic levitation under microgravity conditions on-board of parabolic flights and the International Space Station. The thermophysical properties determined in this work were specific enthalpy, electrical resistivity, specific heat capacity, thermal conductivity, thermal diffusivity, normal spectral emissivity at 684.5 nm, density, surface tension and viscosity, all as a function of temperature.

Surface tension data for the nickel-based superalloy 625, measured on-board of parabolic flights, were compared to surface tension data, measured by means of on-ground EML. The comparison displayed extraordinary good agreement between the microgravity and ground-based data. Viscosity data for the superalloy 625 were determined and show a temperature trend, similar to other nickel-based superalloys. These data could not be compared to ground-based measurements, as viscosity measurement is impossible with EML set-ups under the influence of gravity.

The NIST SRM 1155a, an AISI 316L stainless steel, was characterized by means of ohmic pulse-heating, dynamic scanning calorimetry and electromagnetic levitation and compared to data from the literature of similar steels, classifying as AISI 316 or AISI 316L. The comparison showed very good agreement with data from the literature in general, but for some properties the slightly different composition showed a significant difference. This was mostly observed for surface tension, where the influence of varying sulphur content showed significant differences in the obtained data, compared to the literature.

Additionally, thermal diffusivity, specific heat capacity and normal spectral emissivity at 684.5 nm as a function of temperature, respectively radiance temperature were determined experimentally. While measuring normal spectral emissivity at 684.5 nm, several problems with the μs-DOAP arose. The pellicle foil, which is used to directly observe the hole aperture inside the polarisation state detector, was destroyed during the long period of inactivity the apparatus had to endure. If possible this foil should be replaced in the future. When measuring normal spectral emissivity with the DOAP system, the data show an oscillating behaviour. Further investigation is necessary to determine the origin of said oscillations and optimize the measuring process and data evaluation.

The experiments on-board the International Space Station were delayed several times due to technical problems. When this thesis was close to being finished, an experiment to measure surface tension and viscosity of the nickel-based superalloy L625 with the JAXA ELF on-board the ISS was carried out. Results from this experiment will be evaluated and published in the near future. A comparison between ground-based surface tension, the JAXA ELF experiments and the TEMPUS experiments will be performed. Viscosity data from JAXA ELF and TEMPUS will also be compared to each other.

As the closure of the Thermo- and Metalphysics group at Graz University of Technology is due next year, the biggest task in the near future will be to ensure a clean and proper transition of the measurement apparatuses, described in this work, and to make sure that the important task of characterising high melting metals and alloys for academia and industry continues.

8. Publications

I P. Pichler, B. J. Simonds, J. W. Sowards and G. Pottlacher. "Measurements of thermophysical properties of solid and liquid NIST SRM 316L stainless steel." In: *J. Mater. Sci.* 55 (2020), pp. 4081-4093. [Status: published]

II P. Pichler and G. Pottlacher. "Thermal Conductivity of Liquid Metals." In: *Impact of Thermal Conductivity on Energy Technologies*, Aamir Shahzad, IntechOpen (2018), pp. 81-96. [Status: published]

III A. Eber, P. Pichler and G. Pottlacher. "Re-investigation of the Normal Spectral Emissivity at 684.5 nm of Solid and Liquid Molybdenum." In: *Int. J. Thermophys* (2020). [Status: published]

IV P. Pichler, T. Leitner, E. Kaschnitz, J. Rattenberger and G. Pottlacher. "Surface Tension and Thermal Conductivity of NIST SRM 316L Stainless Steel." [Status: manuscript in preparation]

8.1. Measurements of thermophysical properties of solid and liquid NIST SRM 316L stainless steel

P. Pichler, B. J. Simonds, J. W. Sowards and G. Pottlacher. "Measurements of thermophysical properties of solid and liquid NIST SRM 316L stainless steel." In: *J. Mater. Sci.* 55 (2020), pp. 4081-4093. DOI: https://doi.org/10.1007/s10853-019-04261-6.

SHORT SUMMARY

A set of thermophysical properties for the NIST SRM 1155a, an AISI 316L stainless steel was obtained. Obtained data are compared with other AISI 316L steels from the literature. Data will be used for multi-physics models and simulations.

REMARKS ON AUTHORSHIP

P. Pichler performed pulse-heating and DSC measurements on the material. He wrote chapters "Abstract", "Material and experimental methods", "Results", "Uncertainties" and "Conclusions"
B. J. Simonds provided the material and coordinated the collaboration between authors. He wrote chapter "Introduction".
J. W. Sowards performed calculations and modelling on the material and contributed to chapter "Introduction".
G. Pottlacher supervised the measurement and publication process.

All authors were involved in the text revision process.

Measurements of thermophysical properties of solid and liquid NIST SRM 316L stainless steel

Peter Pichler, Brian J. Simonds, Jeffrey W. Sowards & Gernot Pottlacher

Journal of Materials Science

ISSN 0022-2461
Volume 55
Number 9

J Mater Sci (2020) 55:4081-4093
DOI 10.1007/s10853-019-04261-6

Springer

J Mater Sci (2020) 55:4081–4093

Metals & corrosion

Measurements of thermophysical properties of solid and liquid NIST SRM 316L stainless steel

Peter Pichler[1,*], Brian J. Simonds[2], Jeffrey W. Sowards[3], and Gernot Pottlacher[1]

[1] Institute of Experimental Physics, Graz University of Technology, NAWI Graz, Petersgasse 16, 8010 Graz, Austria
[2] National Institute of Standards and Technology, 325 Broadway, Boulder, CO 80305, USA
[3] Present address: NASA Marshall Space Flight Center, Huntsville, AL 35812, USA

Received: 20 September 2019
Accepted: 27 November 2019
Published online: 9 December 2019

ABSTRACT

In this work, we perform high accuracy measurements of thermophysical properties for the National Institute of Standards and Technology standard reference material for 316L stainless steel. As these properties can be sensitive to small changes in elemental composition even within the allowed tolerances for an alloy class, by selecting a publicly available standard reference material for study our results are particularly useful for the validation of multiphysics models of industrial metal processes. An ohmic pulse-heating system was used to directly measure the electrical resistivity, enthalpy, density, and thermal expansion as functions of temperature. This apparatus applies high current pulses to heat wire-shaped samples from room temperature to metal vaporization. The great advantage of this particular pulse-heating apparatus is the very short experimental duration of 50 μs, which is faster than the collapse of the liquid wire due to gravitational forces, as well as that it prevents any chemical reactions of the hot liquid metal with its surroundings. Additionally, a differential scanning calorimeter was used to measure specific heat capacity from room temperature to around 1400 K. All data are accompanied by uncertainties according to the guide to the expression of uncertainty in measurement.

Jeffrey W. Sowards: Formerly with NIST.

Address correspondence to E-mail: peter.pichler@tugraz.at

https://doi.org/10.1007/s10853-019-04261-6

Introduction

The National Institute of Standards and Technology (NIST) standard reference material (SRM) for 316L stainless steel (1155a) has recently been used for studies of intense laser light coupling in metal to provide data for the validation of multiphysics models of industrial laser processes like welding, cutting, and additive manufacturing [1]. In order to reduce the costs associated with empirical trial-and-error production development, manufacturers are increasingly looking to multiphysics computer simulations to more rapidly optimize process parameters. Generally, these models simulate the laser heating of metal followed by heat flow and fluid transport of the solid/molten metal system in order to predict the evolution of the fusion zone and surrounding heat-affected zone. Therefore, in addition to laser light coupling they also require many thermophysical material properties over a very wide temperature range across solid and liquid phases. Ideally, modelers would be able to find accurate thermophysical property values with known uncertainties spanning the wide temperature range necessary for the exact alloy composition they are modeling. However, due to the limited amount of data available modelers often resort to using values for materials of similar, but not exact, composition to that which they are studying, and extrapolate for values at temperatures not found in the literature.

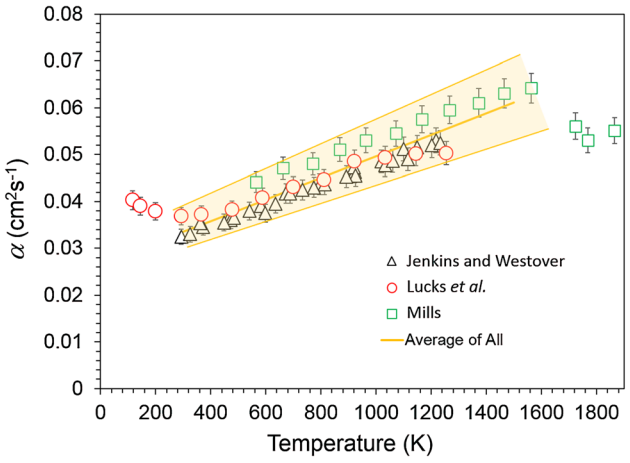

Figure 1 Experimental values for the thermal diffusivity of 304 stainless steel. The solid line represents an average of all values between room temperature and the melting point. The shaded area represents an uncertainty of 15%.

Thermal diffusivity is the relevant material property used in the heat equation to model transient heat conduction during, e.g., welding and additive manufacturing. Figure 1 shows experimental values for thermal diffusivity and their uncertainty, as a function of temperature for the common industrial alloy 304 stainless steel. These data were taken from three different laboratories using different feedstocks for 304 stainless steel [2–4]. Even though these materials meet the composition requirements for 304 stainless steel, the allowed tolerance range for the primary constituent elements Fe, Cr, Ni, and Mo [5] can lead to variations in the microstructure that the thermal diffusivity is sensitive to [6]. The solid curve is an average of all values between room temperature and the melting point. The shaded band spans ±15%, which encompasses all experimental values and their uncertainties. This illustrates the dilemma for the modeler which is to decide which data set to use.

To illustrate the effect that this can have on a model prediction, we perform a simple numerical exercise. We model the temperature field resulting from an instantaneous heat load of 100 J applied as a point source to one surface of a semi-infinite body at time $t = 0$. This is a very simplified approximation of a laser spot weld, and the temperature field in three spatial dimensions x, y, and z is given by

$$T(x,y,z,t) = \frac{Q}{(4\pi\alpha t)^{3/2}} \exp\left(-\frac{x^2+y^2+z^2}{4\alpha t}\right), \qquad (1)$$

where Q is the heat load (100 J), t is time, and α is the thermal diffusivity. For α, we use a nominal value of $0.0557\,\mathrm{cm^2\,s^{-1}}$ which is found by taking an average from Fig. 1. Equation (1) is solved analytically for the time-dependent temperature at points on the surface ($y, z = 0$ mm) of the semi-infinite body at three distances ($x = 1$ mm, 2 mm, and 3 mm) away from the location of the heat load ($x, y, z = 0$) as shown in the inset of Fig. 2a. These results are plotted as solid curves in Fig. 2a. Next, we repeat the calculations but for values of α that represent the spread found in the literature, approximately ±15%. These results are given as dashed curves in Fig. 2a. It is assumed that the temperature of the molten weld pool cannot exceed the boiling point of stainless steel (assumed here to be 2800 K).

From these curves, we derive the average thermal gradient, G, according to

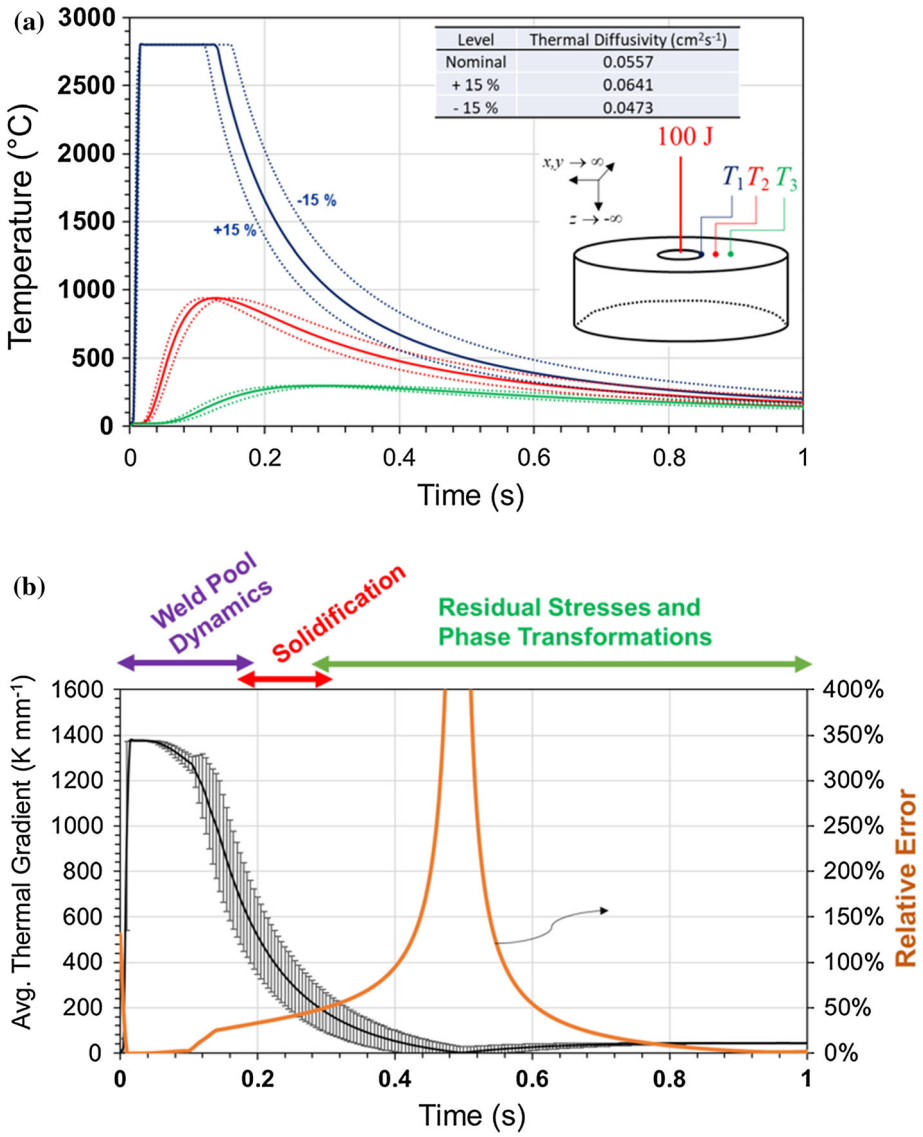

Figure 2 Analytical solutions to the heat transfer equation at three points along the surface of a semi-infinite body after an instantaneous heat load of 100 J are given as solid lines in **a**. An inset shows the location of the three temperature probes, $T1$, $T2$, and $T3$. The dashed lines show the temperature range resulting from a 15% variance in thermal diffusivity. The average thermal gradient at the material surface is computed and plotted as the solid black curve in **b**. The error bars indicate the spread of values from the computed temperature ranges in **a**. The right axis in **b**. shows the relative error caused by the thermal diffusivity-induced uncertainty in temperature.

$$G = \frac{\Delta T}{(x_{T_3} - x_{T_1})}. \tag{2}$$

The thermal gradient is important for development of metallurgical phenomena such as residual stress and phase transformations. Stainless steel alloy 316, in particular, (which is the SRM used herein) can exhibit a strong tendency toward a shift in solidification mode due to increased thermal gradient, resulting in an increase in weld cracking sensitivity [7]. G is plotted in Fig. 2b. on the left ordinate as a solid black line found using the nominal value of α. The error bars represent the deviation that occurs due to the temperature range resulting from different values of α. This range is then used to determine the time-dependent relative error in the average thermal gradient, which is plotted on the right ordinate. Its value exceeds several hundred percent with the peak value precisely in the region where the final weld properties are determined. In these calculations, we use a single, non-temperature-dependent value for α for simplicity. However, using a temperature-dependent value would not change the relative error as whichever temperature-dependent values chosen would still have a $\pm 15\%$ uncertainty to cover the range found in the literature. Together, this exercise shows that not only can the relative error in the predictions be exceedingly large, but that it is largest precisely in the region of most interest for predicting the properties of the weld due to variation in residual stress and phase transformations. Furthermore, this variation is only due to the uncertainty of a single

thermophysical parameter. This will undoubtedly grow when the variation in all parameters needed for full multiphysics models is considered.

In practice, modelers use these variations as guardrails—upper and lower bounds—on the parameters used for their models. These parameters are adjusted within these bounds based on comparisons of their model outputs to measured quantities through a validation process. Although this procedure is useful in practice, it does not allow one to rigorously test the capability of the model for predicting weld performance outside the narrow scope of experimental conditions for which the model is validated. The vast parameter space allowed by the variation in thermophysical properties allows a model to be tuned to give a satisfactory answer without ever knowing if the chosen parameters are accurate, which limits the model's ability to be predictive. The larger context of the work presented here is that our measured material properties are directly linked to experimental data useful for laser weld model validation [1], which will allow for more rigorous testing of laser weld model predictions.

Material and experimental methods

The material analyzed is an AISI 316 stainless steel. The exact composition is given in Table 1.

Two experimental systems were used to measure the thermophysical properties presented in this work. A subsecond ohmic pulse-heating apparatus (OPA) was used to measure temperature-dependent specific enthalpy, electrical resistivity, thermal radial expansion, and density. In addition, a commercial differential scanning calorimeter (DSC), the NETZSCH DSC 404 C Pegasus[1], was used to obtain specific heat as a function of temperature. With the obtained DSC data, it is also possible to expand the low-end temperature range of the OPA data to room temperature.

[1] Certain commercial equipment, software, and/or materials are identified in this paper in order to adequately specify the experimental procedure. In no case does such identification imply recommendation or endorsement by the National Institute of Standards and Technology, nor does it imply that the equipment and/or materials used are necessarily the best available for the purpose.

Ohmic pulse heating

The pulse-heating apparatus at Graz University of Technology was originally developed in the 1990s by Kaschnitz [9] and has been previously described in reference [10]. Wire-shaped samples with a diameter of 0.7 mm and a length of 60 mm are polished with abrasive paper (ISO Grit designation P1200), cleaned with acetone, and placed into a sample holder. This holder is then put into the electrical circuit containing a 500 µF capacitor bank and is placed inside a slightly pressurized (1.3 bar) nitrogen-filled chamber to prevent arcing. The chamber has optical access windows for a pyrometer and camera. The capacitor bank is charged to about 8 kV that is then applied to the wire. The experiment is initiated by a Krytron-triggered ignition. The same mechanism is used to precisely stop the experiment at a predefined time, by dissipating the residual voltage on the capacitor bank across a graphite resistor instead of over the (evaporated) sample. Depending on the ohmic resistance of the sample, the voltage drives a large current (up to 10 kA) through the wire, generating strong heating. Within 50 µs, the sample's temperature rises past its melting point, through the liquid phase until it finally evaporates. One benefit of these short timescales is the inability of the wire to collapse due to the gravitational force in the liquid state. In fact, the liquid column stands vertically in the sample holder, expanding radially, until it explodes. A second benefit is it being quasi-containerless: The wire is clamped at two end points, and the short time scales suppress chemical reactions with these connections and its environment. Because very high currents are rapidly switched on and off, all measuring leads are shielded copper and lead into a Faraday room where the computer for data acquisition resides.

Temperature

Temperature measurements in our OPA system were performed with an optical pyrometer operating at a wavelength of 1569.5 nm. For accurate temperature measurements, it is necessary to know the material's emissivity at the pyrometer measuring wavelength as a function of temperature. However, under the assumption that emissivity in the liquid phase stays constant, it is possible to calibrate the pyrometer by identifying the melting plateau in the pyrometer signal and assigning the known melting temperature

Table 1 Certified mass fraction values for SRM 1155a [8]

Element	Mass fraction/%	Coverage factor, k
Carbon (C)	0.0260 ± 0.0036	2.45
Cobalt (Co)	0.225 ± 0.018	2.26
Chromium (Cr)	17.803 ± 0.099	2.20
Copper (Cu)	0.2431 ± 0.0050	2.20
Iron (Fe)	64.71 ± 0.12	2.00
Manganese (Mn)	1.593 ± 0.060	2.06
Molybdenum (Mo)	2.188 ± 0.015	2.18
Niobium (Nb)	0.0082 ± 0.0014	3.18
Nickel (Ni)	12.471 ± 0.056	2.20
Phosphorus (P)	0.0271 ± 0.0012	2.11
Silicon (Si)	0.521 ± 0.017	2.03
Titanium (Ti)	0.0039 ± 0.0012	2.45
Vanadium (V)	0.0725 ± 0.0046	2.23
Tungsten (W)	0.0809 ± 0.0059	2.45
Oxygen (O)[a]	0.003	

[a]Oxygen content was estimated from one or more NIST or collaborator test methods

to this value. Due to the sensitivity of the pyrometer photodiode (InGaAs), it is not possible to measure surface radiance below a sample temperature of 1100 K. Instead, we extend the range to lower temperatures by correlation with DSC results as will be explained later.

Enthalpy

Because of the short duration of the experiment, heat losses are negligible, and it is assumed that the electrical energy is completely converted into heat. Thus, it is possible to determine the supplied specific heat $Q_S(t)$ by integrating the electrical power according to

$$Q_S(t) = \frac{1}{m} \cdot \int_0^t U(t') \cdot I(t')\, \mathrm{d}t', \tag{3}$$

where m is the mass of the specimen, $U(t')$ the voltage drop along the specimen at time t', and $I(t')$ the current across the specimen at time t'. As pulse heating is an isobaric process, the specific enthalpy is given by Eq. (3). The voltage is measured by contacting the sample with two molybdenum knives, with a distance l between one other, and measuring two voltage drops to a common ground. The difference of these voltage drops yields the voltage drop $U(t')$ along the specimen. Current is measured inductively with a Pearson probe [11]. The mass is determined from the diameter d of the sample at room temperature measured with a laser micrometer, the distance between the voltage knives l, and the density at room temperature.

Electrical resistivity

The resistivity of a conducting material is defined as

$$\rho(t) = R(t) \cdot \frac{A(t)}{l(t)}, \tag{4}$$

with $R(t)$ the time-dependent resistance, $A(t)$ the time-dependent specimen cross-sectional area, and $l(t)$ the time-dependent length of the sample. Note that because of the high heating rates, the length of the sample remains unaffected during the experiment, $l(t) = l(t_0) = l$. According to Ohm's law, Eq. (4) further yields

$$\rho(t) = \frac{U(t)}{I(t)} \cdot \frac{d(t)^2 \cdot \pi}{4 \cdot l}. \tag{5}$$

It is useful to define the resistivity according to the samples initial geometry (IG) by

$$\rho_{\mathrm{IG}}(t) = \frac{U(t)}{I(t)} \cdot \frac{d_{\mathrm{RT}}^2 \cdot \pi}{4 \cdot l_{\mathrm{RT}}}, \tag{6}$$

with d_{RT} and l_{RT} the diameter and distance between the voltage knives at room temperature (RT), respectively. Thus, resistivity including considerations of thermal expansion can be defined as

$$\rho(t) = \rho_{\mathrm{IG}}(t) \cdot \left(\frac{d(t)}{d_{\mathrm{RT}}}\right)^2. \tag{7}$$

Thermal expansion and density

Thermal expansion was measured by obtaining shadow images of the expanding wire every 2.5 µs. To obtain the fast data processing rates for these experiments, a mechanically masked CCD chip was used. Only 8 pixel-rows (with 384 pixels each) of the chip were exposed, leaving the remainder of the chip as a fast buffer storage. Therefore, it was possible to obtain up to 10 images of a small cross section of the expanding wire during an experiment. The unheated wire, with a diameter of 0.7 mm, occupies approximately 140 pixels per row. The spatial resolution is approximately 0.6 pixels. Before the experiment was started, a set of pictures of the cold wire was taken. Summing over the lines of each obtained picture produces an intensity profile from which the diameter of the wire was determined by taking the full

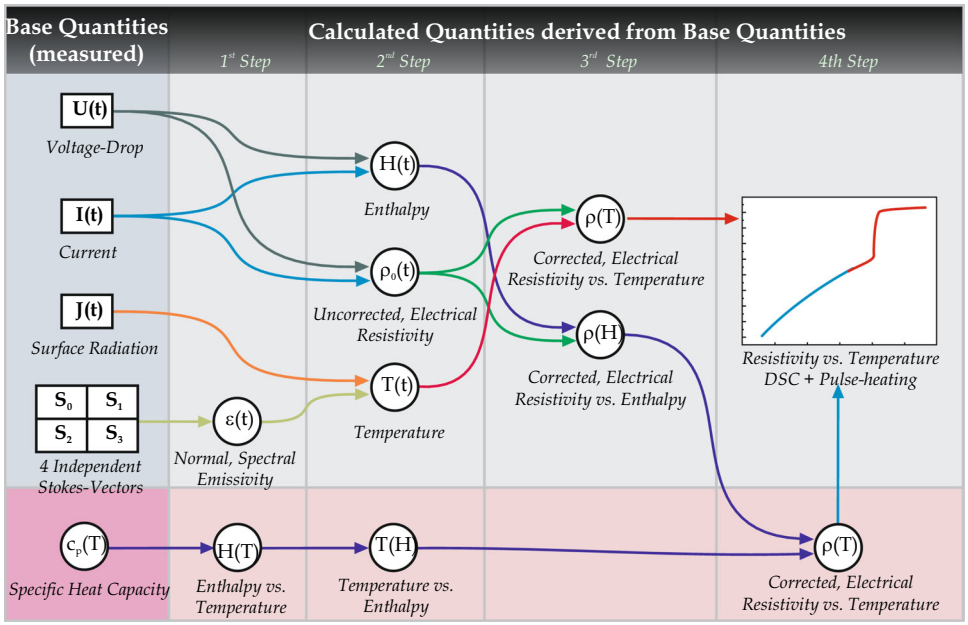

Figure 3 Flowchart on how to expand the temperature range for the OPA measurements with the help of a DSC.

Table 2 Solidus and liquidus temperature of SRM 1155a

	T/K	ΔT/K
T_s	1675	15
T_l	1708	30

T is the temperature, and ΔT is the temperature uncertainty ($k = 2$)

width at half maximum (FWHM) of the intensity profile. All measured quantities shared the same time basis due to a common trigger pulse, and a temperature was assignable to each of the obtained pictures. The volume expansion as a function of temperature was then calculated by the ratio of the FWHM value of the hot wire at a certain time and temperature, $d(T)$, to the FWHM value of the cold wire d_0

$$\frac{V(T)}{V_0} = \left(\frac{d(T)}{d_0}\right)^2. \tag{8}$$

Equation (8) is only true when longitudinal expansion of the wire is prevented and only radial expansion of the wire occurs. In pulse-heating experiments, this is the case as shown by Huepf [12].

Density as a function of temperature $D(T)$ can then be derived by combining the density at room temperature D_0 with the volume expansion

$$D(T) = D_0 \cdot \left(\frac{d_0}{d(T)}\right)^2 \tag{9}$$

with a more detailed explanation found in [13].

Differential scanning calorimeter (DSC)

To measure specific heat capacity in the solid phase and extend the temperature range of the OPA data, a commercial DSC, the NETZSCH DSC 404 C Pegasus, was used. The DSC measures the temperature difference between two crucibles. For one DSC experiment, a total of three measurements were performed: One with two empty crucibles to determine the baseline, a run with one empty crucible and a reference material in the other, and finally a run with one empty crucible and the sample material. As a result of the specific heat capacity of the material (reference or sample), there is a temperature gradient between the empty crucible and the filled one, when heating up both equally. By measuring the temperature gradient for a reference material with a known specific heat capacity, it is possible to determine the specific heat capacity of the sample under test. Ideally, the temperature difference between two empty crucibles would be zero. However, due to minor imperfections in the alignment of the measuring system and unequal masses of the crucibles this is not exactly true. Thus, it is necessary to measure the baseline and subtract it from both the reference measurements, as well as the sample measurement. The specific heat capacity $c_{p,S}$ of the sample was determined by the equation

$$c_{p,S}(T) = c_{p,R}(T) \cdot \frac{m_R}{m_S} \frac{\phi_S - \phi_B}{\phi_R - \phi_B}, \tag{10}$$

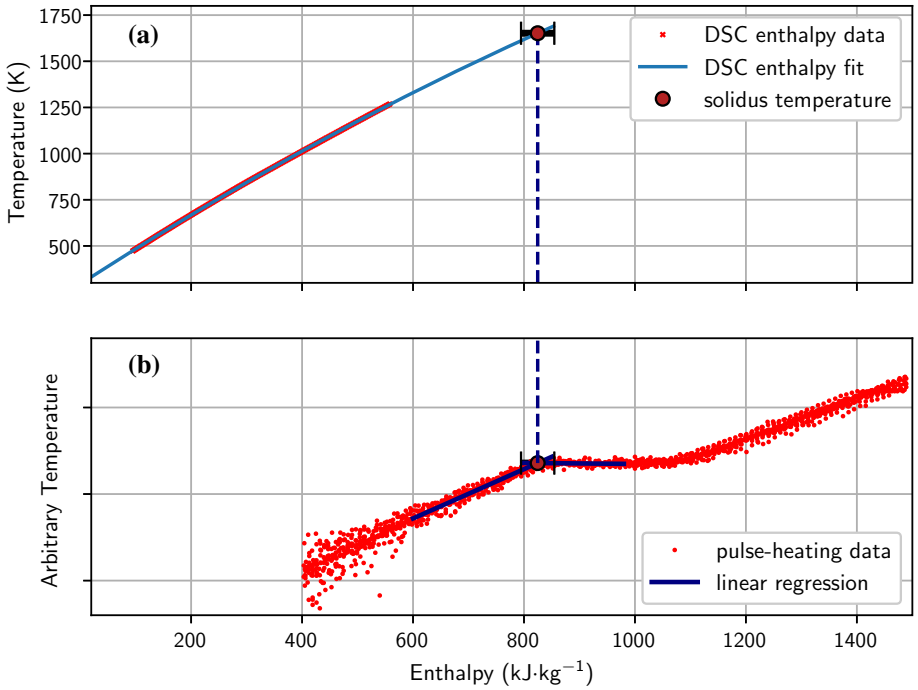

Figure 4 Method to obtain solidus temperature by matching enthalpy of pulse-heating data to enthalpy of DSC measurements. **a** Shows the temperature as a function of enthalpy from DSC measurements, which has been fit and extrapolated. **b** Shows the pyrometer signal as a function of enthalpy from pulse-heating measurements. The onset of the melting plateau has been determined by linearly fitting the plateau as well as the rising pyrometer signal before the plateau. The intersection of those fits yields the onset of the melting plateau. The corresponding temperature to this enthalpy value was then determined by extrapolating DSC enthalpy data.

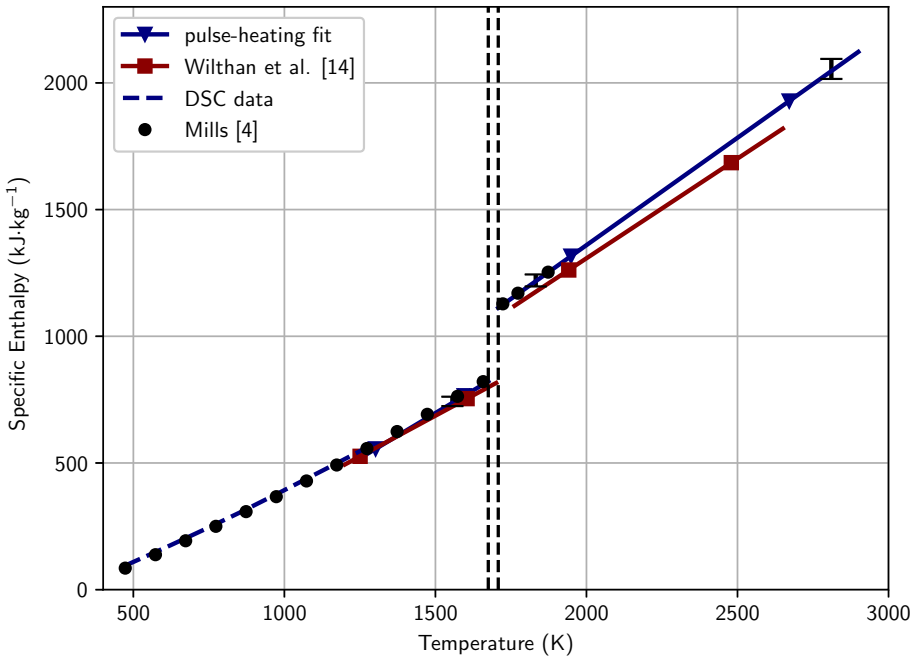

Figure 5 Specific enthalpy as a function of temperature. The reference temperature for enthalpy measurements is room temperature (298 K). The results of this work are compared to measurements by Wilthan et al. [14], who measured a similar AISI 316L stainless steel as well as to the recommended values by Mills [4], who also presents values for a different, but similar AISI 316L stainless steel. The horizontal dashed lines give solidus and liquidus temperatures.

Table 3 Polynomial fit coefficients for the thermophysical properties according to $y = a + bT + cT^2$

Property y	Unit	a	b	c	Range T/K	State	Method
$D(T)$	$\mathrm{kg\,m^{-3}}$	8052	− 0.564		$500 \leq T \leq T_s$	s	OPA
$D(T)$	$\mathrm{kg\,m^{-3}}$	8065	− 0.661		$T_l \leq T \leq 2900$	l	OPA
$\rho_{IG}(T)$	μΩm	0.624	7.951×10^{-4}	-2.61×10^{-7}	$500 \leq T \leq 1250$	s	DSC + OPA
$\rho_{IG}(T)$	μΩm	1.026	1.477×10^{-4}		$1350 \leq T \leq T_s$	s	OPA
$\rho_{IG}(T)$	μΩm	1.263	2.021×10^{-5}		$T_l \leq T \leq 2900$	l	OPA
$\rho_{corr}(T)$	μΩm	0.977	2.605×10^{-4}		$1350 \leq T \leq T_s$	s	OPA
$\rho_{corr}(T)$	μΩm	1.154	1.893×10^{-4}		$T_l \leq T \leq 2900$	l	OPA
$H_s(T)$	$\mathrm{kJ\,kg^{-1}}$	− 139	0.459	7.16×10^{-5}	$500 \leq T \leq 1250$	s	DSC
$H_s(T)$	$\mathrm{kJ\,kg^{-1}}$	− 374	0.714		$1350 \leq T \leq T_s$	s	OPA
$H_s(T)$	$\mathrm{kJ\,kg^{-1}}$	− 335	0.847		$T_l \leq T \leq 2900$	l	OPA

$T_s = 1675\,\mathrm{K}$, $T_l = 1708\,\mathrm{K}$, are the solidus and liquidus temperatures, respectively. D is the density, ρ_{IG} is the electrical resistivity assuming initial geometry, ρ_{corr} is the electrical resistivity corrected for thermal expansion, H_s is the specific enthalpy, and T is the temperature. S and l denote data in solid and liquid phase

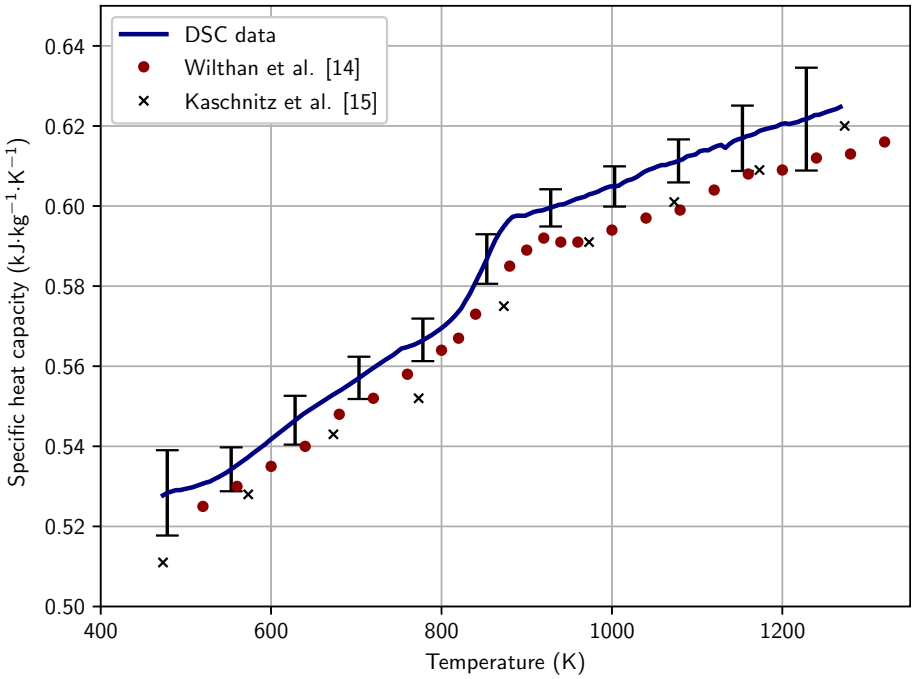

Figure 6 Specific heat capacity obtained via DSC measurements. The solid blue curve represents this work. The red circles represent measurements of a AISI 316L stainless steel, by Wilthan et al. [14]. The black crosses represent measurements of a similar AISI 316L stainless steel by Kaschnitz et al. [15].

with T the temperature, $c_{p,R}(T)$ the specific heat capacity of the reference material, m_R the mass of the reference, m_S the mass of the sample, and ϕ_i the DSC signals (i = R,S,B; R stands for reference, S for sample, and B for baseline).

The temperature range of the DSC measurements starts at 473 K. Enthalpy can be calculated from $c_{p,S}$ by integrating heat capacity with respect to temperature:

$$H(T) = \int_{473\,\mathrm{K}}^{T} c_{p,S}(T')\mathrm{d}T' + (473\,\mathrm{K} - 298\,\mathrm{K}) \cdot c_{p,S}(473\,\mathrm{K}). \tag{11}$$

By obtaining enthalpy as a function of temperature, $H(T)$, it is then possible to determine the inverse: Temperature as a function of enthalpy $T(H)$. As enthalpy data obtained by OPA measurements start from room temperature, these data can be matched with the enthalpy data obtained from DSC

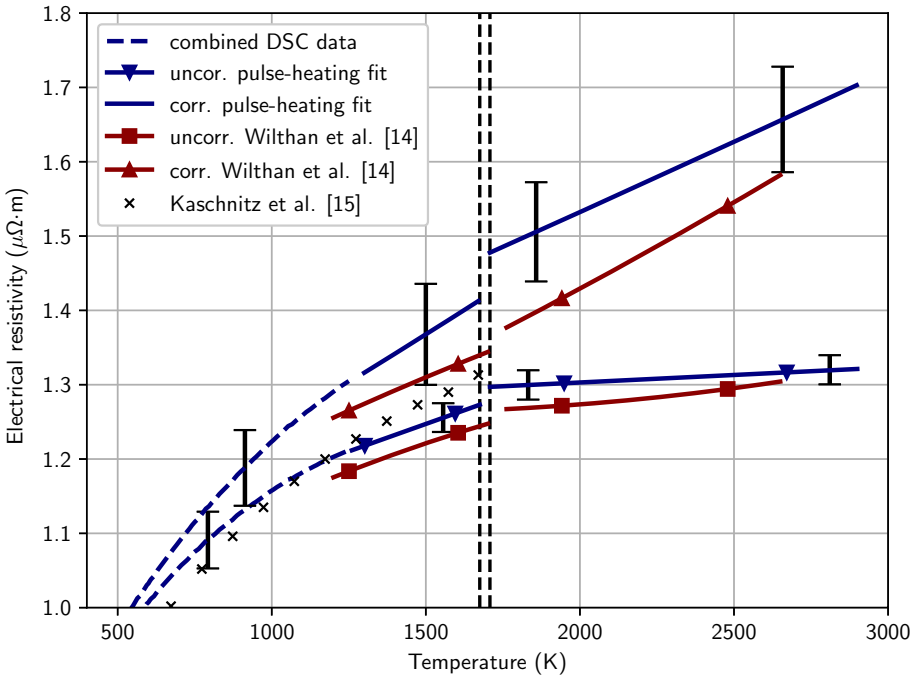

Figure 7 Electrical resistivity as a function of temperature. The solid blue line with triangle-shaped markers represents this work, assuming the initial geometry of the sample. The solid blue line represents this work's resistivity values corrected for thermal expansion. The red lines represent measurements of a AISI 316L stainless steel by Wilthan et al. [14]. The black crosses represent measurements of a similar AISI 316L stainless steel by Kaschnitz et al. [15].

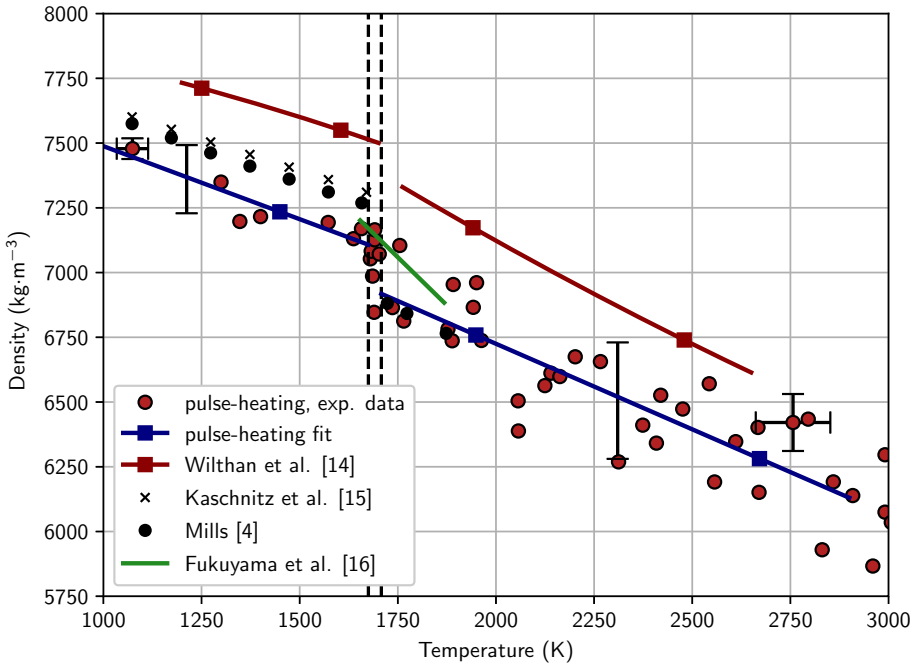

Figure 8 Density as a function of temperature. The red circles are the measured data, and the solid blue lines are linear fits. Black circles represent the recommended values of a similar steel by Mills [4]. The solid red lines are data for a AISI 316L stainless steel measured by Wilthan et al. [14]. The black crosses represent data of a similar AISI 316L stainless steel measured by Kaschnitz et al. [15]. The solid green line without markers represents data of a similar AISI 316L stainless steel measured by Fukuyama et al. [16].

measurements to assign a temperature to the enthalpy data from OPA measurements. This is presented graphically in Fig. 3.

To determine the density at room temperature, cylinders with a diameter of $d = (10.98 \pm 0.01) \times 10^{-3}$m and a height of $h = (5.19 \pm 0.01) \times 10^{-3}$m were machined. The mass of the cylinder was measured with a Mettler Toledo PB303 balance as $m = (3.883 \pm 0.001) \times 10^{-3}$kg, yielding a room temperature density of $(7904 \pm 25)\,\mathrm{kg\,m^{-3}}$.

Results

Solidus (T_s) and liquidus (T_l) temperatures of the material were determined by DSC measurements and are presented in Table 2. Due to evaporation of the

Table 4 Assessed uncertainties of the measured thermophysical properties

Property y	Unit	Uncertainty (%)	State	Method
$D(T)$	$\mathrm{kg\,m^{-3}}$	2.5	Solid	OPA
$D(T)$	$\mathrm{kg\,m^{-3}}$	3	Liquid	OPA
$\rho_{\mathrm{IG}}(T)$	$\mu\Omega\,\mathrm{m}$	3	Solid	DSC + OPA
$\rho_{\mathrm{IG}}(T)$	$\mu\Omega\,\mathrm{m}$	2.5	Solid	OPA
$\rho_{\mathrm{IG}}(T)$	$\mu\Omega\,\mathrm{m}$	2.5	Liquid	OPA
$\rho_{\mathrm{corr}}(T)$	$\mu\Omega\,\mathrm{m}$	5	Solid	OPA + DSC
$\rho_{\mathrm{corr}}(T)$	$\mu\Omega\,\mathrm{m}$	5.5	Solid	OPA
$\rho_{\mathrm{corr}}(T)$	$\mu\Omega\,\mathrm{m}$	4.5	Liquid	OPA
$H_s(T)$	$\mathrm{kJ\,kg^{-1}}$	2.5	Solid	OPA
$H_s(T)$	$\mathrm{kJ\,kg^{-1}}$	2.9	Liquid	OPA
$c_{\mathrm{p}}(T)$*	$\mathrm{kJ\,kg^{-1}K^{-1}}$	1.8–3	Solid	DSC

If not indicated with an asterisk, all uncertainty values are calculated according to the GUM with a coverage factor $k = 2$. Asterisk: uncertainty value assessed statistically

material in the melt phase during DSC measurements, the onset of the melting peak in the DSC signal provides an upper limit of the solidus temperature. By repeated heating of a sample in the DSC, it was found that the onset of the melting peak was shifted to higher temperatures compared to the first heating. Manganese, which has a very high vapor pressure, evaporates from the material during the initial heating, altering the solidus temperature by approx. 20 K. Therefore, the solidus temperature was determined by taking the mean of the onset of the melting peak from the DSC measurements and a temperature found by matching the enthalpy of the OPA data to the extrapolated enthalpy of the DSC measurements (see Fig. 4).

The higher uncertainty of the liquidus temperature is due to the strong evaporation of manganese and chromium at melting. Therefore, as the composition of the material changes during melting, the liquidus temperature determined by identifying the endothermal peak in the DSC heating curve is not the true liquidus temperature of the initial material. Note: Samples used in the DSC were not reused for subsequent OPA measurements.

The specific enthalpy $H_{298}(T) = H_{\mathrm{s}}(T) - H(298\,\mathrm{K})$ as a function of temperature T is shown in Fig. 5. The fitting coefficients are given in Table 3. The horizontal dashed lines in Fig. 5 represent the beginning and end of the melting. The difference in enthalpy between the ending of the solid phase ($H_{298,1} = 822\,\mathrm{kJ\,kg^{-1}}$) and beginning of the liquid phase ($H_{298,2} = 1112\,\mathrm{kJ\,kg^{-1}}$) gives the latent heat of fusion $\Delta H = 290\,\mathrm{kJ\,kg^{-1}}$.

In the liquid phase and at the end of the solid phase, specific heat capacity c_{p} is represented by the slope of $H_{298}(T)$, yielding $c_{\mathrm{p}} = 0.847\,\mathrm{kJ\,kg^{-1}\,K^{-1}}$ for the liquid phase (1708 K to 2900 K) and $c_{\mathrm{p}} = 0.714\,\mathrm{kJ\,kg^{-1}\,K^{-1}}$ for the end of the solid phase. Furthermore, the specific heat capacity in the solid phase has been measured with DSC with the results given in Fig. 6 and in Table 7. DSC-measured specific heat capacity ranges from 500 K to 1250 K. There is a slight kink in the data at 820 K, which most likely results from precipitates dissolving in the material.

Figure 7 shows the results for electrical resistivity as a function of temperature both with and without correction for the change of volume due to thermal expansion. The solid blue line with triangle-shaped

Table 5 Composition of the AISI 316L stainless steels compared in mass %

References	Fe	Cr	Ni	Mo	Mn	Si	C
SRM	bal.	17.803	12.471	2.188	1.593	0.521	0.026
Wilthan et al. [14]	bal.	17.50	14.50	2.70	1.70	0.30	0.030
Kaschnitz et al. [15]	bal.	16.7	10.1	2.0	1.63	0.41	0.03
Mills [4]	bal.	17	12	2.5	2	1	0.08
Fukuyama et al. [16]	bal.	17.3	12.0	2.23	1.61	0.53	0.015

Table 6 Collected thermophysical data of this work

T/K	H_S/kJ kg^{-1}	ρ_{IG}/μΩ m	ρ_{corr}/μΩ m	$D(T)$/kg m^{-3}	$\frac{V(T)}{V_0}$/1
500	109	0.954	0.970	7770	1.017
600	163	1.007	1.033	7714	1.025
700	218	1.054	1.089	7657	1.033
800	274	1.093	1.138	7601	1.041
900	333	1.128	1.183	7544	1.049
1000	393	1.157	1.223	7488	1.057
1100	454	1.182	1.259	7432	1.065
1200	515	1.203	1.290	7375	1.073
1300	554	1.218	1.316	7319	1.081
1400	626	1.232	1.342	7263	1.089
1500	697	1.247	1.368	7206	1.097
1600	769	1.262	1.394	7150	1.105
1700	1042	1.291	1.464	6964	1.132
1800	1190	1.299	1.495	6857	1.151
1900	1275	1.301	1.514	6791	1.163
2000	1360	1.303	1.532	6725	1.176
2100	1444	1.305	1.551	6659	1.189
2200	1529	1.307	1.570	6593	1.201
2300	1614	1.309	1.589	6527	1.214
2400	1699	1.311	1.608	6461	1.226
2500	1783	1.313	1.627	6395	1.239
2600	1868	1.315	1.646	6329	1.251
2700	1953	1.317	1.665	6262	1.264
2800	2037	1.319	1.684	6196	1.277

D is the density, ρ_{IG} is the electrical resistivity, assuming initial geometry, ρ_{corr} is the electrical resistivity, corrected for thermal expansion, H_s is the specific enthalpy, $\frac{V(T)}{V_0}$ is the thermal expansion, and T is the temperature

markers represents the linear fits of the pulse-heating data using the initial sample geometry. The solid blue lines without markers are the linear fit of the pulse-heating data corrected for volume expansion. The dashed blue lines represent the fitted pulse-heating data with matched temperatures from DSC measurements. The uncorrected resistivity is represented by the lower line; the corrected resistivity is represented by the upper line. The coefficients for the polynomial fits are given in Table 3.

Density as a function of temperature is presented in Fig. 8. The red circles are actual measurement points with the solid blue lines the linear fits. The coefficients and their respective temperature ranges are given in Table 3.

Uncertainties

The uncertainties of the DSC measurements were assessed statistically. Other uncertainties were calculated according to the Guide to the Expression of Uncertainty in Measurement (GUM) [17]. Uncertainties of the fitting coefficients were calculated following the guide by Matus [18]. Uncertainty values are listed in Table 4.

Uncertainty values for the temperature-dependent density were assessed by evaluating the radii of the hot and cold wire 10 times to obtain a statistical uncertainty. As this only accounts for uncertainty in evaluation, the standard deviation of the obtained radii was then doubled.

Conclusion

Thermophysical properties of NIST SRM for 316L stainless steel (1155a), a Cr18–Ni12–Mo2 steel, were measured by means of ohmic pulse heating in combination with a differential scanning calorimeter (DSC). These properties include specific heat capacity, specific enthalpy, corrected and uncorrected electrical resistivity, as well as density, all as a function of temperature. Our results were compared to

Table 7 Specific heat capacity c_p as a function of temperature T determined via DSC

T K	c_p kJ kg^{-1} K^{-1}	$\Delta(c_p)$ kJ kg^{-1} K^{-1}	T K	c_p kJ kg^{-1} K^{-1}	$\Delta(c_p)$ kJ kg^{-1} K^{-1}
473	0.528	0.011	873	0.595	0.005
493	0.529	0.009	893	0.598	0.005
513	0.530	0.007	913	0.599	0.005
533	0.532	0.006	933	0.600	0.005
553	0.534	0.005	953	0.601	0.004
573	0.537	0.006	973	0.603	0.004
593	0.541	0.006	993	0.605	0.005
613	0.544	0.006	1013	0.606	0.005
633	0.547	0.006	1033	0.608	0.005
653	0.550	0.006	1053	0.610	0.005
673	0.553	0.006	1073	0.611	0.005
693	0.556	0.005	1093	0.613	0.006
713	0.559	0.005	1113	0.614	0.006
733	0.561	0.005	1133	0.615	0.006
753	0.564	0.005	1153	0.617	0.008
773	0.566	0.005	1173	0.619	0.009
793	0.569	0.006	1193	0.620	0.010
813	0.572	0.006	1213	0.621	0.012
833	0.578	0.007	1233	0.622	0.013
853	0.587	0.006	1253	0.624	0.015

Δc_p denotes the $k = 2$ uncertainty

the literature values of similar steels, as there are no data available in the literature for this exact SRM. Enthalpy and uncorrected resistivity are in good agreement to the literature. Specific heat capacity in the liquid phase obtained in our work is 7% higher than reported by Wilthan et al. [14] and 8.5% higher than reported by Fukuyama et al. [16]. The value for specific heat capacity in the liquid phase reported by Mills [4] is 2% lower than the obtained value of this work. Density in the liquid phase is in good agreement to the values reported by Mills [4]. Our density data are 5% lower, compared to the data reported by Wilthan et al. [14]. The density is indirectly proportional to the thermal volume expansion of the material (see (9)). Therefore, electrical resistivity, corrected for thermal expansion, is 5% higher, compared to the values reported by Wilthan et al. [14]. However, it has to be noted that the composition of the AISI 316L steels reported in the literature differs from the composition of the NIST SRM 1155a. The exact compositions of the samples are shown in Table 5. The literature data are reported as comparison values only. Uncertainty assessment was performed according to the GUM. Thermophysical property data obtained in this work are listed in Tables 6 and 7. Coefficients for all fits are given in Table 3. Results of the uncertainty assessment are listed in Table 4.

Acknowledgements

Open access funding provided by Graz University of Technology. The authors thank Anna Vaskuri, Boris Wilthan, and Matthias Leitner for their comments and careful reading of this manuscript.

Compliance with ethical standards

Conflicts of interest The authors declare that there is no conflict of interest.

References

[1] Simonds BJ, Sowards J, Hadler J, Pfeif E, Wilthan B, Tanner J, Harris C, Williams P et al (2018) Time-resolved absorptance and melt pool dynamics during intense laser irradiation of a metal. Phys Rev Appl 10(4):044061. https://doi.org/10.1103/PhysRevApplied.10.044061

[2] Jenkins R, Westover R (1962) Thermal diffusivity of stainless steel from 20° to 1000° C. J Chem Eng Data 7(3):434–437. https://doi.org/10.1021/je60014a038

[3] Lucks C, Deem H (1958) Thermal properties of 13 metals: thermal properties of 13 metals. ASTM 9:795–795. https://doi.org/10.1002/maco.19580091216

[4] Mills K (2002) Recommended values of thermophysical properties for selected commercial alloys. Woodhead Publishing, Sswston

[5] Specification for Chromium and Chromium-Nickel Stainless Steel Plate, Sheet, and Strip for Pressure Vessels and for General Applications. https://doi.org/10.1520/a0240_a0240m-17

[6] Mills K, Su Y, Li Z, Brooks R (2004) Equations for the calculation of the thermo-physical properties of stainless steel. ISIJ Int 44(10):1661–1668. https://doi.org/10.2355/isijinternational.44.1661

[7] Lippold L (1994) Solidification behavior and cracking susceptibility of pulsed-laser welds in austenitic stainless steels. Weld J 73(6):129–139

[8] SRM 1155a (2013) AISI 316 Stainless Steel. National Institute of Standards and Technology; U.S. Department of Commerce, Gaithersburg, MD

[9] Kaschnitz E, Pottlacher G, Jaeger H (1992) A new microsecond pulse-heating system to investigate thermophysical properties of solid and liquid metals. Int J Thermophys 13(4):699–710. https://doi.org/10.1007/bf00501950

[10] Leitner M, Leitner T, Schmon A, Aziz K, Pottlacher G (2017) Thermophysical properties of liquid aluminum. Metall Mater Trans A 48:3036–3045. https://doi.org/10.1007/s11661-017-4053-6

[11] Pearson Electronics I (2019) Pearson current monitor model 3025. http://www.pearsonelectronics.com/pdf/3025.pdf. Accessed 05 Apr

[12] Huepf T (2010) Density determination of liquid metals: Ph.D. thesis, Graz University of Technology

[13] Leitner M, Schroer W, Pottlacher G (2018) Density of liquid tantalum and estimation of critical point data. Int J Thermophys 39(11):124. https://doi.org/10.1007/s10765-018-2439-3

[14] Wilthan B, Reschab H, Tanzer R, Schuetzenhoefer W, Pottlacher G (2008) Thermophysical properties of a chromium–nickel–molybdenum steel in the solid and liquid phases. Int J Thermophys 29(1):434–444. https://doi.org/10.1007/s10765-007-0300-1

[15] Kaschnitz E, Kaschnitz H, Schleutker T, Guelhan A Bonvoisin B (2017) Electrical resistivity measured by millisecond pulse-heating in comparison to thermal conductivity of the stainless steel AISI 316L at elevated temperature. High Temp High Press 46

[16] Fukuyama H, Higashi H, Yamano H (2019) Thermophysical properties of molten stainless steel containing 5 mass% B4C. Nucl Technol 0(0):1–10. https://doi.org/10.1080/00295450.2019.1578572

[17] Joint Committee for Guides in Metrology (JCGM/WG 1), WG (ed) (1993) Guide to the expression of uncertainty in measurement: BIPM

[18] Matus M (2005) Koeffizienten und Ausgleichsrechnung: Die Messunsicherheit nach GUM. Teil 1: Ausgleichsgeraden (Coefficients and adjustment calculations: measurement uncertainty under GUM. Part 1: best fit straight lines): tm—Technisches Messen 72(10/2005). https://doi.org/10.1524/teme.2005.72.10_2005.584

8.2. Thermal Conductivity of Liquid Metals

SHORT SUMMARY A variety of experimental methods to obtain thermal conductivity λ from the literature is compared and explained. The methods are explained and their uncertainties are listed.

REMARKS ON AUTHORSHIP

P. Pichler conducted a literature search and wrote the majority of the publication.
G. Pottlacher conducted a literature search and wrote chapter "Abstract". He supervised the publication process.

Chapter 5

Thermal Conductivity of Liquid Metals

Peter Pichler and Gernot Pottlacher

Additional information is available at the end of the chapter

http://dx.doi.org/10.5772/intechopen.75431

Abstract

Over the last decades, many experimental methods have been developed and improved to measure thermophysical properties of matter. This chapter gives an overview over the most common techniques to obtain thermal conductivity λ as a function of temperature T. These methods can be divided into steady state and transient methods. At the Institute of Experimental Physics at Graz University of Technology, an ohmic pulse-heating apparatus was installed in the 1980s, and has been further improved over the years, which allows the investigation of thermal conductivity and thermal diffusivity for the end of the solid phase and especially for the liquid phase of metals and alloys. This apparatus will be described in more detail. To determine thermal conductivity and thermal diffusivity with the ohmic pulse-heating method, the Wiedemann-Franz law is used. There are electronic as well as lattice contributions to thermal conductivity. As the materials examined at Graz University of Technology, are mostly in the liquid phase, the lattice contribution to thermal conductivity is negligibly small in most cases. Uncertainties for thermal conductivity for aluminum have been estimated ±6% in the solid phase and ±5% in the liquid phase.

Keywords: thermal conductivity, ohmic pulse-heating, Wiedemann-Franz law, sub-second physics, high temperature, liquid phase

1. Introduction

Knowing thermophysical properties, i.e., properties that are influenced by temperature, of metals and alloys is not only of academic interest, but also profoundly important for industry and commerce. Casting of metal objects, made of, e.g., steel or aluminum, is prone to casting defects and imperfections. Therefore, in the majority of modern production procedures, computer simulations are performed to reduce defects and imperfections as well as generally

optimize manufacturing processes. The driven benefits from such simulations often are limited by an insufficient or lacking access to experimentally obtained data. It is especially the liquid phase of metals and alloys, that is of interest, as such production processes like, e.g., casting, naturally take place in the liquid phase.

The term thermophysical properties include various properties: thermal conductivity, thermal diffusivity, thermal volume expansion, heat capacity, density, viscosity and so on. Many of those properties are important in industrial processes; however, it is thermal conductivity, more precisely, thermal conductivity of liquid metals and alloys that will be discussed in this chapter.

Naturally, the numbers of experimental methods to measure the desired quantities that have been developed over the past decades are manifold. It is the goal of this work to give a brief overview of the most common or practical techniques in Section 2, but only few of these methods are suitable to conduct measurements in the liquid phase. These techniques will be highlighted in Section 2.

At the Thermo- and Metalphysics group at Graz University of Technology, fast pulse-heating experiments are performed to measure thermophysical properties of liquid metals and alloys. The Wiedemann-Franz law is applied to calculate thermal diffusivity and thermal conductivity from measured quantities. These mentioned calculations are briefly explained in Section 3, and the experimental apparatus used is described in Section 4.

2. An overview of methods to measure thermal conductivity of liquid metals

In principle, there are three different classes of measurement methods:

- Steady state methods
- Non-steady state methods
- Transient methods

However, it is not always as easy to classify a certain technique. Especially, distinguishing between non-steady state methods and transient methods can be challenging.

Steady state methods are defined as techniques, where the temperature gradient remains constant across the sample. Those methods require precise temperature control throughout the whole experiment to confine convection effects to a minimum, which is especially hard to achieve for metals with high melting points.

Transient methods and non-steady state methods make use of very short time frames in order to conclude measurements before convection plays a role. Non-steady state methods achieve those conditions due to very high heating rates of up to 1000 Ks^{-1}, with rather large temperature gradients of over 100 K.

The temperature gradient in transient methods is significantly lower (on the order of 5 K) than in non-steady state methods, which minimizes the possibility of convection-induced effects in the measurements. In recent history transient methods grew in importance and started to replace non-steady state methods.

2.1. Steady state methods

2.1.1. Axial heat flow method

A known heat flux q is applied to one end of a sample and dissipated on the other end by a heat sink. Thermal conductivity can be calculated by

$$\lambda = \frac{q}{A} \cdot \frac{\Delta z}{\Delta T} \tag{1}$$

where q is the applied heat flux, A is the specimen cross-section, and $\frac{\Delta z}{\Delta T}$ is the inverse temperature gradient across two points z_q and z_2.

Therefore, the conditions to determine thermal conductivity with this method is the determination of the geometry A and Δz, guarantee that the heat flow is unidirectional, measurement of the heat flux q, and measurement of temperature of at least two points z_q and z_2 (normally thermocouples).

While this technique is mostly targeted at solid materials, it can be used on a variety of liquid metals with low melting points such as mercury, lead, indium, and gallium [1].

The temperature range is 90–1300 K, and the accuracy in this range has been estimated to be ±0.5 to ±2% [2].

2.1.2. Radial heat flow method

Another method to measure thermal conductivity for both solid and liquid materials is the concentric cylinder method.

The solid sample is placed in-between two concentric cylinders, and a known heat flux is applied by leading a heater through the inner cylinder. The outer cylinder is water cooled to provide a temperature gradient between the two cylinders.

The temperature difference between temperature sensors (often thermocouples) in the two cylinders is determined when steady state is achieved. Knowing the radii of the two cylinders and their length, thermal conductivity can be calculated by

$$\lambda = \frac{q}{L} \cdot \frac{\ln\left(\frac{r_2}{r_1}\right)}{2 \cdot \pi \cdot \left(\mathrm{T}_1 - \mathrm{T}_2\right)} \tag{2}$$

with q being the applied heat flux, L as the length of the cylinders, r_1 as radius of the inner cylinder, r_2 as radius of the outer cylinder, and T_1 and T_2 as the respective temperatures.

A more in-depth explanation of this method can be found in [2].

The method can be adapted for liquid metals by providing a container for the liquid sample in-between the two concentric cylinders. Apart from this container, the measuring principle remains the same for liquid metal samples.

The radial heat flow method operates in a temperature range of 4–1000 K and the uncertainty of this method has been estimated to be about ±2% [3].

2.2. Direct heating methods

The term "direct electrical heating method" summarizes all those measurement techniques, where the sample is heated up, by running a current through it, without an additional furnace. An example of such a method, but in a dynamic way and not as a steady state method, is the ohmic pulse-heating method that will be discussed later in this chapter.

Direct electrical heating methods are therefore limited to samples which are decent electrical conductors. The shape of the samples can vary from wires, rods, sheets to tubes. The advantage of such techniques is for one, the lack of a furnace and, secondly, the possibility to measure a multitude of thermophysical properties simultaneously.

Direct heating methods are able to achieve high temperatures of about 4000 K and are therefore suitable for measuring thermal conductivity in the liquid phase of metals with high melting points.

2.2.1. Guarded hot plate

This steady state method utilizes two temperature-controlled plates that sandwich a solid disc-shaped sample. Heating one plate, while cooling the other one, generates a uniformly distributed heat flux through the sample, achieving a steady state temperature at each plate. The technique is considered as the steady state method with the highest accuracy.

The guarded hot plate apparatus can be constructed in single sided or double sided mode. When operated in double sided mode, there is a total amount of three plates as well as two samples: A central heater plate together with two cooling plates sandwiching the two samples. The temperature drop across the two specimens is measured with thermocouples, which are apart a distance L. Thermal conductivity can then be determined by

$$\lambda = \frac{q \cdot L}{2 \cdot A \cdot \Delta T} \tag{3}$$

where q is the heat flux through the specimen, A is the cross section, L is the spatial distance between the two thermocouples, and ΔT is the temperature difference.

In the single-sided mode, one of the cooling plates as well as the second specimen is removed. The temperature gradient in one direction therefore vanishes, which leads to the loss of a factor 2 in Eq. (3)

http://dx.doi.org/10.5772/intechopen.75431

$$\lambda = \frac{q \cdot L}{A \cdot \Delta T} \tag{4}$$

The experimental setup and the calculation of the thermal conductivity are more thoroughly explained in [4].

Commercially available guarded hot plate (GHP) apparatus, like the NETZSCH GHP 456 Titan [5], operate in a temperature range of 110–520 K and provide an accuracy of ±2%.

It has to be noted that the GHP method is applicable only for solid samples and it is not a suitable method to determine thermal conductivity of high-melting metals.

2.2.2. Calorimeter method

The calorimeter technique is a direct measurement of Fourier's law. It consists of a heating source (typically SiC or $MoSi_2$ elements) and a SiC slab to distribute the temperature gradient. The specimen is enclosed by two insulating guard bricks, which are, like the specimen as well, in thermal contact with a water-cooled copper base. As the name gives away, the central part of the system is a calorimeter, which is surrounded by the guards. The apparatus is designed in a way that the heat flow into the calorimeter is one-dimensional.

Two thermocouples, which are apart a distance L and lie vertically to each other, are enclosed in the specimen and the temperature difference $T_2 - T_1$ between them is measured.

Thermal conductivity can be determined by

$$\lambda = \frac{\frac{dq}{dt} \cdot L}{A(T_2 - T_1)} \tag{5}$$

with A being the cross section of the calorimeter, L as the distance between the two thermocouples, $\frac{dq}{dt}$ as the rate of heat flow into the calorimeter, and $T_2 - T_1$ as the temperature difference between the two thermocouples.

2.3. Transient methods

2.3.1. Transient hot wire and transient hot strip method

Simple experimental arrangements and short measurement times are granted by the transient hot wire (THW) along with the transient hot strip (THS) method.

The transient hot wire technique is most commonly used for measuring thermal conductivity λ and thermal diffusivity a. An electrically heated wire, which acts as a self-heated thermometer is placed into a material and distributes a radial heat flow into the sample. The specimen itself acts as a heat sink for the system, while the wire functions as a heat source as well as providing a mechanism to measure the thermal transport properties, due to a temperature-dependent drop of the voltage along the wire. Solving the fundamental heat conduction equation yields

$$\Delta T(r, t) = \frac{q}{4 \cdot \pi \cdot \lambda} \cdot \ln\left(\frac{4 \cdot a \cdot t}{r^2 \cdot e^{\gamma}}\right), \tag{6}$$

with q the heat input per unit length of the wire, r the radius of the wire, a the thermal diffusivity, γ Euler's constant, t the time, and λ, of course, the thermal conductivity.

An in-depth explanation of this method to determine thermal conductivity is given in [6, 7].

The transient hot strip (THS) method further improves the THW method. Instead of a wire as the heat source and measuring device, a thin strip of metal foil is used. The metal foil provides a greater surface as well as a smaller thickness than the heated wire, leading to a lower density of heat flow and consequently, a smaller thermal contact resistance to the sample.

While the THW method is only applicable for liquids and some solids, which can be wrapped around the heating wire in a way the thermal resistance is low enough, the THS method is the go-to method to perform measurements on solids.

Note: this work focuses on the measurement techniques for thermal conductivity of liquids. THS measurements are also performed on gases (see [8]).

At Physikalisch-Technische Bundesanstalt (PTB), Braunschweig, an upgraded version of the THS and THW method, the transient hot bridge technique, has been developed. In this method, a total of eight strips are deployed in a way they form a Wheatstone bridge, allowing an effective thermal and electrical self-compensation [9].

Uncertainties of the THW technique have been reported (e.g., see [10]) to be ±5.8% for the determination of thermal conductivity. However, the method has also be described as even more accurate [11], with uncertainties of below ±1% for gases, liquids, and solids. With a maximum temperature of about 1000 K, this method is only suitable for low melting metals.

2.3.2. 3ω method

The 3ω method goes back to the work done by Cahill [12] in 1987. The method has similarities with the THS and THW technique, since it also uses a single element as heat source as well as thermometer. While both the THS and THW method measure temperature in dependence of time, the 3ω technique records the amplitude and phase of the resistance depending on the frequency of the excitation.

It is most commonly used as a technique to measure thermal conductivity of solids or liquids, but has been improved to also be applicable on thin films [12, 13]. A conducting wire is distributed onto a specimen and an AC voltage with a frequency ω is driven through it. Due to the electrical resistance, the sample is heated up, resulting in a temperature change. The frequency of the change in temperature is 2ω. The product of the resistance oscillation 2ω and the excitation frequency ω gives a voltage of frequency 3ω, which is measured and responsible for the name 3ω method.

Measuring the 3ω voltage at two frequencies f_1 and f_2, thermal conductivity is

$$\lambda = \frac{V^3 \ln f_2/f_1}{4 \cdot \pi \cdot l \cdot R^2 (V_{3,1} - V_{3,2})} \frac{dR}{dT} \tag{7}$$

with $V_{3,1}$ the 3ω voltage at frequency f_1, $V_{3,2}$ the 3ω voltage at frequency f_2, and R the average resistance of the metal line of length l.

In the original work of Cahill [13], the temperature range of the 3ω method is 30–750 K, which is not suitable for high melting metals. This method often is applied on nanofluids and publications state an uncertainty of around ±2% [14].

2.3.3. Laser flash method

Under the laser flash method (LFM), the directly measured quantity is thermal diffusivity and not thermal conductivity. Thermal conductivity can, however, be determined with knowledge of specific heat as well as density of the sample.

$$\lambda(T) = a(T) \cdot \rho(T) \cdot c_p(T), \tag{8}$$

with $a(T)$ the thermal diffusivity, $\rho(T)$ the density, and $c_p(T)$ the specific heat.

In the LFM, the sample is exposed to a high intensity laser pulse at one face, which generates heat at said surface. On the back surface, which is not exposed to the laser pulse, an infrared sensor detects a rising temperature signal, due to heat transfer through the sample.

For adiabatic conditions, thermal diffusivity can be obtained by

$$a = 0.1388 \frac{l^2}{t_{0.5}}, \tag{9}$$

with l the sample thickness and $t_{0.5}$ the time at 50% of the temperature increase.

LFM, as introduced by Parker et al. [15], has been a convenient technique to determine thermal diffusivity a and thermal conductivity λ of solids at moderate temperatures. The method has been further improved since then and is applicable for a great temperature range, up to around 2500°C.

In 1972, Schriempf [16] applied LFM to determine thermal diffusivity for liquid metals at high temperatures. The liquid metal has to be placed in a suitable container in order to arrange a proper setup. Problems arise for liquids of low thermal conductivity. When the thermal conductivity of the sample is of the same order as of the container, this leads to an unneglectable heat current through the container. Therefore, it was proposed in [17] not to insert the liquid sample into a container, but have it placed between a metal disc, which is exposed to the laser pulse.

Commercially available laser flash apparatus like the NETZSCH LFA 427 [18] operate in a temperature range from −120 to 2800°C, depending on the furnace and are therefore applicable for higher melting metals as well.

Kaschnitz [19] estimates uncertainties of thermal conductivity for LFM to be between ±3 and ±5% in the solid phase and ±8 to ±15% in the liquid phase.

Hay [20] did an uncertainty assessment for their apparatus at Bureau national de métrologie (BNM) and claimed uncertainty estimations from ±3 to ±5%.

Hohenauer [21] did an uncertainty assessment of their laser flash apparatus and stated an expanded uncertainty with thermal diffusivity measurement in the temperature range from 20 to 900°C of 3.98%.

3. Calculations via Wiedemann-Franz law

In some cases, it is more applicable to measure electrical conductivity respectively electrical resistivity. Heat transport and thus thermal conductivity through a metal or an alloy needs carriers. One has to distinguish between the component λ_e of thermal conductivity due to electrons and λ_l, which is the lattice contribution, due to phonons. Naturally for liquid metals and alloys, thermal conductivity is dominated by the electronic contribution. The total thermal conductivity would then be the sum of the components $\lambda = \lambda_e + \lambda_l$.

Thermal conductivity of liquid aluminum was examined at Graz University of Technology. Here the sole consideration of the electronic contribution gave promising results for the liquid phase [22]. A detailed derivation of the lattice-contribution to thermal conductivity can be found in the paper of Klemens [23].

An example when the lattice contribution has to be considered in the calculation of thermal conductivity for the Inconel 718 alloy is given in [24].

The Wiedemann-Franz law states that for conducting metals the electronic component of the thermal conductivity λ_e is

$$\lambda_e = L_0 \frac{T}{\rho(T)} \tag{10}$$

with $\rho(T)$ the temperature-dependent electrical resistivity and $L = \frac{\pi^2}{3} \cdot (k_B/e)^2 = 2.45 \times 10^{-8}\,\mathrm{W} \cdot \Omega \cdot \mathrm{K}^{-2}$ the (theoretical) Lorenz number.

Considering thermal expansion, the temperature-dependent electrical resistivity is

$$\rho(T) = \rho_{IG} \frac{d(T)^2}{d_0^2}, \tag{11}$$

with d_0 the diameter at reference temperature (room temperature), ρ_{IG} the electrical resistivity at initial geometry, and $d(T)$ the diameter at an elevated temperature T. To calculate thermal conductivity, it is therefore necessary to measure thermal volume expansion as well.

An estimation of thermal diffusivity $a(T)$ can be found by

http://dx.doi.org/10.5772/intechopen.75431

$$a(T) = \frac{L_0 \cdot T}{c_p(T) \cdot D(T) \cdot \rho(T)} \tag{12}$$

with $c_p(T)$ the heat-capacity and $D(T)$ the temperature-dependent density. With the ohmic pulse-heating setup at Graz University of Technology (as explained later in this work), radial over longitudinal expansion is ensured (see, e.g., [25]). Considering Eq. (12) and radial expansion yields

$$a(T) = \frac{L_0 \cdot T}{c_p(T) \cdot D(T) \cdot \rho(T)} = \frac{L_0 \cdot T}{c_p(T) \cdot D_0 \rho_{IG}} \tag{13}$$

with D_0 the density at room temperature.

Thus, Eqs. (10) and (12) enable us to determine thermal conductivity and thermal diffusivity from ohmic pulse-heating experiments, and deliver results that are in the same range as results from Laser flash measurements, as shown in the thermal diffusivity intercomparisons NPL – Report CBTLM S30 [26]. With a variation of only 3%, our results were significantly close to the average determined.

The experimental setup at Graz University of Technology is described in the following section.

4. Measurements at Graz University of Technology

In ohmic pulse-heating experiments, the electric conducting sample is heated up by passing a large current pulse through it. Due to the resistivity of the material, the sample is heated up from room temperature to the melting point and further up through the liquid phase to the boiling point in a period of about 50–70 μs.

The specimen typically is in the shape of a wire, with diameters ranging from a few hundred micrometers up to some millimeters, rectangular shape for materials that cannot be drawn into wires, foils or tubes. As a consequence of the narrow time frame under which these experiments are performed, the liquid phase does not collapse due to gravitational forces, enabling investigations of the entire liquid phase up to the boiling point. In addition, the specimen can be considered to not be in contact with the surrounding medium, rendering the experiment to being a container-less method.

4.1. Setup

A typical pulse heating experiment consists of the following parts: An energy storage (mostly a capacitor or battery bank) with a charging unit, a main switching unit (e.g., high-voltage mercury vapor ignition tubes) and an experimental chamber with windows for optical diagnostics and the ability to maintain a controlled ambient atmosphere. Pulse heating experiments are mostly performed under inert atmosphere, e.g., nitrogen or argon at ambient pressure,

or in vacuum. The setup of the pulse-heating apparatus at Graz University of Technology is presented in **Figure 1**.

The setup has been explained in detail in previous publications [27–29].

4.2. Current and voltage measurement

The current pulse, which the sample is subjected to, is measured using an induction coil (Pearson Electronics, Model Number 3025). To measure the voltage drop, two Molybdenum voltage-knives are attached to the specimen. The voltage drop relative to a common ground is measured for both of the voltage-knives, allowing the measurement of the voltage drop between the two contact points of the sample and the respective voltage-knives (**Figure 2**).

4.3. Temperature measurement

A fast pyrometer provides temperature determination. The pyrometer measures the spectral radiance of a sample surface from which the temperature can be calculated using Planck's law.

$$L_{\lambda,B}(\lambda, T) = \frac{c_1}{\pi \cdot \lambda^5} \cdot \frac{1}{e^{\frac{c_2}{\lambda \cdot T}} - 1}, \tag{14}$$

with $L_{\lambda,B}(\lambda, T)$ the radiance emitted by a black body at temperature T and wavelength λ and the two radiation constants $c_1 = 2\pi \cdot h \cdot c^2$ and $c_2 = \frac{h \cdot c}{k_B}$ (h is the Planck's constant, c the speed of light, and k_B the Boltzmann constant). It has to be considered that nearly no real material is a perfect black body. The deviation from black body radiation is taken into account by emissivity $\varepsilon(\lambda,T)$. The ratio of radiation emitted by a real material therefore is

$$L_\lambda(\lambda, T) = \varepsilon(\lambda, T) \cdot L_{\lambda,B}(\lambda, T). \tag{15}$$

It has to be noted as well that the measured quantity of the pyrometer is a voltage signal $U_{Pyro}(T)$, which is dependent on measuring geometry, transmission of the optical measuring setup, width of the spectral range and detector sensitivity. When summarizing the majority of the temperature-independent quantities in a constant C, the pyrometer signal is

$$U_{Pyro}(T) = C \cdot \varepsilon(\lambda, T) \cdot \left(e^{\frac{c_2}{\lambda \cdot T}} - 1\right)^{-1} \tag{16}$$

4.4. Thermal diffusivity and thermal conductivity

With the obtained values of the time-dependent current $I(t)$, the time-dependent voltage drop $U(t)$, the specimen radius $r(t)$ and the surface radiation $L(t)$ it is now possible to calculate the desired thermal properties, i.e., thermal conductivity $\lambda(T)$, thermal diffusivity $a(T)$ as well as specific heat capacity $c_p(T)$. This has been shown briefly in the second section of this chapter and is thoroughly discussed in [30, 31].

The solid phase as well as the liquid phase data are fitted linearly (for the solid phase) and quadratically (for the liquid phase). In our publications (e.g., [22]) we give the coefficients for the

http://dx.doi.org/10.5772/intechopen.75431

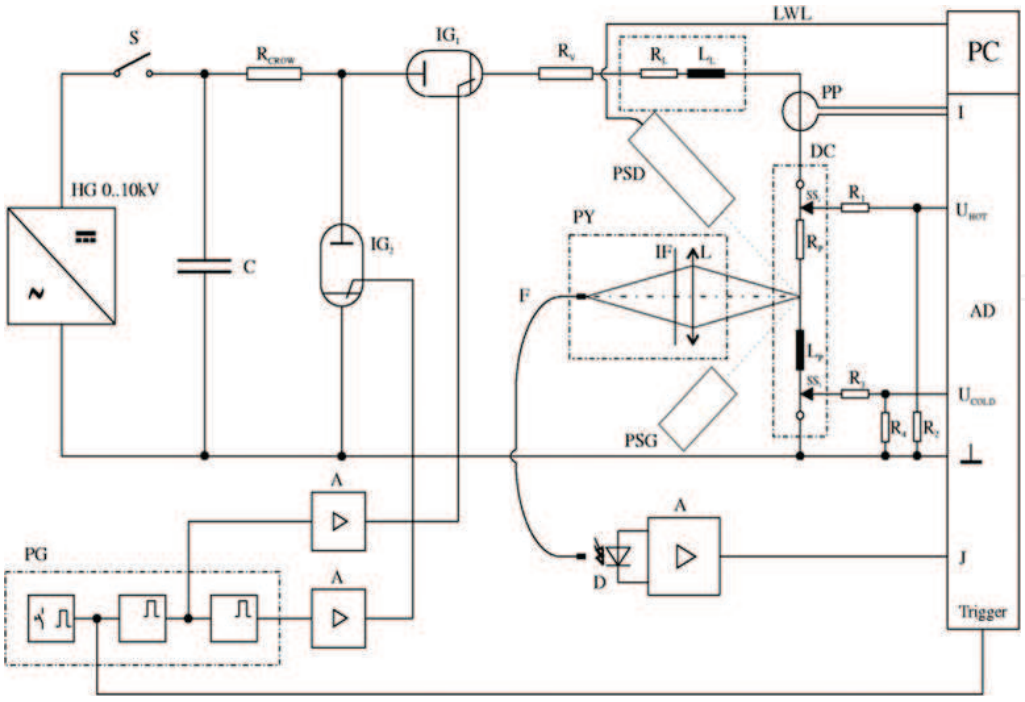

Figure 1. Schematic experimental setup. HG: high voltage power supply; S: switch for loading the capacitor bank C; R CROW: crowbar resistor; I G 1 : main ignitron; I G 2 : crowbar ignitron; R V : matching resistor; R C, L C, R S, L S : resistance and inductance of the circuit and/or the sample; R 1 – R 4 : voltage dividers; K E 1, K E 2 : knife-edge probes; PP: Pearson-probe; DC: discharge chamber; PY: Pyrometer; L: lens; IF: interference filter; F: fiber; D: photo-diode; A: amplifier; PG: pulse generator; AD: analog-to-digital converter; PC: personal computer; I, U HOT, U COLD, J : measurement signals of current, voltages and intensity of radiation; PSG: polarization state generator; PSD: polarization state detector; LWL: light wire line.

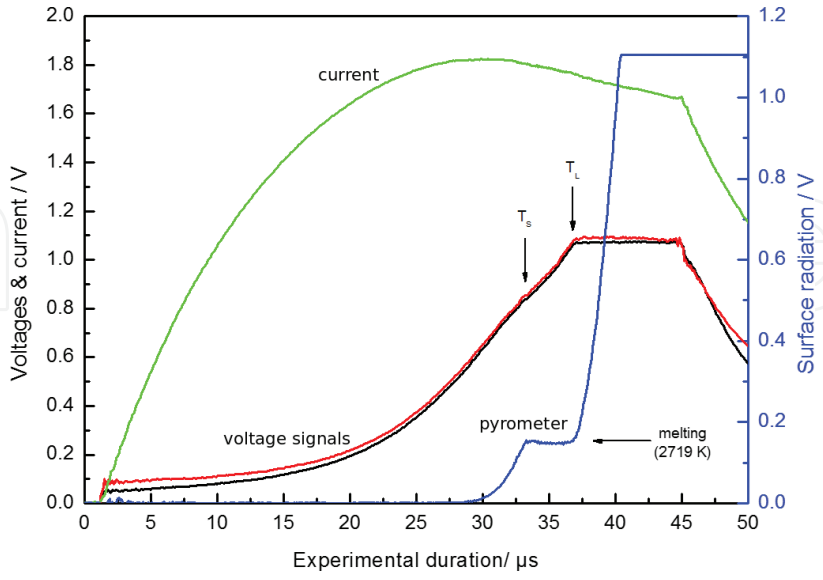

Figure 2. Typical raw measurement signals of the ohmic pulse-heating experiment performed on Iridium. The black line and red line are the voltage signals, the green line is the current signal and the blue line is the signal of the pyrometer. Note that solidus temperature (T_S) and liquidus temperature (T_l) are visible not only in the pyrometer signal, but also in the voltage signals.

linear fits as well as uncertainty assessments. The schematic data provided in this chapter are for aluminum; therefore, the temperature range is rather low. With the ohmic pulse-heating apparatus, it is also possible to examine high melting metals like tungsten, niobium and tantalum.

Figures 3 and **4** show typical results of thermal conductivity and thermal diffusivity determination with the ohmic pulse-heating apparatus for aluminum.

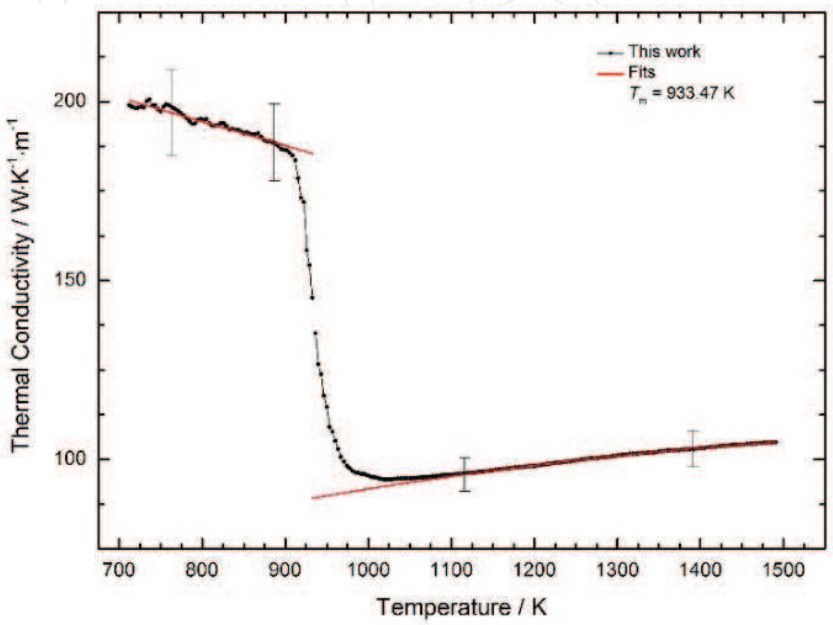

Figure 3. Results of thermal conductivity determination for aluminum. Data taken from [22].

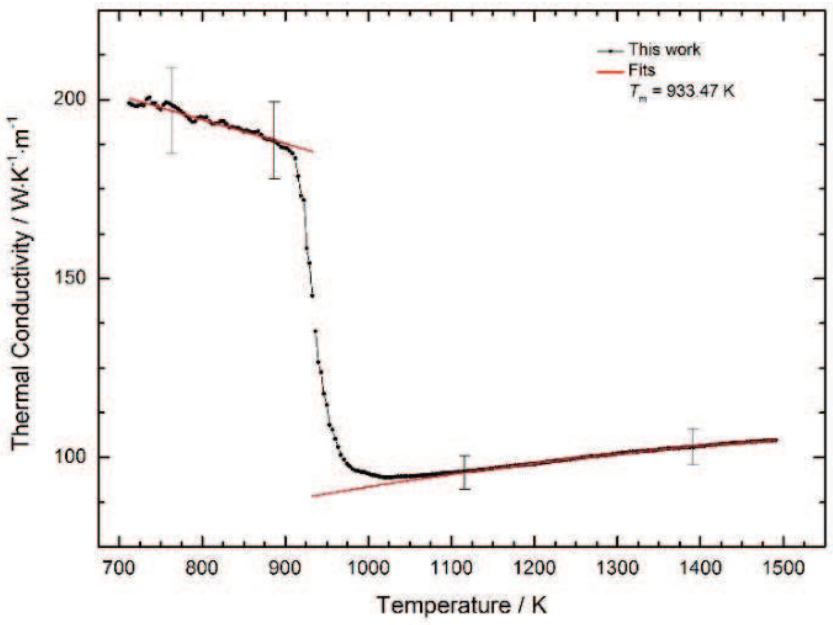

Figure 4. Results of thermal diffusivity determination for aluminum. Data taken from [22].

The data show the solid phase (up to about 900 K) and the liquid phase (up to 1500 K). Thermal conductivity in this case can be fitted quadratically with a positive slope in the liquid phase.

4.5. Uncertainty for the ohmic pulse-heating method

Uncertainties have been estimated according to GUM [32], with a coverage factor of $k = 2$ (95%).

Uncertainties for thermal conductivity $\lambda(T)$ for aluminum have been estimated ±6% in the solid phase and ±5% in the liquid phase. Uncertainties for thermal diffusivity $a(T)$ for aluminum have been estimated ±8% in the solid phase and ±5% in the liquid phase. See also [22].

5. Conclusions

A variety of common methods to determine thermal conductivity of liquid metals have been reviewed in this chapter. These methods can be classified into steady state, non-steady state, and transient techniques. However, not all of the reviewed methods are suitable for the liquid phase of high-melting metals.

To conclude this chapter, the methods that are suitable for the determination of thermal conductivity of high-melting metals in the liquid phase are summarized.

The laser flash method (LFM) is applicable also for high-melting metals, as the temperature range has been reported to be −120 to 2800°C. Uncertainties for this measurement technique range from ±3 to ±15% [16–19].

Another suitable method to determine thermal conductivity of even high-melting metals in the liquid phase is the ohmic pulse-heating method in combination with the Wiedemann-Franz law. This method can easily achieve temperatures of about 4000 K and higher and is therefore suitable for all high-melting metals (the metal with the highest melting point is tungsten with 3695 K). Uncertainties for thermal conductivity for aluminum have been estimated ±6% in the solid phase and ±5% in the liquid phase [22].

Especially in the liquid phase, where lattice contributions in the determination of thermal conductivity can be neglected, the ohmic pulse-heating method has been proven to be a very accurate method. This has been shown in an intercomparison with laser flash measurements in [26].

Author details

Peter Pichler and Gernot Pottlacher*

*Address all correspondence to: pottlacher@tugraz.at

Institute of Experimental Physics, Graz University of Technology, NAWI Graz, Austria

References

[1] Mills KC, Monaghan BJ, Keene BJ. Thermal conductivities of molten metals: Part 1. Pure metals. International Materials Review. 1996;**41**(6):209-242

[2] Maglic KD, Cezairliyan A, Peletsky VE. Compendium of Thermophysical Property Measurement Methods: Vol. 1. Survey of Measurement Techniques. New York, NY: Plenum Press; 1984

[3] Buck W, Rudtsch S. Thermal properties. In: Czichos H, Saito T, Smith L, editors. Springer Handbook of Materials Measurement Methods [Internet]. Berlin, Heidelberg: Springer Berlin Heidelberg; 2006. pp. 399-429. DOI: 10.1007/978-3-540-30300-8_8

[4] Salmon D. Thermal conductivity of insulations using guarded hot plates, including recent developments and sources of reference materials. Measurement Science and Technology. 2001;**12**(12):R89. Available from: http://stacks.iop.org/0957-0233/12/i=12/a=201

[5] [Internet] [cited 2018/01/20]. Available from: https://www.netzsch-thermal-analysis.com/en/products-solutions/thermal-diffusivityconductivity/ghp-456-titan/

[6] Assael MJ, Dix M, Gialou K, Vozar L, Wakeham WA. Application of the transient hot-wire technique to the measurement of the thermal conductivity of solids. International Journal of Thermophysics. 2002;**23**(3):615-633. DOI: 10.1023/A:1015494802462

[7] Hammerschmidt U. A quasi-steady state technique to measure the thermal conductivity. International Journal of Thermophysics. 2003;**24**(5):1291-1312. Available from: http://link.springer.com/article/10.1023/A:1026151101668

[8] Roder HM, Perkins RA, Laesecke A, de Castro CAN. Absolute steady-state thermal conductivity measurements by use of a transient hot-wire system. Journal of Research of the National Institute of Standards and Technology. 2000;**105**(2):221

[9] Hammerschmidt U, Meier V. New transient hot-bridge sensor to measure thermal conductivity, thermal diffusivity, and volumetric specific heat. International Journal of Thermophysics. 2006;**27**(3):840-865. DOI: 10.1007/s10765-006-0061-2

[10] Hammerschmidt U, Sabuga W. Transient hot wire (THW) method: Uncertainty assessment. International Journal of Thermophysics. 2000;**21**(6):1255-1278. Available from: http://link.springer.com/article/10.1023/A:1006649209044

[11] Assael MJ, Antoniadis KD, Wakeham WA. Historical evolution of the transient hot-wire technique. International Journal of Thermophysics. 2010 Jun 1;**31**(6):1051-1072. DOI: 10.1007/s10765-010-0814-9

[12] Cahill DG, Katiyar M, Abelson J. Thermal conductivity of a-Si: H thin films. Physical Review B. 1994;**50**(9):6077

[13] Cahill DG. Thermal conductivity measurement from 30 to 750 K: The 3ω method. Review of Scientific Instruments. 1990;**61**(2):802-808

[14] Choi TY, Maneshian MH, Kang B, Chang WS, Han CS, Poulikakos D. Measurement of the thermal conductivity of a water-based single-wall carbon nanotube colloidal suspension with a modified 3- ω method. Nanotechnology. 2009;**20**(31):315706. Available from: http://stacks.iop.org/0957-4484/20/i=31/a=315706

[15] Parker W, Jenkins R, Butler C, Abbott G. Flash method of determining thermal diffusivity, heat capacity, and thermal conductivity. Journal of Applied Physics. 1961;**32**(9):1679-1684. Available from: http://scitation.aip.org/content/aip/journal/jap/32/9/10.1063/1.1728417

[16] Schriempf JT. A Laser Flash Technique for Determining Thermal Diffusivity of Liquid Metals at Elevated Temperatures. Review of Scientific Instruments. 1972;**43**(5):781-786. DOI: 10.1063/1.1685757

[17] Tada Y, Harada M, Tanigaki M, Eguchi W. Laser flash method for measuring thermal conductivity of liquids—Application to low thermal conductivity liquids. Review of Scientific Instruments. 1978;**49**(9):1305-1314

[18] https://www.netzsch-thermal-analysis.com/en/products-solutions/thermal-diffusivity-conductivity/lfa-427/ [Internet]. Available from: https://www.netzsch-thermal-analysis.com/en/products-solutions/thermal-diffusivity-conductivity/lfa-427/

[19] Kaschnitz E. Private conversation

[20] Hay B, Filtz JR, Hameury J, Rongione L. Uncertainty of thermal diffusivity measurements by laser flash method. International Journal of Thermophysics. 2005 Nov 1;**26**(6):1883-1898. DOI: 10.1007/s10765-005-8603-6

[21] Vozár L, Hohenauer W. Uncertainty of thermal diffusivity measurements using the laser flash method. International Journal of Thermophysics. 2005 Nov 1;**26**(6):1899-1915. DOI: 10.1007/s10765-005-8604-5

[22] Leitner M, Leitner T, Schmon A, Aziz K, Pottlacher G. Thermophysical properties of liquid aluminum. Metallurgical and Materials Transactions A. 2017;**48**:3036-3045

[23] Klemens PG, Williams RK. Thermal conductivity of metals and alloys. International Metals Reviews. 1986;**31**(5):197-215

[24] Pottlacher G, Hosaeus H, Kaschnitz E, Seifter A. Thermophysical properties of Inconel 718 alloy up to 1800 celsius. Scandinavian Journal of Metallurgy. 2002;**31**:161-168

[25] Schmon A. Density Determination of Liquid Metals by Means of Containerless Techniques [Internet]. Graz University of Technology; 2016. Available from: https://www.tugraz.at/fileadmin/user_upload/Institute/IEP/Thermophysics_Group/Files/Diss-SchmonAlexander.pdf

[26] James M, Monaghan B, Cusco L, Redgrove JPQ. Intercomparison of measurements of the thermal diffusivity of molten metals. NPL Report CBTLM S30; 2000

[27] Cagran C, Huepf T, Wilthan B, Pottlacher G. Selected thermophysical properties of Hf-3% Zr from 2200K to 3500K obtained by a fast pulse-heating technique. High Temperatures-High Pressures. 2008;**37**:205-219

[28] Schmon A, Aziz K, Luckabauer M, Pottlacher G. Thermophysical properties of Manganin ($Cu_{86}Mn_{12}Ni_2$) in the solid and liquid state. International Journal of Thermophysics. 2015

[29] Wilthan B, Cagran C, Brunner C, Pottlacher G. Thermophysical properties of solid and liquid platinum. Thermochimica Acta. 2004;**415**:47-54

[30] Cagran C, Wilthan B, Pottlacher G, Roebuck B, Wickins M, Harding RA. Thermophysical properties of a Ti-44%Al-8%Nb-1%B alloy in the solid and molten states. Intermetallics. 2003;**11**:1327-1334

[31] Kaschnitz E, Pottlacher G, Jaeger H. A new microsecond pulse-heating system to investigate thermophysical properties of solid and liquid metals. International Journal of Thermophysics. 1992 Jul;**13**(4):699-710. Available from: http://www.springerlink.com/openurl.asp?genre=article&id=doi:10.1007/BF00501950

[32] Metrology (JCGM/WG 1) WG 1 of the Joint Committee for Guides. In: Guide to the Expression of Uncertainty in Measurement. BIPM; 1993

8.3. Re-investigation of the Normal Spectral Emissivity at 684.5 nm of Solid and Liquid Molybdenum

SHORT SUMMARY The normal spectral emissivity at 684.5 nm of solid and liquid molybdenum was measured by means of a μs-DOAP in combination with an ohmic pulse-heating system.

REMARKS ON AUTHORSHIP

A. Eber performed measurements on solid and liquid molybdenum and wrote chapters “Results”, “Discussion” and “Uncertainty”.
P. Pichler supervised the measuring and publication process. He wrote chapters “Introduction”, “Abstract”, “Experimental Methods” and contributed to the other chapters.
G. Pottlacher supervised the measuring and publication process.

International Journal of Thermophysics (2021) 42:17
https://doi.org/10.1007/s10765-020-02769-7

Re-investigation of the Normal Spectral Emissivity at 684.5 nm of Solid and Liquid Molybdenum

Alexander Eber[1] · **Peter Pichler**[1] · **Gernot Pottlacher**[1]

Received: 8 October 2020 / Accepted: 7 November 2020

Abstract

In this work, we present normal spectral emissivity data of solid and liquid molybdenum at a wavelength of 684.5 nm. The presented results are novel measurements on molybdenum, a material, which was already measured 15 years ago by our group. The present results indicate a lower emissivity in the liquid phase. The novel measurements were done within the European Metrology Programme for Innovation and Research (EMPIR) project 17IND11 Hi-TRACE. The optimized measuring system is an ohmic pulse-heating apparatus combined with microsecond Division of Amplitude polarimetry.

Keywords Normal spectral emissivity · Microsecond polarimetry · Molybdenum · Pulse heating · Subsecond thermophysics

1 Introduction

When investigating thermophysical properties, *i.e.*, temperature-dependent properties, of liquid metals and alloys at high temperatures, measurements need to be performed contactless and containerless. Especially contactless temperature measurement poses manifold complications. Above a temperature of 1234.93 K, the melting point of silver, the international temperature of 1990 (ITS-90) [1], is defined by spectral pyrometry. Pyrometry is based on the fact that every object with a temperature higher than absolute zero, 0 K, emits thermal radiation, which can be detected by, *e.g.*, a photo diode. However, the ratio between emitted thermal radiation of an object and the emitted thermal radiation of a so-called black body (a perfect thermal emitter) under the same conditions needs to be known in order to obtain correct temperatures. This ratio is called the emissivity of the material. Especially, the normal spectral emissivity, meaning the temperature-dependent emissivity, perpendicular to

✉ Gernot Pottlacher
pottlacher@tugraz.at

[1] Institute of Experimental Physics, Graz University of Technology, NAWI Graz Petersgasse 16, 8010 Graz, Austria

Published online: 28 December 2020

the surface of the object analyzed at the wavelength of the pyrometer used for measurement, needs to be known.

At the thermo- and metalphysics group of the institute of experimental physics of Graz University of Technology, a fast ohmic pulse-heating system is used to measure thermophysical properties of liquid metals and alloys, see, *e.g.* [2]. The setup was extended by a microsecond Division of Amplitude Photopolarimeter (µs-DOAP) in 2001 [3]. The µs-DOAP allows the measurement of normal spectral emissivity at a wavelength of 684.5 nm. After a longer period of inactivity, the µs-DOAP system was re-established as part of Graz University of Technology's contribution to the European Metrology Programme for Innovation and Research (EMPIR) project 17IND11 "Hi-TRACE." After ensuring the functionality of the apparatus, the normal spectral emissivity of solid and liquid molybdenum at 684.5 nm was measured and compared to previously published data in 2004, Cagran *et al.* [4], 2005, Cagran *et al.* [5] and 2013, Pottlacher *et al.* [6].

A discrepancy between the previously published data and the newly obtained data was detected. After re-evaluating the original data, obtained by Cagran *et al.*, we conclude that the previously reported data in the liquid phase are too high. Therefore, newly measured and evaluated values are published in this work.

2 Experimental Methods

The methods used to obtain normal spectral emissivity of solid and liquid molybdenum are a combination of an ohmic pulse-heating apparatus with a µs-DOAP. Both measuring systems have been thoroughly described in previous publications, *e.g.* [7, 8]. Only a short description of the measuring system is given in this work.

2.1 Ohmic Pulse-Heating Apparatus (OPA)

The ohmic pulse-heating apparatus (OPA) works as follows: A large current pulse (some 1000 A) is distributed through a wire-shaped sample, with a diameter of 0.5 nm. Due to its electrical resistivity, the sample heats up, melts, and once it reaches the material's boiling point, it explodes. Thus, the technique was also called exploding wire technique. The whole process of heating up through the solid phase, melting, and passing through the liquid phase only takes around 30 µs to 50 µs. Besides the prevention of chemical reactions with any surroundings, this short experimental time also ensures that the liquid wire can be observed, without collapsing due to gravitational forces. The temperature measurement is performed by pyrometry. An especially designed pyrometer for very fast time responses, operating at a wavelength of 649.7 nm, is used to measure the radiance temperature of the sample. The radiance temperature can later be used, to calculate the true temperature if the normal spectral emissivity of the sample is known, measured, or estimated. Additional information about the measuring system can be found, *e.g.,* in [9].

2.2 Microsecond Division of Amplitude Photopolarimeter (μs-DOAP)

Polarimetry is a powerful tool to measure normal spectral emissivity (see, *e.g.* [10]). Usually polarimetry instruments depend on rotating or other moveable parts. For fast experimental time scales, like OPA measurements, a polarimeter with moveable parts would suffer from insufficient resolution. Such instruments might even not be capable to obtain one data point during one OPA experiment. In 1982, Azzam [11] designed an instrument without moveable parts. The working principle is as follows: An incident laser beam with a wavelength of 684.5 nm passes the so-called polarization state generator (PSG), which as the name suggests generates a linearly polarized beam. This laser beam is then reflected by the wire-shaped sample inside the experimental chamber of the OPA, which changes the state of polarization. At an angle of incidence of 70°, the reflected laser beam hits the polarization state detector (PSD). A coated beam splitter then splits up the laser beam and the two resulting beams each pass a Glan–Thompson prism. Finally, there are four laser beams, which are detected by separate photo diodes. By calibrating the measuring system beforehand, these four detector signals are used to calculate the so-called Stokes vector. From the Stokes vector, the normal spectral emissivity of the sample at the wavelength of the incident laser beam can be calculated. More information on the measuring system and the data analysis can be found in previous publications [3, 4, 8, 12, 13].

3 Results

Normal spectral emissivity data for solid and liquid molybdenum are presented in the following. Figure 1 shows normal spectral emissivity data as a function of radiance temperature T_r for both the solid and the liquid phase. Keep in mind, that normal spectral emissivity in the solid phase is highly dependent on the surface condition. The samples were prepared by polishing them with abrasive paper (grade 1200) and subsequently cleaned by acetone. This procedure was performed consistently over all experiments to ensure comparability.

The data were evaluated for a radiance temperature of 2520 K (at the pyrometer wavelength), the melting point of molybdenum [6]. The linear regression lines were calculated from 1650 K to 2490 K for the solid phase and from 2550 K to 3190 K for the liquid phase. The measurement range of the pyrometer limits the temperature ranges. In the solid phase, the linear regression line of the normal spectral emissivity is given by

$$\epsilon_{684.5\ \mathrm{nm,s}}(T_\mathrm{r}) = 0.623 - 6.31 \times 10^{-5} \cdot T_\mathrm{r} \quad \text{for} \quad 1650\ \mathrm{K} \leq T_\mathrm{r} \leq 2490\ \mathrm{K}. \tag{1}$$

However, in the solid phase, two clusters of data can be seen. Additional to the fit of all data in the solid phase, both clusters were also evaluated separately. There are three datasets in the upper cluster, denoted with *top*, which can be approximated by a linear regression line of

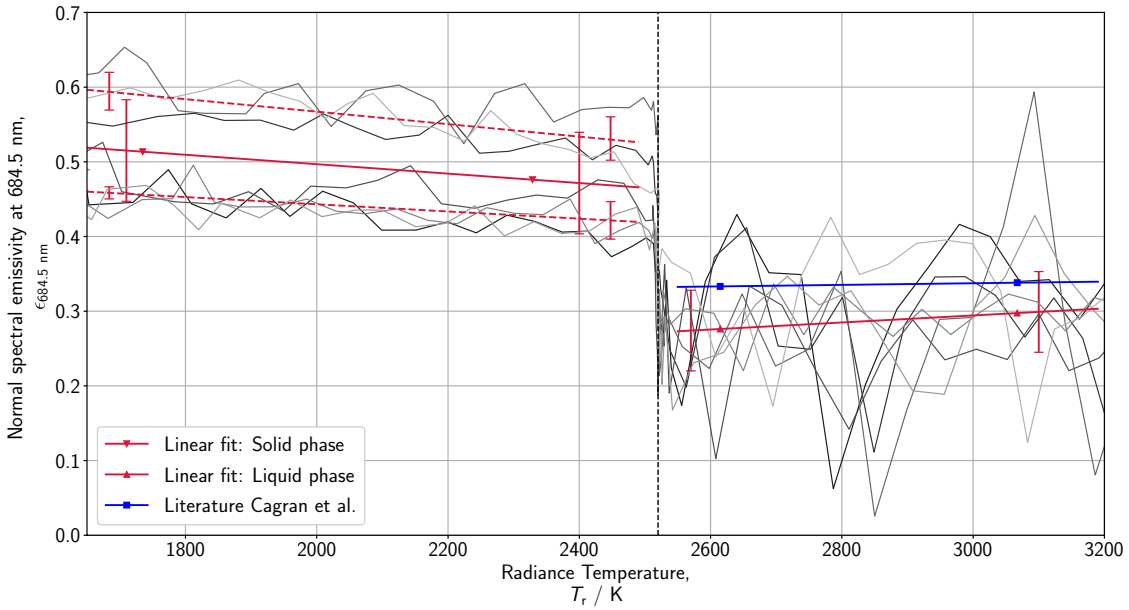

Fig. 1 Normal spectral emissivity at 684.5 nm $\epsilon_{684.5\ \mathrm{nm}}$ as a function of radiance temperature T_r for 649.7 nm, seven independent measurements with linear regression lines and statistical uncertainty analysis, errorbars represent single standard deviations in the solid phase and $k = 2$ standard deviations in the liquid phase. gray lines: measurement data, solid red lines: linear regression lines for solid and liquid phase, dotted red lines: linear regression lines for the two clusters in the solid phase, blue line: literature data from 2004, Cagran *et al.* [4].

$$\epsilon_{684.5\ \mathrm{nm,s,\ top}}(T_\mathrm{r}) = 0.734 - 8.36 \times 10^{-5} \cdot T_\mathrm{r} \quad \text{for} \quad 1650\ \mathrm{K} \leq T_\mathrm{r} \leq 2490\ \mathrm{K}. \tag{2}$$

In the lower cluster, denoted with *bottom*, four datasets can be found. This suggests an approximately equal distribution between the two bulks. The following linear regression line approximates the lower bulk:

$$\epsilon_{684.5\ \mathrm{nm,s,\ bottom}}(T_\mathrm{r}) = 0.540 - 4.83 \times 10^{-5} \cdot T_\mathrm{r} \quad \text{for} \quad 1650\ \mathrm{K} \leq T_\mathrm{r} \leq 2490\ \mathrm{K}. \tag{3}$$

In the liquid phase, a linear regression line approximates the normal spectral emissivity by

$$\epsilon_{684.5\ \mathrm{nm,l}}(T_\mathrm{r}) = 0.153 + 4.71 \times 10^{-5} \cdot T_\mathrm{r} \quad \text{for} \quad 2550\ \mathrm{K} \leq T_\mathrm{r} \leq 3190\ \mathrm{K}. \tag{4}$$

By extrapolating the linear fit of the liquid phase towards the melting point, the normal spectral emissivity at the melting temperature can be estimated by

$$\epsilon_{684.5\ \mathrm{nm}}(T_\mathrm{m}) = 0.272 \pm 0.027. \tag{5}$$

4 Discussion

The resulting normal spectral emissivity in the liquid phase is, close to the melting temperature, outside of the calculated $k = 2$ uncertainty interval and overall lower by about 20 % than the values presented in the articles 2004, Cagran *et al.* [4], 2005, Cagran *et al.* [5], and 2013, Pottlacher *et al.* [6]. After revisiting of the original data from 2004, Cagran *et al.* [4], one dataset was omitted because of an incorrect temperature allocation and one dataset was taken out because of an atypical evolution of the emissivity in the liquid phase. By removing these two datasets, the resulting emissivity decreases significantly.

Within this work, two different clusters of data were measured, with a significant difference in emissivity in the solid phase. The surface treatment was performed consistently over all experiments with a certain number of strokes in certain directions with abrasive paper and acetone. Although the experiments were performed over several days, no correlation of the data with any external influences was found. Measurements with results in both clusters were performed on each day and the room temperature as well as the nitrogen atmosphere was comparable during all experiments.

5 Uncertainty

Uncertainty estimation of the emissivity measurements with the µs-DOAP is challenging. While at first glance the obtained data seem to have a rather high uncertainty of about 30 %, comparison with other institutes in the past showed a good agreement of the measured data. The uncertainty is increased by single data points, which do not follow the characteristic, linear temperature evolution.

In 1970, Jaeger [14] suggested that these peaks are caused by magnetohydrodynamic oscillations on the surface. Before the experiments, the measurement devices are adjusted to the position of the wire. If the wire would start oscillating, the measurement devices are not adjusted properly any more because the reflection of the laser after the wire might not be correctly directed in the detector. Therefore, the oscillations are influencing the measurement of the emissivity by changing the geometry. If only the normal spectral emissivity is considered, the uncertainty can be estimated significantly lower. Therefore, only the linear regression lines for every single experiment are used for the uncertainty estimation of the normal spectral emissivity. The uncertainty is calculated by looking at the deviation between these averages. To quantify a reasonable uncertainty, we suggest the following routine:

The uncertainty estimation was performed separately for the solid and the liquid phase. A linear regression line was calculated for every single measurement, for both the solid and the liquid phase. Then, the average of the linear regression lines together with the standard deviation was calculated. In Fig. 1, the average of the standard deviation, together with the average as a function of the radiance temperature, is shown.

This method weights single peaks in the data only very lightly, because of the averaging process. On the other hand, it allows a good understanding of the deviations between the different experiments. For the solid phase, an average single standard deviation of $\Delta\varepsilon_{684.5\ \mathrm{nm,s}}(T_\mathrm{r}) = 0.068$ was calculated if all data points are included. If only the upper bulk is considered, the single standard deviation for the solid phase is $\Delta\varepsilon_{684.5\ \mathrm{nm,s,top}}(T_\mathrm{r}) = 0.024$. If only the lower bulk is considered, the single standard deviation for the solid phase is $\Delta\varepsilon_{684.5\ \mathrm{nm,s,bottom}}(T_\mathrm{r}) = 0.016$. For the liquid phase, an average single standard deviation of $\Delta\varepsilon_{684.5\ \mathrm{nm,l}}(T_\mathrm{r}) = 0.027$ is reached with this evaluation method. This equates to about 10 % of the value for the liquid phase. After considering several different types of B uncertainties, we concluded that the combined uncertainty is mainly governed by the statistical uncertainty.

Acknowledgements Hi-TRACE Project has received funding from the EMPIR initiative co-financed by the Participating States and from the European Union's Horizon 2020 research and innovation programme.

Funding Open access funding provided by Graz University of Technology.

References

1. W. Blanke, Die Internationale Temperaturskala von 1990: ITS-90 (Physikalisch-Technische Bundensanstalt) (1989)
2. P. Pichler, B.J. Simonds, J.W. Sowards, G. Pottlacher, J. Mater. Sci. **55**, 4081 (2019). https://doi.org/10.1007/s10853-019-04261-6
3. A. Seifter, F. Sachsenhofer, S. Krishnan, G. Pottlacher, Int. J. Thermophys. **22**, 1537 (2001)
4. C. Cagran, B. Wilthan, G. Pottlacher, Int. J. Thermophys. **25**, 1551 (2004)
5. C. Cagran, G. Pottlacher, M. Rink, W. Bauer, Int. J. Thermophys. **26**, 1001 (2005). https://doi.org/10.1007/s10765-005-6680-1
6. G. Pottlacher, K. Boboridis, C. Cagran, T. Huepf, A. Seifter, B. Wilthan, Temperature: its measurement and control in science and industry, volume 8. In: Proceedings of the Ninth International Temperature Symposium, AIP Publishing, vol. 1552, pp. 704–709 (2013)
7. E. Kaschnitz, G. Pottlacher, H. Jaeger, Int. J. Thermophys. **13**, 699 (1992). https://doi.org/10.1007/BF00501950
8. A. Seifter, F. Sachsenhofer, G. Pottlacher, Int. J. Thermophys. **23**, 1267 (2002)
9. M. Leitner, T. Leitner, A. Schmon, K. Aziz, G. Pottlacher, Metall. Mater. Trans. A **48**, 3036 (2017). https://doi.org/10.1007/s11661-017-4053-6
10. H.G. Thompson, E.A. Irene (eds.), Handbook of Ellipsometry. William Andrew Inc., New York
11. R. Azzam, Opt. Acta Int. J. Opt. **29**, 685 (1982). https://doi.org/10.1080/713820903
12. A. Seifter, Bestimmung des normalen spektralen Emissionskoeffizienten von flüssigen pulsgeheizten Metallen mittels eines schnellen Photopolarimeters. Ph.D. Thesis (2001)
13. C. Cagran, Untersuchung des Emissionsverhaltens flüssiger Metalle mittels Photopolarimetrie und Mehrwellenlängenpyrometrie. Ph.D. Thesis (2004)

14. H. Jaeger. Die physikalischen Vorgänge bei elektrischen Drahtexplosionen. Habilitationsschrift (1970)

8.4. Surface Tension and Thermal Conductivity of NIST SRM 316L Stainless Steel

SHORT SUMMARY Surface tension and thermal conductivity of the NIST SRM 316L stainless steel have been measured and compared to other AISI 316 and AISI 316L stainless steels in the literature.

REMARKS ON AUTHORSHIP

P. Pichler performed pulse-heating measurements to obtain thermal conductivity and contributed to electromagnetic levitation measurements to obtain surface tension.
T. Leitner performed electromagnetic levitation measurements to obtain surface tension.
E. Kaschnitz performed laser flash measurements to obtain thermal conductivity.
J. Rattenberger performed energy-dispersive X-ray spectroscopy measurements.
G. Pottlacher supervised the measuring and publication process and managed communication between the authors.

Appendix

Appendix A.

Experimental Data

Table A.1.: Collected thermophysical data of NIST SRM 1155a. D is the density, ρ_{IG} is the electrical resistivity, assuming initial geometry, ρ_{corr} is the electrical resistivity, corrected for thermal expansion, H_{s} is the specific enthalpy, $\frac{V(T)}{V_0}$ is the thermal expansion and T is the temperature.

T	H_{S}	ρ_{IG}	ρ_{corr}	$D(T)$	$\frac{V(T)}{V_0}$
K	$\mathrm{kJ{\cdot}kg^{-1}}$	$\mu\Omega{\cdot}\mathrm{m}$	$\mu\Omega{\cdot}\mathrm{m}$	$\mathrm{kg{\cdot}m^{-3}}$	1
500	109	0.954	0.970	7770	1.017
600	163	1.007	1.033	7714	1.025
700	218	1.054	1.089	7657	1.033
800	274	1.093	1.138	7601	1.041
900	333	1.128	1.183	7544	1.049
1000	393	1.157	1.223	7488	1.057
1100	454	1.182	1.259	7432	1.065
1200	515	1.203	1.290	7375	1.073
1300	554	1.218	1.316	7319	1.081
1400	626	1.232	1.342	7263	1.089
1500	697	1.247	1.368	7206	1.097
1600	769	1.262	1.394	7150	1.105
1700	1042	1.291	1.464	6964	1.132
1800	1190	1.299	1.495	6857	1.151
1900	1275	1.301	1.514	6791	1.163
2000	1360	1.303	1.532	6725	1.176
2100	1444	1.305	1.551	6659	1.189
2200	1529	1.307	1.570	6593	1.201
2300	1614	1.309	1.589	6527	1.214
2400	1699	1.311	1.608	6461	1.226
2500	1783	1.313	1.627	6395	1.239
2600	1868	1.315	1.646	6329	1.251
2700	1953	1.317	1.665	6262	1.264
2800	2037	1.319	1.684	6196	1.277

Table A.2.: Specific heat capacity c_p for NIST SRM 1155a as a function of temperature T determined via DSC. Δc_p denotes the $k = 2$ uncertainty.

T / K	c_p / kJ·kg^{-1}·K^{-1}	$\Delta(c_p)$ / kJ·kg^{-1}·K^{-1}	T / K	c_p / kJ·kg^{-1}·K^{-1}	$\Delta(c_p)$ / kJ·kg^{-1}·K^{-1}
473	0.528	0.011	873	0.595	0.005
493	0.529	0.009	893	0.598	0.005
513	0.530	0.007	913	0.599	0.005
533	0.532	0.006	933	0.600	0.005
553	0.534	0.005	953	0.601	0.004
573	0.537	0.006	973	0.603	0.004
593	0.541	0.006	993	0.605	0.005
613	0.544	0.006	1013	0.606	0.005
633	0.547	0.006	1033	0.608	0.005
653	0.550	0.006	1053	0.610	0.005
673	0.553	0.006	1073	0.611	0.005
693	0.556	0.005	1093	0.613	0.006
713	0.559	0.005	1113	0.614	0.006
733	0.561	0.005	1133	0.615	0.006
753	0.564	0.005	1153	0.617	0.008
773	0.566	0.005	1173	0.619	0.009
793	0.569	0.006	1193	0.620	0.010
813	0.572	0.006	1213	0.621	0.012
833	0.578	0.007	1233	0.622	0.013
853	0.587	0.006	1253	0.624	0.015

Table A.3.: Surface tension data for NIST SRM 1155a. T is the temperature and γ is the surface tension

T / K	ΔT / K	γ / N·m^{-1}	$\Delta\gamma$ / N·m^{-1}
1723	9	1575	22
1731	9	1577	22
1734	30	1620	22
1734	10	1587	22
1738	9	1588	21
1741	9	1585	22
1744	10	1599	22
1749	9	1613	22
1754	11	1572	22
1762	10	1610	22
1765	9	1602	22
1767	10	1597	22
1780	10	1620	22
1780	10	1611	22
1787	11	1631	22
1793	10	1600	22
1793	12	1622	22
1807	10	1615	22
1813	10	1617	22
1824	17	1588	22
1830	11	1589	22
1836	10	1637	23
1857	11	1603	22

Table A.4.: TEMPUS Surface tension data for the nickel-base super-alloy L625. T is the temperature and γ is the surface tension

T K	ΔT K	γ $N \cdot m^{-1}$	$\Delta\gamma$ $N \cdot m^{-1}$
1470	10	1.84	0.09
1476	10	1.87	0.09
1476	10	1.86	0.09
1482	10	1.82	0.09
1483	10	1.83	0.09
1485	10	1.85	0.09
1493	10	1.82	0.09
1497	10	1.88	0.09
1503	10	1.82	0.09
1512	10	1.85	0.09
1513	10	1.82	0.09
1523	10	1.80	0.09
1540	10	1.93	0.10
1576	10	1.78	0.09
1606	12	1.84	0.09
1612	11	1.83	0.09
1619	11	1.86	0.09
1633	12	1.83	0.09

Table A.5.: TEMPUS viscosity data for the nickel-base super-alloy L625. T is the temperature and η is the surface tension

T K	ΔT K	η Pa·s	$\Delta\eta$ Pa·s
1470	10	0.0174	0.0017
1476	10	0.0178	0.0018
1476	10	0.0188	0.0019
1483	10	0.0167	0.0017
1485	10	0.0189	0.0019
1493	10	0.0148	0.0015
1503	10	0.0199	0.0020
1513	10	0.0212	0.0021
1523	10	0.0192	0.0019
1527	10	0.0131	0.0013
1619	11	0.0083	0.0008
1633	11	0.0033	0.0003
1647	12	0.0079	0.0008
1687	12	0.0053	0.0005

Appendix B.

EDX Results for NIST SRM 1155a

Label:qx11655: 1155a 3 vor Exp. [20keV]

kV:20.0 Tilt:0.0 Take-off:36.6 Det: SUTW Sapphire

Res:129 Amp.T:51.20 FS:5359 Lsec:100

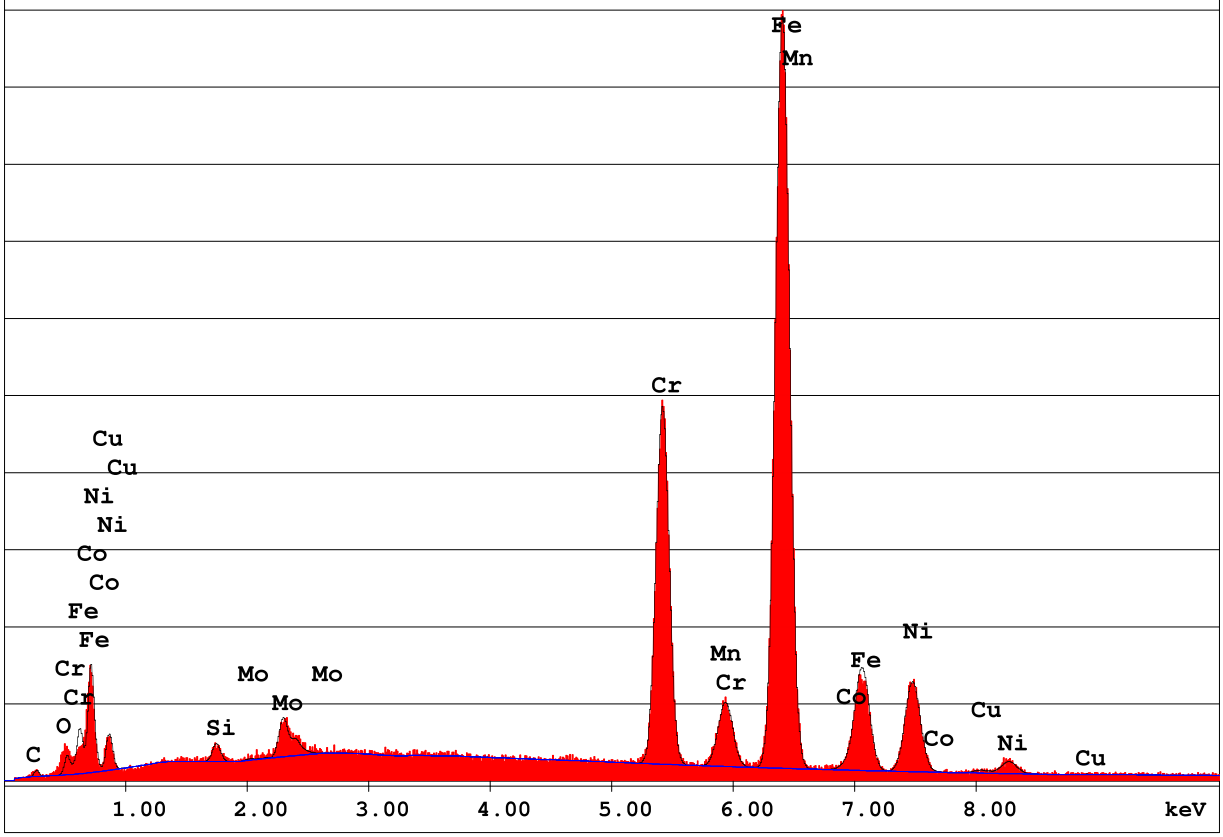

EDAX PhiRhoZ Quantification (Standardless)
Element Normalized
SEC Table :

Element	Wt %	At %	K-Ratio	Z	A	F
SiK	0.63	1.25	0.0033	1.1481	0.4525	1.0019
MoL	3.18	1.85	0.0232	0.8993	0.8118	1.0019
CrK	19.28	20.68	0.2171	1.0023	0.9842	1.1415
MnK	1.48	1.50	0.0146	0.9835	0.9919	1.0116
FeK	64.21	64.11	0.6280	1.0014	0.9639	1.0132
CoK	0.57	0.54	0.0054	0.9806	0.9720	1.0007
NiK	10.12	9.61	0.0925	1.0156	0.9000	1.0000
CuK	0.54	0.47	0.0048	0.9669	0.9197	1.0000
Total	100.00	100.00				

Element	Net Inte.	Bkgd Inte.	Inte. Error	P/B
SiK	8.59	11.79	6.60	0.73
MoL	20.00	14.81	3.52	1.35
CrK	268.03	15.77	0.65	17.00
MnK	17.12	13.72	3.90	1.25
FeK	606.42	12.66	0.41	47.90
CoK	4.42	10.78	11.53	0.41
NiK	77.79	9.71	1.27	8.01
CuK	2.78	8.11	15.68	0.34

Label:qx11654: 1155a 2 nach Exp. [20keV]

kV:20.0 Tilt:0.0 Take-off:36.7 Det: SUTW Sapphire

Res:129 Amp.T:51.20 FS:5077 Lsec:100

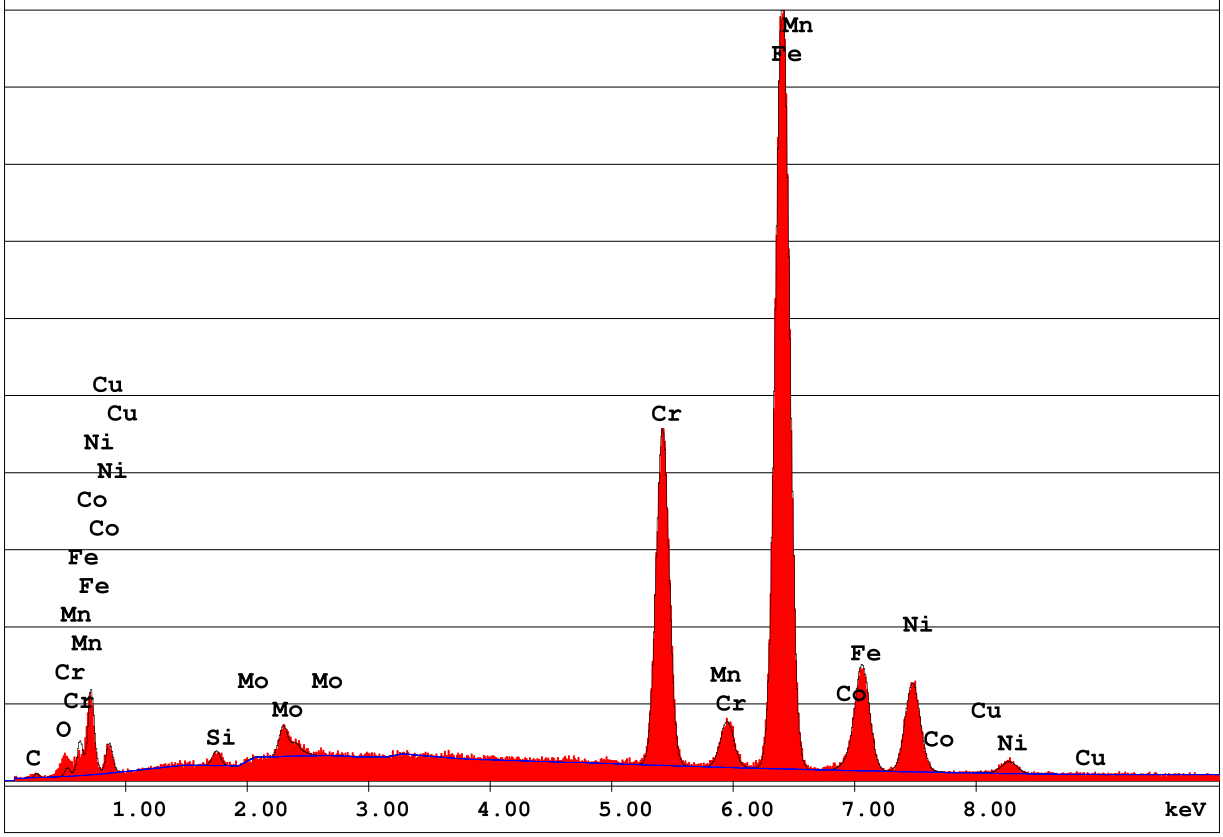

EDAX PhiRhoZ Quantification (Standardless)
Element Normalized
SEC Table :

Element	Wt %	At %	K-Ratio	Z	A	F
SiK	0.52	1.03	0.0027	1.1472	0.4510	1.0018
MoL	2.56	1.49	0.0187	0.8986	0.8104	1.0018
CrK	18.34	19.65	0.2083	1.0015	0.9851	1.1517
MnK	0.11	0.11	0.0011	0.9827	0.9926	1.0117
FeK	67.41	67.24	0.6600	1.0005	0.9661	1.0130
CoK	0.71	0.67	0.0068	0.9798	0.9757	1.0003
NiK	10.17	9.65	0.0928	1.0148	0.8992	1.0000
CuK	0.19	0.17	0.0017	0.9660	0.9189	1.0000
Total	100.00	100.00				

Element	Net Inte.	Bkgd Inte.	Inte. Error	P/B
SiK	6.59	8.81	7.47	0.75
MoL	14.98	14.24	4.40	1.05
CrK	239.21	13.81	0.68	17.32
MnK	1.17	12.15	43.13	0.10
FeK	592.72	11.37	0.42	52.13
CoK	5.14	9.86	9.70	0.52
NiK	72.57	9.06	1.31	8.01
CuK	0.92	7.72	43.96	0.12

Company Name: FELMI-ZFE

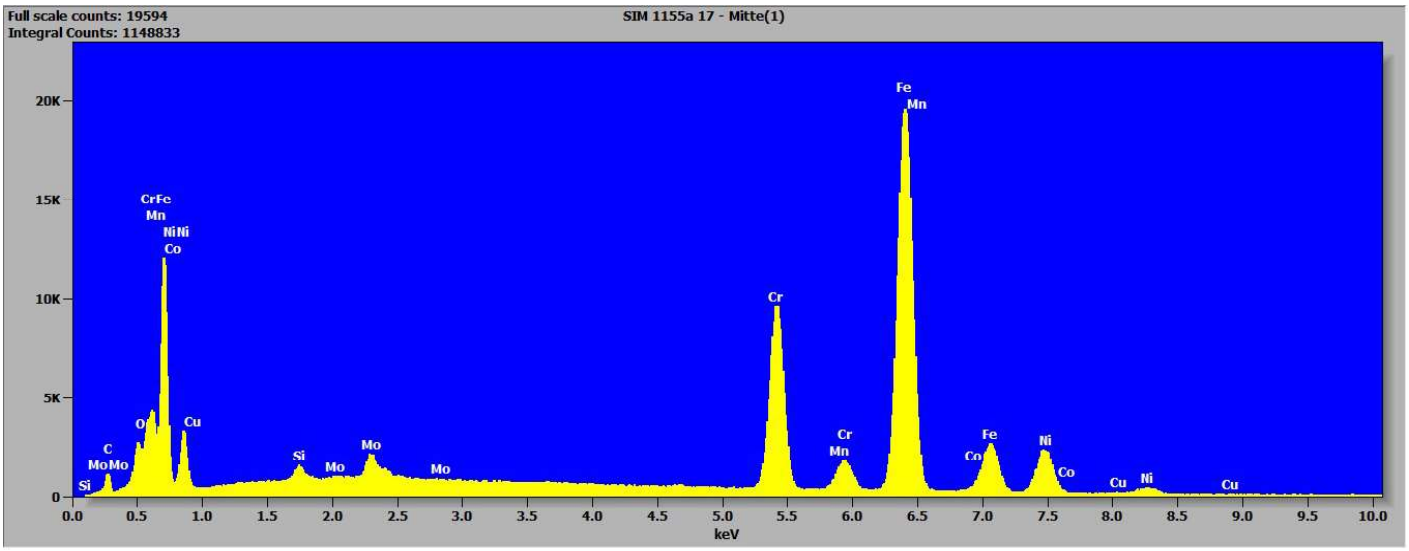

Acc.Voltage: 20.0 kV Take Off Angle: 35.8 deg.

Quantitative Results for: SIM 1155a 17 - Mitte(1)

Element	*Net Counts*	*Weight %*	*Atom %*
Si	6515	0.7	1.3
Cr	135401	17.1	18.3
Mn	6056	1.2	1.2
Fe	303273	65.7	65.5
Co	944	0.3	0.3
Ni	37539	12.6	11.9
Cu	282	0.1	0.1
Mo	19022	2.4	1.4
Total		100.0	100.0

Company Name: FELMI-ZFE

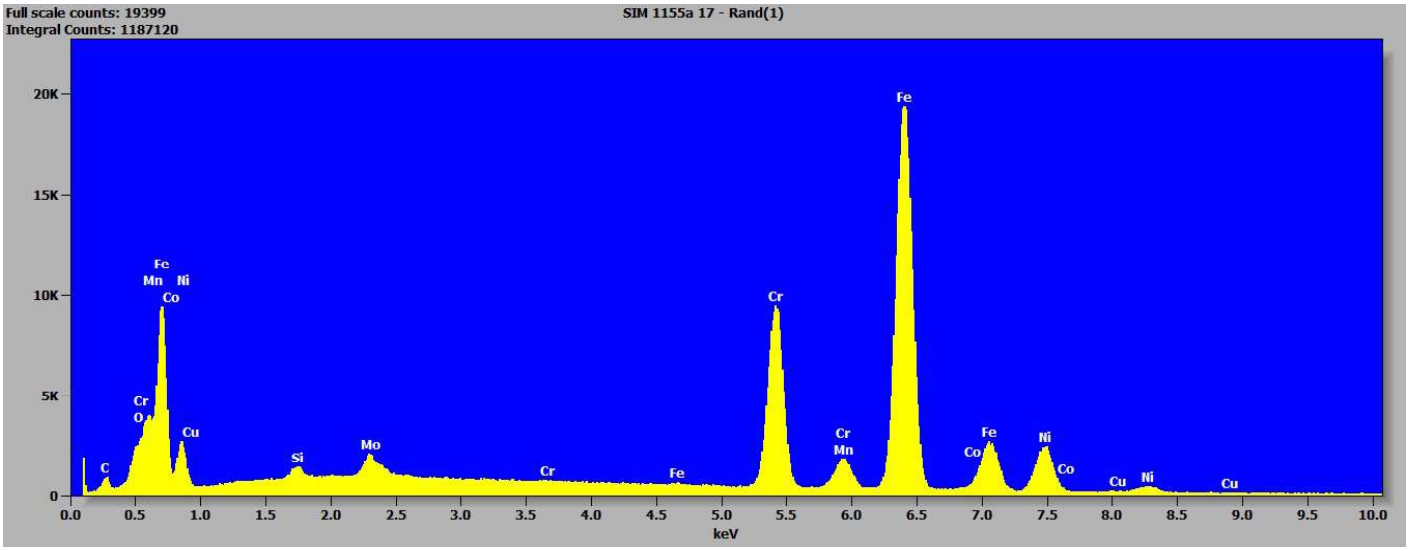

Acc.Voltage: 20.0 kV Take Off Angle: 35.8 deg.

Quantitative Results for: SIM 1155a 17 - Rand(1)

Element	Net Counts	Weight %	Atom %
Si	6376	0.6	1.3
Cr	141035	17.1	18.3
Mn	5411	1.0	1.0
Fe	315952	65.6	65.4
Co	923	0.3	0.3
Ni	40107	12.9	12.2
Cu	343	0.1	0.1
Mo	19485	2.4	1.4
Total		100.0	100.0

Company Name: FELMI-ZFE

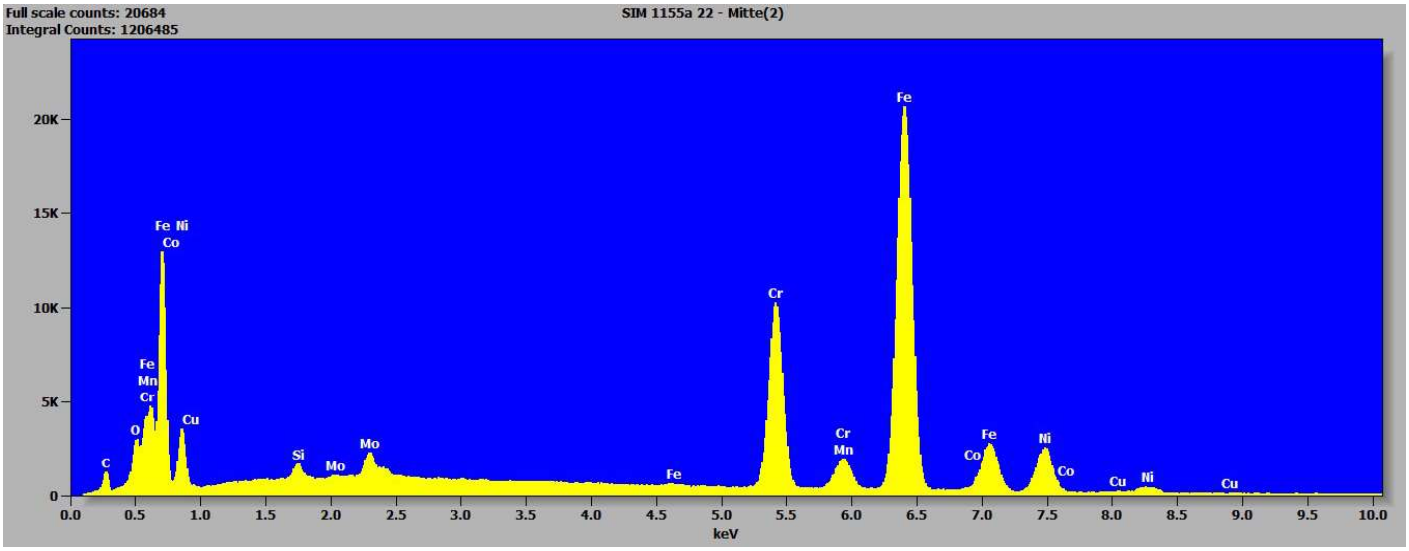

Acc.Voltage: 20.0 kV Take Off Angle: 34.3 deg.

Quantitative Results for: SIM 1155a 22 - Mitte(2)

Element	*Net Counts*	*Weight %*	*Atom %*
Si	7174	0.7	1.5
Cr	140200	17.0	18.2
Mn	7311	1.3	1.4
Fe	316228	65.6	65.4
Co	679	0.2	0.2
Ni	38849	12.5	11.8
Cu	729	0.3	0.3
Mo	18713	2.3	1.4
Total		100.0	100.0

Company Name: FELMI-ZFE

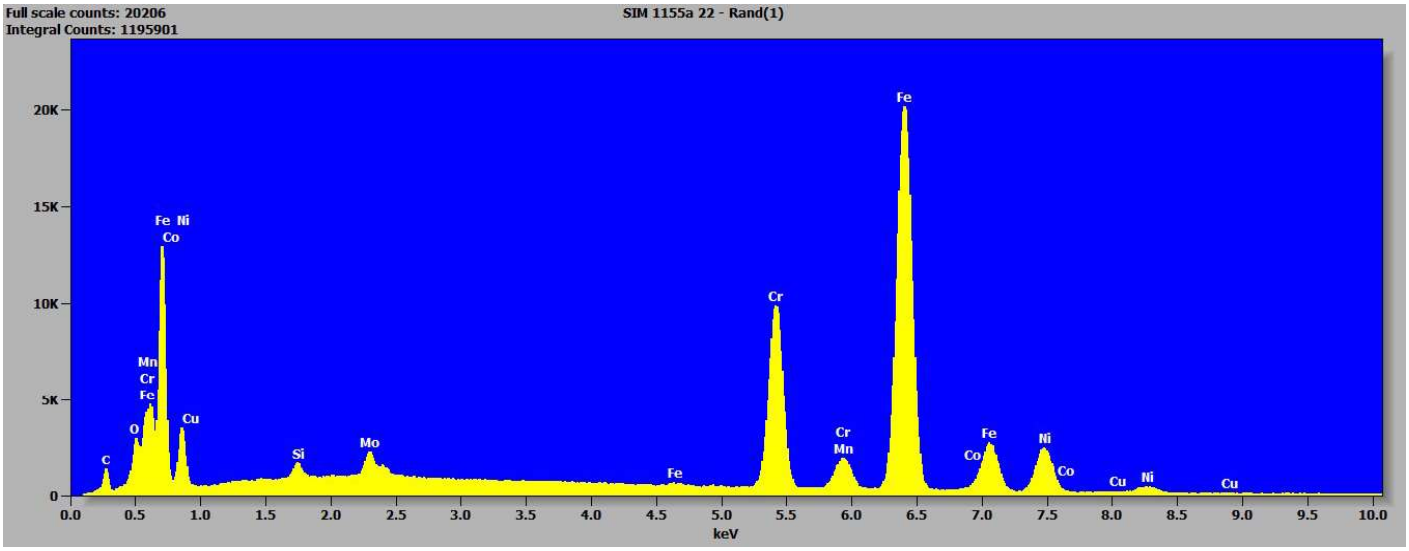

Acc.Voltage: 20.0 kV Take Off Angle: 34.3 deg.

Quantitative Results for: SIM 1155a 22 - Rand(1)

Element	*Net Counts*	*Weight %*	*Atom %*
Si	7121	0.7	1.5
Cr	137850	16.8	18.0
Mn	7655	1.4	1.4
Fe	312060	65.3	65.1
Co	741	0.3	0.2
Ni	39756	12.9	12.2
Cu	314	0.1	0.1
Mo	19527	2.5	1.4
Total		100.0	100.0

Bibliography

[1] *Working Group 1 of the Joint Committee for Guides in Metrology (JCGM/WG 1). Guide to the expression of uncertainty in measurement*. BIPM, 1993.

[2] E. Kaschnitz, G. Pottlacher, and H. Jaeger. "A new microsecond pulse-heating system to investigate thermophysical properties of solid and liquid metals." In: *International Journal of Thermophysics* 13.4 (July 1992), pp. 699–710. DOI: 10.1007/BF00501950.

[3] A. Schmon. "Density Determination of Liquid Metals by Means of Containerless Techniques." PhD thesis. Institute of Experimental Physics, Graz University of Technology, 2016.

[4] C. Cagran. "Untersuchung des Emissionsverhaltens flüssiger Metalle mittels Photopolarimetrie und Mehrwellenlängenpyrometrie." PhD thesis. Institut für Experimentalphysik der Technischen Universität Graz, 2004.

[5] M. Leitner, W. Schröer, and G. Pottlacher. "Density of Liquid Tantalum and Estimation of Critical Point Data." In: *International Journal of Thermophysics* 39.11 (Sept. 2018). DOI: 10.1007/s10765-018-2439-3.

[6] G. Pottlacher and T. Hüpf. In: *Thermal Conductivity 30/Thermal Expansion 18*. Ed. by D. S. Gaal. Lancaster: DEStech Publications, Inc., 2010, pp. 195–206.

[7] T. Hüpf. "Density Determination of Liquid Metals." PhD thesis. Graz University of Technology, 2010.

[8] M. Leitner. "Density of Liquid High-Melting Metals and the Estimation of Critical Point Data." PhD thesis. Graz University of Technology, 2019.

[9] F. Sachsenhofer. "Data evaluation for pulse heating experiments combined with emissivity measurements using adivision-of-amplitude photopolarimeter." MA thesis. Institut für Experimentalphysik der Technischen Universität Graz, 2000.

[10] A. Sommerfeld. "Zur Elektronentheorie der Metalle auf Grund der Fermischen Statistik." In: *Zeitschrift für Physik* 47.1-2 (Jan. 1928), pp. 1–32. DOI: 10.1007/bf01391052.

[11] C. Cagran. "Thermal Conductivity and Thermal Diffusivity of Liquid Copper." MA thesis. Institut für Experimentalphysik der Technischen Hochschule Graz, 2000.

[12] P. Klemens and R. Williams. "Thermal conductivity of metals and alloys." In: *Int. Metals Reviews* 31.5 (1986), pp. 197–215.

[13] H. G. Thompson and E. A. Irene, eds. *Handbook of Ellipsometry*. 2005. ISBN: 0-8155-1499-9.

[14] R. M. A. Azzam. "Division-of-amplitude Photopolarimeter (DOAP) for the Simultaneous Measurement of All Four Stokes Parameters of Light." In: *Optica Acta: International Journal of Optics* 29.5 (May 1982), pp. 685–689. DOI: 10.1080/713820903.

[15] S. Krishnan. "Calibration, properties, and applications of the division-of-amplitude photopolarimeter at 6328 and 1523 nm." In: *Journal of the Optical Society of America A* 9.9 (Sept. 1992), p. 1615. DOI: 10.1364/josaa.9.001615.

[16] R. M. A. Azzam and A. G. Lopez. "Accurate calibration of the four-detector photopolarimeter with imperfect polarizing optical elements." In: *Journal of the Optical Society of America A* 6.10 (Oct. 1989), p. 1513. DOI: 10.1364/josaa.6.001513.

[17] A. Seifter. "Bestimmung des normalen spektralen Emissionskoeffizienten von flüssigen pulsgeheizten Metallen mittels eines schnellen Photopolarimeters." PhD thesis. Institut für Experimentalphysik der Technischen Universität Graz, 2001.

[18] A. Eber. "Measurements of normal spectral emissivity data @684.5nm of metals in the solid and liquid phaseusing a s-DOAP." MA thesis. Institute of Experimental Physics, Graz University of Technology, 2020.

[19] O. Muck. "German Patent No. 422004." 1923.

[20] E. Okress, D. Wroughton, G. Comenetz, P. Brace, and J. Kelly. "Electromagnetic levitation of solid and molten metals." In: *Journal of Applied Physics* 23 (1952), pp. 545–552.

[21] W. R. Smythe. *Static and Dynamic Electricity*. McGraw-Hill Book Company, Ing., 1950.

[22] P. R. Rony. "The electromagnetic levitation of metals." In: *Trans. Vacuum Met. Conference*. Ed. by M. Cocca. Amer. Vacuum Society, 1965. Boston, MA.

[23] D. L. Cummings and D. A. Blackburn. "Oscillations of magnetically levitated aspherical droplets." In: *Journal of Fluid Mechanics* 224.1 (Mar. 1991), p. 395. DOI: 10.1017/s0022112091001817.

[24] L. Rayleigh. "On the Capillary Phenomena of Jets." In: *Proceedings of the Royal Society of London* 29.196-199 (Jan. 1879), pp. 71–97. DOI: 10.1098/rspl.1879.0015.

[25] T. Leitner. "Thermophysical properties of liquid aluminium determined by means of electromagnetic levitation." MA thesis. Institute of Experimental Physics, Graz University of Technology, 2016.

[26] A. Werkovits. "Surface tension measurements of liquid nickel and steel W360 using electromagnetic levitation." MA thesis. Institute of Experimental Physics, Graz University of Technology, 2019.

[27] O. Klemmer. "Surface tension of the liquid iron-nickel system determined by means of electromagnetic levitation." MA thesis. Institute of Experimental Physics, Graz University of Technology, 2017.

[28] G. Lohöfer, P. Neuhaus, and I. Egry. "TEMPUS - A Facility for Measuring Thermophysical Properties of Undercooled Liquid Metals." In: *High Temperatures, High Pressures* 23 (1991), pp. 333–342.

[29] G. Lohöfer and G. Pottlacher. "Inductive measurement of thermophysical properties of electromagnetically levitated metallic melts." In: *High Temperatures, High Pressures* 40.3-4 (3-4 2011), pp. 237–248.

[30] A. S. Tenney. "Radiation Ratio Thermometry." In: *Theory and Practice of Radiation Thermometry*. John Wiley & Sons, Inc., pp. 459–494. DOI: 10.1002/9780470172575.ch6.

[31] P. Neuhaus, I. Egry, and G. Lohöfer. "Aspects of high-temperature pyrometry for measurements in ultrahigh vacuum." In: *International Journal of Thermophysics* 13.1 (Jan. 1992), pp. 199–210. DOI: 10.1007/bf00503367.

[32] H. Lamb. "On the Oscillations of a Viscous Spheroid." In: *Proceedings of the London Mathematical Society* s1-13.1 (Nov. 1881), pp. 51–70. DOI: 10.1112/plms/s1-13.1.51.

[33] W.-K. Rhim, S. K. Chung, D. Barber, K. F. Man, G. Gutt, A. Rulison, and R. E. Spjut. "An electrostatic levitator for high-temperature containerless materials processing in 1-g." In: *Review of Scientific Instruments* 64.10 (Oct. 1993), pp. 2961–2970. DOI: 10.1063/1.1144475.

[34] H. Tamaru, C. Koyama, H. Saruwatari, Y. Nakamura, T. Ishikawa, and T. Takada. "Status of the Electrostatic Levitation Furnace (ELF) in the ISS-KIBO." In: *Microgravity Science and Technology* 30.5 (June 2018), pp. 643–651. DOI: 10.1007/s12217-018-9631-8.

[35] JAXA. *JAXA ELF*. URL: https://iss.jaxa.jp/en/kiboexp/pm/elf/ (visited on 02/25/2021).

[36] JAXA. 2020. URL: https://darts.isas.jaxa.jp/iss/kibo/files/reference/aos_los.pdf (visited on 11/08/2020).

[37] B. J. Simonds, J. Sowards, J. Hadler, E. Pfeif, B. Wilthan, J. Tanner, C. Harris, P. Williams, and J. Lehman. "Time-Resolved Absorptance and Melt Pool Dynamics during Intense Laser Irradiation of a Metal." In: *Physical Review Applied* 10.4 (Oct. 2018). DOI: 10.1103/physrevapplied.10.044061.

[38] E. Kaschnitz, H. Kaschnitz, T. Schleutker, A. Guelhan, and B. Bonvoisin. "Electrical resistivity measured by millisecond pulse-heating in comparison to thermal conductivity of the stainless steel AISI 316L at elevated temperature." In: *High Temperatures, High Pressures* 46 (2017).

[39] H. Fukuyama, H. Higashi, and H. Yamano. "Thermophysical Properties of Molten Stainless Steel Containing 5 mass % B_4C." In: *Nuclear Technology* 205.9 (Mar. 2019), pp. 1154–1163. DOI: 10.1080/00295450.2019.1578572.

[40] B. Wilthan, H. Reschab, R. Tanzer, W. Schützenhöfer, and G. Pottlacher. "Thermophysical Properties of a Chromium–Nickel–Molybdenum Steel in the Solid and Liquid Phases." In: *International Journal of Thermophysics* 29.1 (Nov. 2007), pp. 434–444. DOI: 10.1007/s10765-007-0300-1.

[41] P. Pichler, B. J. Simonds, J. W. Sowards, and G. Pottlacher. "Measurements of thermophysical properties of solid and liquid NIST SRM 316L stainless steel." In: *Journal of Materials Science* 55.9 (Dec. 2019), pp. 4081–4093. DOI: 10.1007/s10853-019-04261-6.

[42] *SRM 1155a., AISI 316 Stainless Steel*. (National Institute of Standards and Technology; U.S. Department of Commerce, Gaithersburg, MD, 2013).

[43] E. M. Barrall. "Precise determination of melting and boiling points by differential thermal analysis and differential scanning calorimetry." In: *Thermochimica Acta* 5.4 (Feb. 1973), pp. 377–389. DOI: 10.1016/0040-6031(73)80016-4.

[44] M. Schmid. *Vapor pressure Calculator IAP/TU Wien Surface Group 2013-2019*. (Visited on 10/09/2020).

[45] E. B. Ferreira, M. L. Lima, and E. D. Zanotto. "DSC Method for Determining the Liquidus Temperature of Glass-Forming Systems." In: *Journal of the American Ceramic Society* 93.11 (Aug. 2010), pp. 3757–3763. DOI: 10.1111/j.1551-2916.2010.03976.x.

[46] A. S. Pedersen, N. Pryds, S. Linderoth, P. H. Larsen, and J. Kjøller. In: *Journal of Thermal Analysis and Calorimetry* 64.3 (2001), pp. 887–894. DOI: 10.1023/a:1011506526074.

[47] E. Kaschnitz, H. Kaschnitz, T. Schleutker, A. Guelhan, and B. Bonvoisin. "Electrical resistivity measured by millisecond pulse-heating in comparison to thermal conductivity of the stainless steel AISI 316L at elevated temperature." In: 46 (2017).

[48] K. Mills. *Recommended values of thermophysical properties for selected commercial alloys*. Woodhead Publishing, 2002.

[49] S. Ozawa, K. Morohoshi, and T. Hibiya. "Influence of Oxygen Partial Pressure on Surface Tension of Molten Type 304 and 316 Stainless Steels Measured by Oscillating Droplet Method Using Electromagnetic Levitation." In: *ISIJ International* 54.9 (2014), pp. 2097–2103. DOI: 10.2355/isijinternational.54.2097.

[50] R. F. Brooks and P. N. Quested. "The surface tension of steels." In: *Journal of Materials Science* 40.9-10 (May 2005), pp. 2233–2238. DOI: 10.1007/s10853-005-1939-2.

[51] J. Manara. *Hi-Trace: Project Homepage*. URL: https://hi-trace.eu (visited on 12/09/2020).

[52] C. Cagran, B. Wilthan, and G. Pottlacher. "Normal spectral emissivity at a wavelength of 684.5 nm and thermophysical properties of liquid Molybdenum." In: *International Journal of Thermophysics* 25 (2004), pp. 1551–1566.

[53] P. D. Desai. "Thermodynamic Properties of Manganese and Molybdenum." In: *Journal of Physical and Chemical Reference Data* 16.1 (Jan. 1987), pp. 91–108. DOI: 10.1063/1.555794.

[54] A. Eber, P. Pichler, and G. Pottlacher. "Re-investigation of the normal spectral emissivity at 684.5 nm of solid and liquid molybdenum." In: *International Journal of Thermophysics* (2020). DOI: 10.1007/s10765-020-02769-7.

[55] voestalpine Böhler Edelstahl. *L625*. URL: https://www.bohler-edelstahl.com/en/products/l625/ (visited on 02/14/2021).

[56] K. D. Maglić, N. L. Perović, and A. M. Stanimirović. "Calorimetric and transport properties of Zircalloy 2, Zircalloy 4, and Inconel 625." In: *International Journal of Thermophysics* 15.4 (July 1994), pp. 741–755. DOI: 10.1007/bf01563797.

[57] E. Kaschnitz, L. Kaschnitz, and S. Heugenhauser. "Electrical Resistivity Measured by Millisecond Pulse Heating in Comparison with Thermal Conductivity of the Superalloy Inconel 625 at Elevated Temperature." In: *International Journal of Thermophysics* 40.3 (Feb. 2019). DOI: 10.1007/s10765-019-2490-8.

[58] T. Leitner. "Thermophysical property measurement of industrial metals and alloys using electromagnetic levitation." PhD thesis. Institute of Experimental Physics, Graz University of Technology, 2021.

[59] S. Heugenhauser and E. Kaschnitz. "Density and thermal expansion of the nickel-based superalloy INCONEL 625 in the solid and liquid states." In: *High Temperatures, High Pressures* 48 (4 2019), pp. 381–393.

[60] B. Wilthan. "Verhalten des Emissionsgrades und thermophysikalische Daten von Legierungen bis in die flüssige Phase mit einer Unsicherheitsanalyse aller Messgrößen." PhD thesis. Institute of Experimentalphysics, Graz University of Technology, 2005.

[61] T. Macher. "Modernisierung einer ohmschen Pulsheizapparaturzur Bestimmung thermophysikalischer Daten von Metallen in der flüssigen Phase -Datenerfassung, Datenauswertung und Unsicherheitsanalyse." MA thesis. Institute of Experimentalphysics, Graz University of Technology, 2014.

[62] M. Matus. "Koeffizienten und Ausgleichsrechnung: Die Messunsicherheit nach GUM. Teil 1: Ausgleichsgeraden (Coefficients and Adjustment Calculations: Measurement Uncertainty under GUM. Part 1: Best Fit Straight Lines)." In: *tm - Technisches Messen* 72.10/2005 (Jan. 2005). DOI: 10.1524/teme.2005.72.10_2005.584.